UNIVERSITAT POLITÈCNICA
DE CATALUNYA
BARCELONATECH

DEPARTAMENT DE TEORIA DEL SENYAL I COMUNICACIONS

"Acquisition and Processing Software for an Airborne Soil Moisture Mapper L-Band Radiometer"

Author:

Xavier Bosch i Lluis

Advisors:

Dr. Adriano José Camps Carmona

René Acevo Herrera

Barcelona, July 2010

“Acquisition and Processing Software for an Airborne Soil Moisture Mapper L-Band Radiometer”

*This work, conducted as part of the award "***Passive Advanced Unit (PAU): A Hybrid L-band Radiometer, GNSS-Reflectometer and IR-Radiometer for Passive Remote Sensing of the Ocean"** *made under the European Heads of Research Councils and European Science Foundation EURYI (European Young Investigator) Awards scheme in 2004, was supported by funds from the Participating Organizations of EURYI and the EC Sixth Framework Program.*

Outline

1 Introduction

1.1 General Background

The improvement in weather forecast and climate motorization, to prevent for example natural disasters, requires global scale knowledge of the soil moisture (SM) and the surface salinity (SSS), which are non-existent at present due to the difficulty to carry out in-situ measurements. These parameters influence the heat exchange among land, sea and air. On one hand, thanks to the SM, the amount of water on Earth and the exchange of energy between the land's surface and the atmosphere can be known. On the other hand, the knowledge of the distribution of the SSS will inform about sea currents and differences between evaporation and precipitation. The quantification of these parameters will contribute to improve the weather forecasts, hydrological studies, vegetation motorization, and risk of forest fires.

As part of the program "*The living planet programme: Earth Explorer Opportunity Missions"*, the European Space Agency (ESA) selected in 1999 the Soil Moisture and Ocean Salinity (SMOS) mission, designed to observe soil moisture over land and salinity over the oceans. It was launched in 2009 and has put in orbit the first microwave imaging radiometer using aperture synthesis. Over the sea, sea surface salinity will be remotely measured by means of L-band (1400-1427 MHz) microwave radiometry. As the brightness temperature also depends on the sea surface temperature and on the sea state, post-processing corrections are needed to get the surface salinity. Over land, soil moisture is retrieved from the changes in the L-band brightness temperature, although post processing correction for surface roughness and vegetation are also required.

1.2 Motivation of this project

Radiometry is a mature technique that has demonstrated in the past years to be readily suitable for remote sensing applications. One of the most promising applications is soil moisture sensing. Within this background, the group of the Remote Sensing Laboratory (RSLab) decided some years ago to design an airborne radiometer capable of generating soil moisture images to investigate its possibilities.

In order to minimize the cost, the platform was designed especially for the requirements of the project, it is remotely controlled and can flow over any aerodrome area. Due to the airborne platform dimensions, the system provides enough autonomy to plan field campaigns to test the onboard equipment or to improve the post-processing algorithms whenever it is necessary, without too many external constraints. The resulting airborne data acquired can be processed and further analyzed to deploy the instrument's capabilities. The aim of this project is to produce an application to geo-reference sea salinity and/or soil moisture maps over Google Earth. In order to achieve this goal, the data processing from the different sensors has been performed in an automatic manner. Furthermore, specific software will be developed in order to create automatically soil moisture maps from the radiometric data. A set of tools has been implemented so as to analyze and understand the data obtained. Graphical visualizations such as histograms, graphs and display of antenna footprints and trajectory, are provided for a further data interpretation.

This work takes advantage of several previous works, in the following lines a chronological order and the most relevant milestones are provided in order to better understand the underlying work:

- The master thesis entitled: "*Disseny i implementació d'un radiòmetre/reflectòmetre lleuger embarcat en un avió*" by Francesc Bou [1] in May 2006 and it was the first work on this topic in the RSLab-UPC. In this work the system was envisaged, the hexagonal and seven patches antenna (Fig. 1-1a) were

designed and built. The aim of this project was to develop PAU-One Receiver Airborne (PAU-ORA) [1] at L1 GPS band, which is a hybrid of a reflectometer and a radiometer. In this system, the collected data was sent to a ground station in real time, using a radio-link in the ICM bands (465 and 868 MHz). Despite the huge amount of energy deployed to fulfill the project requirements, the system never flown and finished as a ground concept demonstrator (Fig 1-1b).

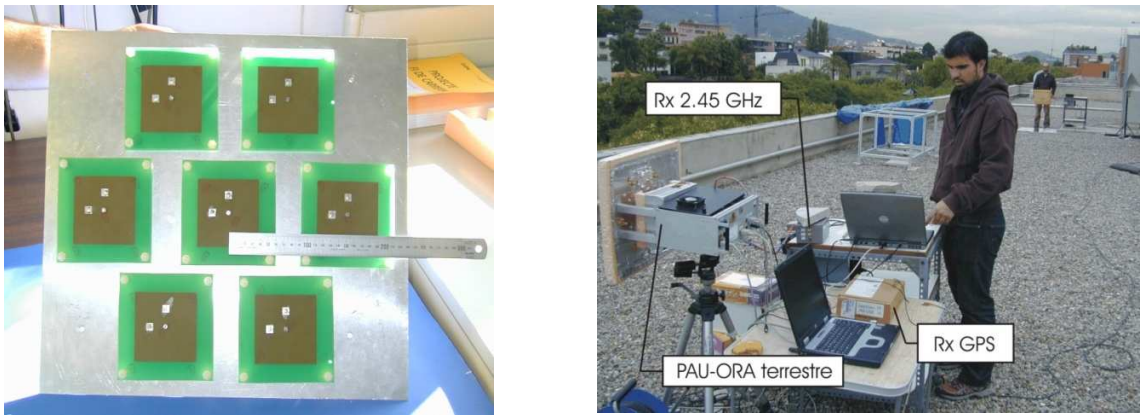

(a) (b)

Fig. 1-1 : Pictures from F. Bou's M.Sc. Thesis: (a) 7 element hexagonal patch antenna array and (b) Ground demonstrator of the PAU-ORA system.

- Master thesis entitled: *"Diseño e implementación de un sistema híbrido GPS-inerciales para determiner la trayectoria de un avión de RC y de unos módulos de comunicación en bandas ICM con estación base"* by Carlos Ibañez [2], May 2006. This work was the companion of the previous one, were the transmission system was set up, the avionic subsystems were designed and the IMUs (magnetometers, accelerometers and gyroscopes) measurements were provided to record the attitude of the aircraft (Fig. 1-2ab). Moreover, a GPS on board was also used for further geolocating of the acquired radiometric data.

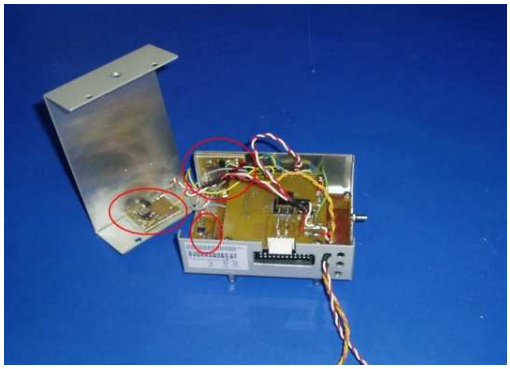

(a)

(b)

Fig. 1-2 : Pictures from C. Ibáñez's M.Sc. Thesis: (a) the packaged IMUs system and (b) IMUs, control and transmission system boarded on the RC aircraft.

- Master thesis entitled: "*Emisividad del terreno en banda L: Estudio y medida del efecto de la topografia*" by Pablo Benedicto [3], December 2006. Two important milestones were achieved during this project: the first one was to change the boarded instrument from PAU-ORA to Airborne RadIomEter at L band (ARIEL), having a Dicke radiometric topology and working at the remote sensing reserved L-band (1400-1427 MHz). The second milestone was that some data were collected during a field campaign and it was approximately plotted over a map (Fig 1-3 ab). Unfortunately, the system had some aerodynamic problems that required an entire reconstruction of the airborne platform.

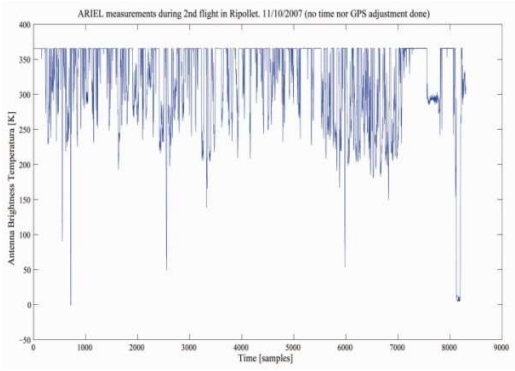

(a)

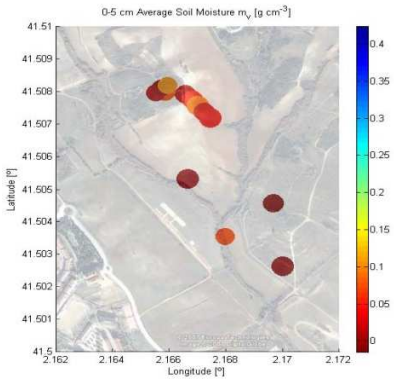

(b)

Fig. 1-3: Pictures from P. Benedicto's M.Sc. Thesis: (a) Collected brightness temperature and (b) Retrieved Soil moisture plotted approximately on a map.

- Master thesis entitled: "*Georeferencing in Google Earth radiometric data from UAV: Simulation and experimental data processing*" by Mathilde Glénat [4], July 2008. The IMU system was replaced by the digital compass F350-Compass-RD^{TM} from Silicon Laboratories, the main drawback was that only one measurement per second was provided. It was the first time that pixels were created accordingly to the attitude and the height of the plane and the beam pattern of the antenna, some great results were obtained (Fig. 1-4 ab). Furthermore, the radio control platform shown its possibilities as viable and high performance remote sensing system. This work has won the first award from IEEE GRSS Spanish section for the best master Thesis on remote sensing of 2008.

(a)

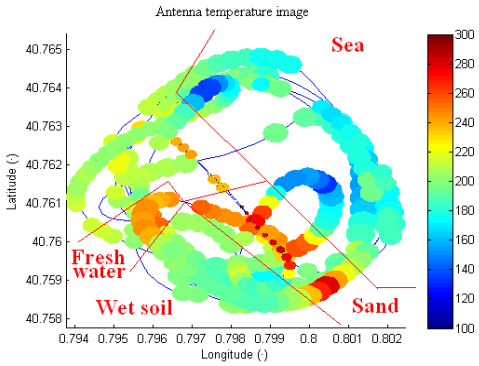

(b)

Fig. 1-4: Pictures from M. Glénat's M.Sc. Thesis: (a) ARIEL during a T_{Cold} calibration and (b) brightness temperature analysis, results obtained in the Ebre river Mouth campaign.

- Master thesis entitled: "*Soil Moisture Retrieval Using an Airbone L-Band Radiometer*" by Arnaud Duperrier [5], July 2008. In this work no hardware improvements were done, the work focused on the software design. A user friendly processor, called ARIEL Processor-Soil Moisture Retrieval (AP-SMR), was developed with lots of functionalities within the most important are: the possibility of filtering the data by height, by angle, by temperature range or by soil moisture range, and the possibility to plot the data in histograms to understand the nature of the collected data. The soil moisture retrieval algorithm was set up for the first

time and interpolation techniques were used to fill the remaining gaps due to a non uniform flight increasing the coverage of the final product parameters. Figure 1-5 ab show some results.

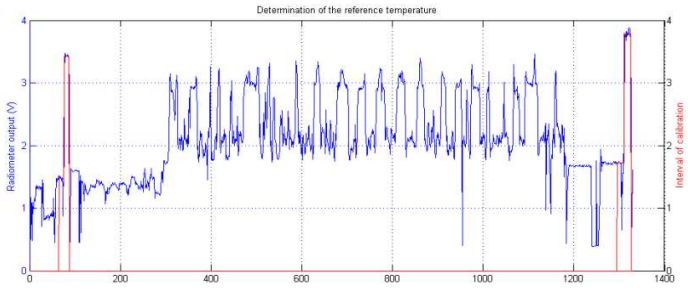

(a)

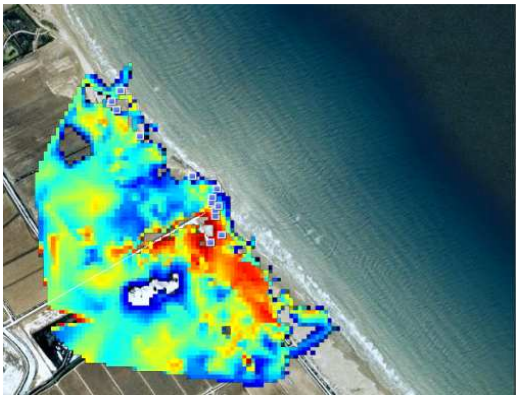

(b)

Fig. 1-5: Pictures from A. Duperrier's M.Sc. Thesis: (a) Voltage output and (c) AP-SMR outputs, results obtained in the Ebre river Mouth campaign.

- Ph.D thesis proposal (Diploma Estudis Avançats, DEA) entitled: "UAV/Airborne active and passive remote sensing instruments for Earth monitoring" by Rene Acevo [6], January 2009. In this work some important improvements were done regarding the post processing data. The most important achieved milestones were: the miniaturization of the radiometer (Fig 1-6 a) and the interpolation technique using the antenna diagram to interpolate and merge the final data (Fig. 1-6 b). Some important tests were performed during this work, for example during the GRAJO [7] experiment, to test the suitability of the platform for retrieving soil moisture information of an agricultural field and to assess scientific hypotheses and experiments.

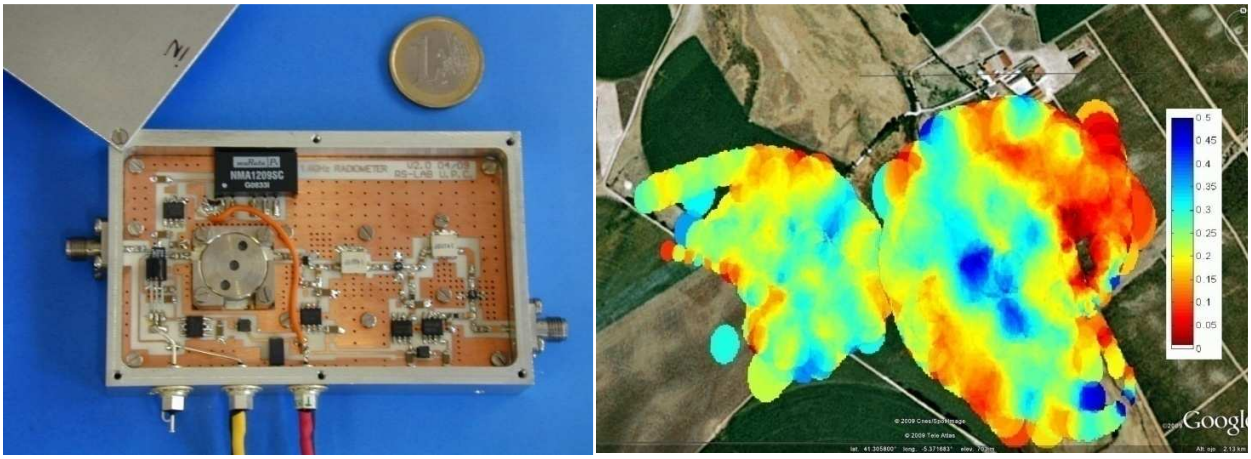

(a) (b)

Fig. 1-6 : Pictures from R. Acevo's Ph.D. Thesis proposal: (a) new ARIEL RF front end 10 x 6 x 2 cm and (b) Soil moisture map (0-50%) in GRAJO experiment in Salamanca (Spain) mixing two different flights.

The aim of the present work is to culminate the knowledge acquired in the previous system's versions into a non-expert user instrument. For that purpose the principal novelties are:

1. an onboard embedded computer which collects the relevant data,
2. a commercial and high performance IMS system,
3. a two beam radiometer for soil moisture and vegetation content retrieval. The first beam is pointing to nadir with horizontal polarization and the other is fore-looking with an incidence angle of 22^{o} with vertical polarization, and
4. a new user friendly software which includes: the controller, running on the onboard computer to drive the radiometer and the processor for non-expert users. Both programs have been developed focusing on a non-expert user who with the main objective of collecting data, needs the platform as a tool instead of a scientific platform.

1.3 Specification of the airborne platform

The ARIEL carrying aircraft has been designed to be a remote control aircraft capable of carrying 5 kg payload and with 30 min autonomy to scan an area over land and/or sea. It has a high wing surface in order to provide a stable flight. In addition to the aircraft instrumentation, an hexagonal 7-patch array antenna is mounted under the aircraft (Fig. 1-7) and an on-board nadir-looking video camera is also embedded to help the interpretation of the data acquired by the payload. The inner part of the fuselage allows loading the necessary equipments as GPS (Global Positioning System) and attitude sensors. Data from these instruments are acquired and stored for later processing.

Fig. 1-7: ARIEL radiometer during a flight test in Ripollet, Barcelona

1.4 Structure of this report

This project is divided in six chapters. First, chapter two reviews the basics of radiometry, emission theory and types of radiometer. Chapter three covers the onboard system, describing the both sensors (X-sens and microwave radiometer), to be able to explain the aircraft software driver that collects the geolocated radiometric data with the attitude information. Chapter four

describes the main functions and algorithms implemented in the Processor. The main steps of the data processing are explained: synchronization, calibration and soil moisture retrieval. Furthermore, this chapter describes the graphical interface of the processor, how to use it, and how to get the geo-referenced images over Google Earth. Chapter five presents results obtained in two field experiment, analyzing the soil moisture estimations obtained. Finally, chapter six presents some conclusions and future research lines.

2 Microwave radiometry

This chapter provides an introduction to microwave radiometry, which is the field of science devoted to the measurement of the thermal electromagnetic energy radiated by the bodies. Since the appearance of remote sensing satellites, radiometry has played an important role in remote sensing. A radiometer is an instrument that measures the brightness temperature, that is, the power emitted by a body by unit solid angle, and by unit surface, with high resolution and accuracy.

In this chapter microwave radiometry concepts are introduced and then the simplest two types of radiometers are described: the total power radiometer (TPR) and the Dicke radiometer (DR).

2.1 Power collected by an antenna

The power emitted by a body in a solid angle by unit surface is called the brightness, units [W sr^{-1} m^{-2}]. If the emitting surface radiates with a pattern $F_t(\theta,\phi)$, the brightness $B(\theta,\phi)$ is given by:

$$B(\theta,\phi) = \frac{F_t(\theta,\phi)}{A_t} \tag{2.1}$$

where A_t is the total area which is radiating.

The power collected by an antenna surrounded by a distribution of incident power $B(\theta,\phi)$ can be computed as:

$$P = F_t \frac{A_r}{R^2} = B A_t \frac{A_r}{R^2} \tag{2.2}$$

with A_r the effective area of the antenna and R the distance to the radiating surface. Taking into account that the solid angle Ω_t subtended by the transmitting antenna is defined by:

$$\Omega_t = \frac{A_t}{R^2} \tag{2.3}$$

Then, the power collected by the antenna can be computed as:

$$P = B \cdot A_r \cdot \Omega_t . \tag{2.4}$$

Replacing the solid angle by a differential solid angle $(d\Omega)$, the corresponding power received by the antenna from an extended source of incidence brightness $B(\theta,\phi)$ can be expressed as:

$$dP = A_r B(\theta,\phi)|F_n(\theta,\phi)|^2 d\Omega \tag{2.5}$$

where $|F_n(\theta,\phi)|^2$ is the normalized antenna radiation pattern. Moreover, if the brightness is not constant with frequency, a new magnitude must be defined: the spectral brightness density $B_f(\theta,\phi)$, units [W sr^{-1} m^{-2} Hz^{-1}]. The total power collected by the antenna is then obtained by integrating Eq. (2.5) over the system's bandwidth and over the space:

$$P = \frac{1}{2} \cdot A_r \int_{f}^{f+B} \iint_{4\pi} B_f(\theta,\phi) \cdot |F_n(\theta,\phi)|^2 \cdot d\Omega \cdot df \tag{2.6}$$

where B is the bandwidth of the receiving system. Since the antenna collects only half of the randomly polarized thermal emitted power, it is multiplied by a factor $\frac{1}{2}$.

2.2 Thermal radiation

2.2.1 Quantum theory of radiation

All bodies at a finite absolute temperature radiate electromagnetic energy. According to Bohr's equation, the frequency *f* of an emitted radiation is given by:

$$f = \frac{\varepsilon_1 - \varepsilon_2}{h}, \tag{2.7}$$

where ε_1 and ε_2 are different energy levels in J, and *h* is the Planck's constant (*h* = $6.63 \cdot 10^{-34}$ J). The emission of radiation is caused by electrons changing its energy moment following Eqn. 2-7. The emission probability is a function of the density of the particles and the kinetic energy of their random motion. The increase of the intensity of the energy radiated by a body is proportional to the increase of its absolute temperature.

2.2.2 Planck's radiation's law

In general, part of the electromagnetic energy incident on a surface is absorbed, and part is reflected. The spectral brightness (brightness per unit bandwidth) is given by the Planck's law Eq. (2.8).

$$B_f = \frac{2 \cdot h \cdot f^3}{c^2} \cdot \frac{1}{e^{hf/kT_o} - 1}, \tag{2.8}$$

where *f* is the frequency in Hertz (Hz), *k* is the Boltzmann's constant (k = $1.38 \cdot 10^{-23}$ J K^{-1}), T_o is the absolute physical temperature in Kelvin, and *c* is the speed of light (c ≈ $3 \cdot 10^8$ m s^{-1}).

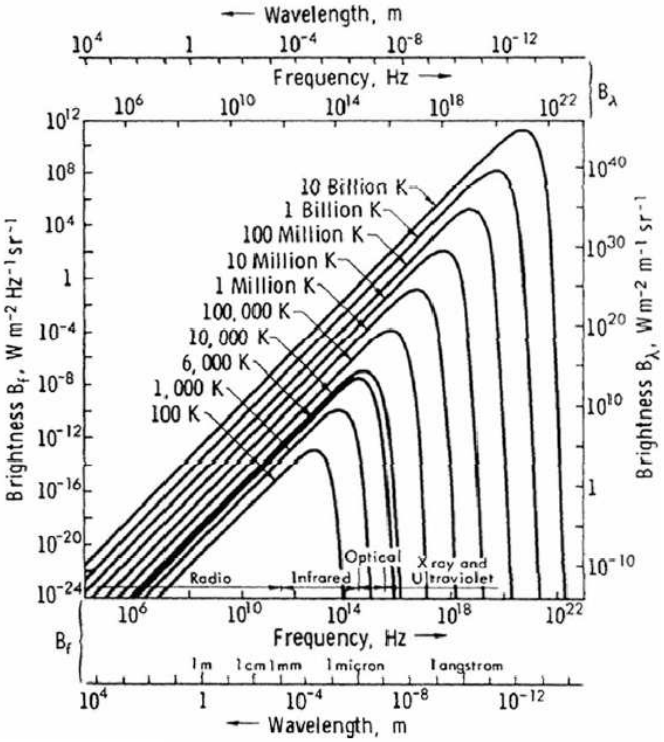

Fig. 2-1 : Planck's radiation law [8]

Applying a Taylor's approximation to the exponential function in Eq. (2.8), the exponent hf/kT_o in the denominator of Planck's law is far smaller than 1 at microwave frequencies, and therefore, the following approximation can be used to simplify Eq. (2.8).

$$e^x - 1 = 1 + x + \frac{x^2}{2} + \ldots - 1 \approx x \;\; for \;\; x << 1. \tag{2.9}$$

Hence, at low microwave frequencies the Rayleigh-Jeans law can be used as good approximation of the Planck's law (2.8) and can be written as:

$$B_f \approx \frac{2 \cdot f^2 \cdot k \cdot T_{phys}}{c^2} = \frac{2 \cdot k \cdot T_{phys}}{\lambda^2}. \tag{2.10}$$

In this case, if λ and T_o appearing Eq. (2.10) satisfy that:

$$\lambda \cdot T_o > 0.77\ m\,K,\ \ \frac{f}{T_o} < 3.9 \cdot 10^8\ Hz \cdot K^{-1}, \tag{2.11}$$

The error by the Rayleigh-Jeans' approximation, which covers a large part of the microwave spectrum, is smaller than $1.2 \cdot 10^{-4}$, if the physical temperature is 300 K and the frequency is 1.4 GHz. Equation (2.10) will be used from now on. Note that there is a linear relationship between the spectral brightness density and the physical temperature.

2.2.3 Power-temperature correspondence

The power received by an antenna with normalized radiation pattern $|F_n(\theta,\phi)|^2$, placed inside of a black-body chamber at a constant physical temperature T_o is given by:

$$P_{bb} = \frac{1}{2} \cdot A_r \cdot \int_f^{f+B} \iint_{4\pi} \frac{2 \cdot k \cdot T_o}{\lambda^2} |F_n\ (\theta,\phi)\ |^2\, d\Omega \cdot df, \tag{2.12}$$

where the subscript *bb* stands for black-body.

The detected power is limited by the receiver's bandwidth *B*. If this bandwidth is small enough to assume that the spectral brightness density does not change over the frequency range, Eq. (2.12) is reduced to:

$$P_{bb} = k \cdot T_o \cdot B \cdot \frac{A_r}{\lambda^2} \cdot \iint_{4\pi} |\ F_n\,(\theta,\phi)\ |^2\, d\Omega = k \cdot T_o B, \tag{2.13}$$

where the antenna solid angle has been expressed as a function of its effective area:

$$\Omega_p = \iint_{4\pi} |F_n\ (\theta,\phi)\ |^2\, d\Omega = \frac{\lambda^2}{A_r}. \tag{2.14}$$

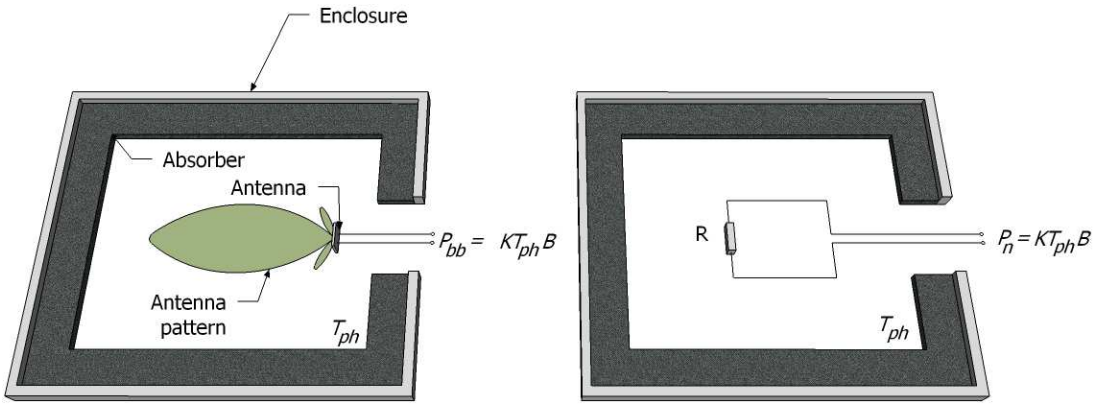

Fig. 2-2 : The power delivered by: (a) an antenna placed inside of a black-body enclosure of temperature T_{ph} is equal to the power delivered by and (b) a resistor maintained at the same physical T_{ph} (assuming each one is connected to a matched receiver of bandwidth *B*)

Equation 2-13 shows a linear relationship between the physical temperature of a body and the power collected by an antenna. In 1928, Nyquist found the same expression (Eq. (2.15)) for the available power at the terminals of a resistance at a physical temperature T_o. This means that, for an ideal receiver of bandwidth B, the antenna delivers to the load the same power as a resistance at a temperature T_A, which is called the antenna temperature:

$$P = k \cdot T_o \cdot \mathrm{B}. \tag{2.15}$$

2.2.4 Gray-body radiation

2.2.4.1 Brightness temperature and emissivity

A black-body is an idealized body and it is a perfect emitter. These bodies absorb all the incident energy, and when the thermodynamic equilibrium is reached at a physical temperature T_o, they radiate all the energy omni-directionally. However, real materials (usually called gray-bodies) emit less energy than a black-body, since they do not absorb all the incident energy on them. Since the universe is composed of gray-bodies two new concepts are introduced, the brightness temperature $(T_B(\theta,\phi))$ and the emissivity $(e(\theta,\phi))$. Equation 2.16 shows the relationship between these two concepts:

$$e(\theta,\phi)=\frac{B(\theta,\phi)}{B_{bb}}=\frac{T_B(\theta,\phi)}{T_o}, \tag{2.16}$$

where B_{bb} is the brightness of the black-body at a temperature T_o.

The brightness temperature emitted by a black-body coincides with its physical temperature hence its emissivity is 1. Consequently the brightness temperature emitted by real bodies is less than the physical temperature, and then their range of emissivity values is between 0 and 1. In conclusion, the emissivity of a perfect reflecting material is equal to zero and the emissivity of a perfect absorber is one.

2.2.4.2 The apparent temperature

The apparent temperature (T_{AP}) is an equivalent temperature related to the total brightness incident over the antenna, $B_i(\theta,\phi)$:

$$B_i(\theta,\phi)=\frac{2\cdot k}{\lambda^2}\cdot T_{AP}(\theta,\phi)\cdot \mathrm{B} \tag{2.17}$$

In remote sensing applications, the T_B of the surface is measured by an antenna far away (Fig. 2-3). In this case, the apparent temperature T_{AP} is the key parameter that depends on:

- the brightness temperature of the surface under observation (T_B),
- the atmospheric upward radiation (T_{UP}),
- the atmospheric downward radiation scattered reflected by the surface (T_{SC}), and
- the atmospheric attenuation (L_a),

and can be written as:

$$T_{AP} = T_{UP} + \frac{1}{L_a} \cdot \left(T_B + T_{SC}\right). \tag{2.18}$$

By observing Eq. (2.18), when the atmospheric losses are high, the apparent temperature is almost equal to the atmospheric temperature. This happens at high frequencies or at the absorption windows of some gases. If the brightness temperature of the Earth surface is being measured, it will be necessary to work at frequencies that give low atmospheric attenuation. In the frequency range from 1 GHz to 10 GHz losses for a cloud-free atmosphere are very small and can be mostly neglected. Consequently the apparent brightness temperature (T_{AP}) can be approximated by the brightness temperature (T_B).

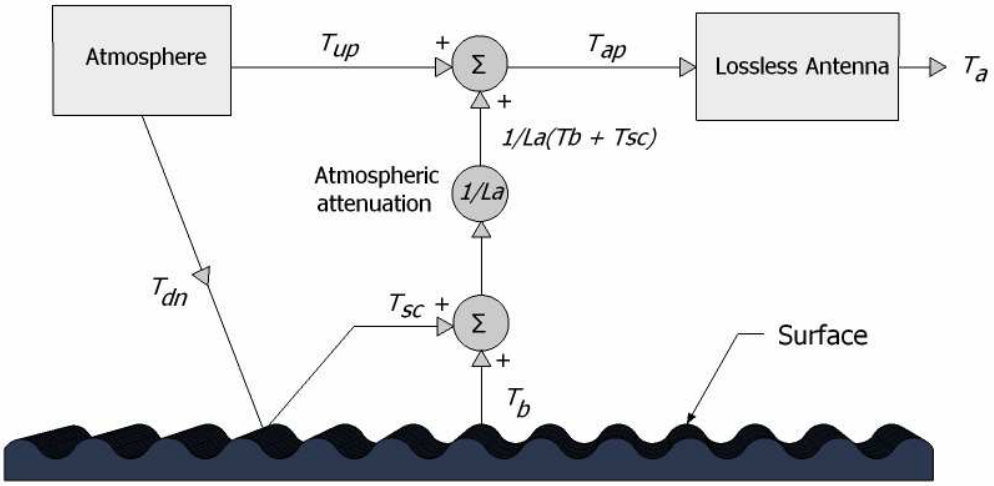

Fig. 2-3 : Relationship between the antenna temperature T_a, the apparent temperature T_{ap} and the brightness temperature T_b .

According to Fig. 2-3**,** and taking into account the normalized antenna pattern ($\boldsymbol{F_n(\theta,\phi)}$) and normalized by the pattern solid angle Ω_p, the antenna temperature is given by:

$$P = \frac{1}{\Omega_p} kB \iint_{4\pi} T_{AP}(\theta,\phi) \mid F_n(\theta,\phi) \mid^2 d\Omega = kT_A B, \tag{2.19}$$

$$T_A = \frac{1}{\Omega_p} \iint_{4\pi} T_{AP}(\theta,\phi) \mid F_n(\theta,\phi) \mid^2 d\Omega. \tag{2.20}$$

2.3 Types of microwave radiometers

2.3.1 Introduction

As it has been seen in the previous part 2.2.4.2, if an antenna is pointing to a body, the power that is collected at its output (expressed in term of antenna temperature T_A) is related to the brightness temperature T_B of this body. A microwave radiometer is an instrument that measures the antenna temperature (T_A) with high resolution and accuracy. In practice, a radiometer measures the power delivered by the antenna to the receiver. In fact, a microwave radiometer is a well calibrated and high sensitive microwave receiver.

The performance of a radiometer is characterized by two important factors: sensitivity and accuracy. The first one determines the smallest change in T_A that can be detected by the radiometer output. The second one indicates the correspondence of the measurement of the true value.

In order to illustrate these two aspects, the following example is analyzed; a radiometer is connected to an antenna which is exposed to a temperature T_A = 200 K, and the resolution requirement of the measure is of 1 K. The noise temperature introduced by the radiometer, like any receiver, has to be taken in account; a typical value will be T_R = 800 K. Then the aim of the radiometer is to perform a measurement which matches with a variation of 1 K over 1000 K (200 K + 800 K). In order to achieve this resolution, a radiometer uses an integration technique.

Therefore, if the radiometer's gain G and the noise temperature T_R are added in (2.19), the resulting output power is:

$$P = kBG(T_A + T_R). \tag{2.21}$$

As it is shown, the stability of the power measurement depends on the stability of the factors in Eqn. 2.21: B, G and T_R. As B is a parameter of the filter (passive device), it is assumed to be constant. Back to the previous example, if the required resolution is 1 K, it means that G and T_R have to be stable in an interval of ≤0.1 %, which corresponds to about 0.004 dB. Therefore the following problem appears that it will be difficult to get these requirements from an amplifier.

After having seen the two mains problems linked to the design of a radiometer, the main radiometer types and their behavior are presented in term of resolution and accuracy. A radiometer block diagram consists basically of an antenna, a super-heterodyne receiver which translates the radio frequency signal to an intermediate frequency, a detector and a low-pass filter.

This chapter focuses on the description of the radiometer operation as well as the introduction to different types of radiometers. Although more radiometer topologies exist such as the Noise Injection Radiometer (NIR) or the pseudo-correlation radiometer, the Total Power Radiometer (TPR) and Dicke Radiometer (DR) are presented here because its topology is the simplest and one of the most widely used and both are the two possible configurations of the ARIEL's radiometer topology.

2.3.2 Total Power Radiometer

The TPR is the more common radiometer used. It is easy to understand and can illustrate the most important notion of the performance of such instrument. Figure 2-4 is used to explain it with more details.

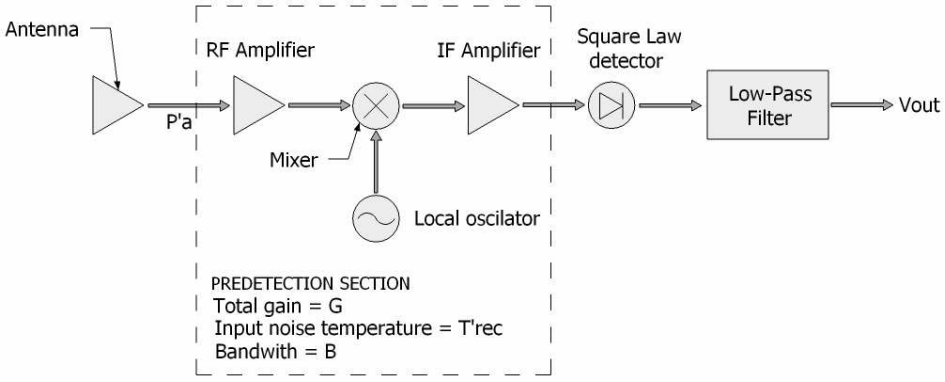

Fig. 2-4 : Total power radiometer block diagram [2.1]

In Fig. 2-4 the radiometer gain G is symbolized by an amplifier and its bandwidth B with a low-pass filter. To measure the noisy input signal, a square low detector is used. Its output is directly proportional related to the input signal and so to the temperature T_A. An integrator is used to reduce the fluctuations in the detected signal and therefore to increase the stability of the measurement. Moreover, as bigger the integration time, more stable will be the radiometer's output. The output voltage of the TPR is the following:

$$V_{out} = k\mathrm{BG}(T_A + T_R) = c(T_A + T_R), \tag{2.22}$$

where the parameters assumed to be constant are grouped in the factor *c*. In Eqn. 1.22 appears that V_{OUT} is depending on T_R and G. As said in the introduction of this chapter, with this dependence, the TPR will not be able to provide enough accuracy for most applications, mostly if the calibration is not performed very frequently. However, regarding the resoluiton of the TPR, it is calculated to be [9]:

$$\sigma_T = \frac{(T_A + T_R)}{\sqrt{\mathrm{B}\tau}}, \tag{2.23}$$

this will be the best resolution available for this type of radiometer. To conclude, with a TPR, the best theoretical resolution can be performed. However due to the gain fluctuations problems, a calibration process is required frequently.

2.3.3 Dicke radiometer

With the aim to correct the stability problems associated to gain fluctuations existing in the TPR, Dicke published in 1946 a radiometer design which is named after him.

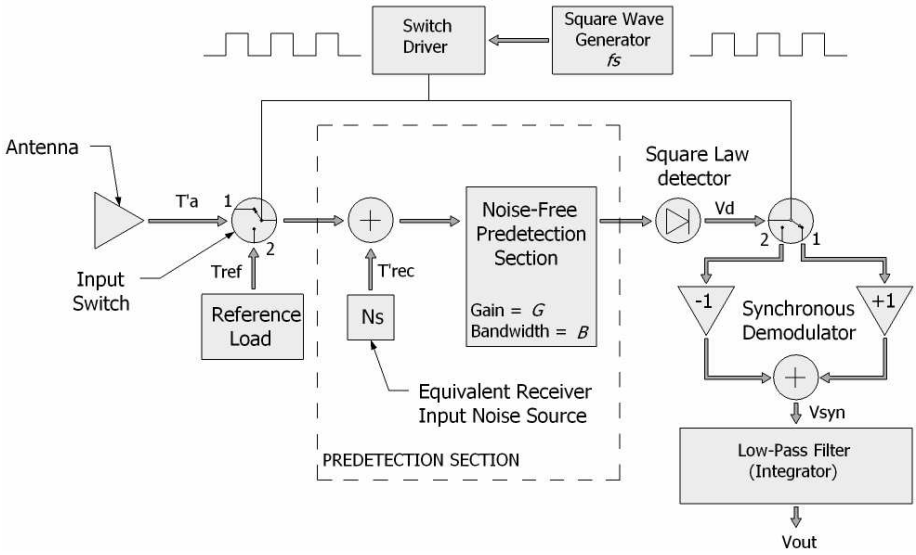

Fig. 2-5 : Dicke radiometer sketch

The Dicke radiometer (DR), instead of measuring directly the antenna temperature, performs the measurement of the difference between T_A and a reference temperature T_{REF} known. With this method, the noise temperature instability T_R is filtered out and the impact of the gain is largely reduced.

As it is shown in Fig 2-5, a DR is a modified TPR with an input switch that changes of position at a given frequency (f_S) between the antenna and the reference temperature T_{REF} and a synchronous demodulator (±1 multiplier). Therefore, two different outputs in distinct time slots are obtained. During one half period, the detector output gives:

$$V_A = c(T_A + T_R)\mathrm{G}, \tag{2.24}$$

and during the other half period:

$$V_{REF} = c(T_{REF} + T_R)\mathrm{G}. \tag{2.25}$$

If the switching frequency f_S is sufficiently fast to consider the parameter T_A, T_R and G constants during an entire period, and also that the period is smaller than the integration time ($f_s >> \tau^{-1}$), then the radiometer output can be expressed as:

$$V_{OUT} = V_A - V_{REF} = c(T_A - T_{REF}). \tag{2.26}$$

It can be observed in the Eq. 2.26 that the output of the radiometer does not depend now on the noise temperature T_R, and that the impact of the gain fluctuations G is proportional to the difference of temperatures (T_A - T_{REF}). Therefore if the temperature T_{REF} is chosen close to the antenna temperature T_A, the impact of G fluctuations is small. Then if (T_A - T_{REF})<< (T_A + T_R) is fulfilled, the DR increases the accuracy respect to the TPR. Although the stability of the system is improved, by measuring the antenna temperature just half of the time, there is a loss of resolution as compared to a TPR. The expression of the resolution of the DR can be calculated easily from the TPR equation (Eqn. 2.23). Indeed, on each half period, the radiometer can be assimilated to a TPR pointing to the antenna or to the reference load, using an integration time of $\tau / 2$. Therefore for the first half period, the resolution obtained is the following:

$$\sigma_{T_A} = \frac{(T_A + T_R)}{\sqrt{\mathrm{B}\frac{\tau}{2}}}, \tag{2.27}$$

and during the other half period:

$$\sigma_{T_{REF}} = \frac{(T_{REF} + T_R)}{\sqrt{\mathrm{B}\frac{\tau}{2}}} \tag{2.28}$$

Then the DR resolution is obtained by:

$$\sigma_T = \sqrt{\left(\sigma_{T_A}\right)^2 + \left(\sigma_{T_{REF}}\right)^2}. \tag{2.29}$$

As T_{REF} is assumed to be close from the typical value of T_A, from Eq. 2.27 and 2.29 is obtained:

$$\sigma_T = 2\frac{(T_A + T_R)}{\sqrt{\mathrm{B}\,\tau}}, \tag{2.30}$$

this means that, the Dicke radiometer, despite of being more stable, its radiometric resolution is a factor of two worse than the TPR.

2.3.4 Conclusions

A Dicke topology radiometer has been chosen for its improved stability as compared to a total power one, so it can be calibrated less frequently, for example at the beginning and/or the end of the flight. A balanced Dicke radiometer topology using noise injection, Noise Injection Radiometer (NIR), was first considered, but the limited improvement in stability did not compensate the extra weight and power consumption. The radiometric resolution that can be achieved with a balanced Dicke radiometer (NIR) is given by Eq. 2.30.

Taking into account that the RF bandwidth is 27 MHz (1400-1427 MHz) and that the maximum flight speed and minimum height determine a minimum integration time of 100 ms for the worst case, a radiometric sensitivity of ΔT= 0.71 K is derived, which is acceptable for soil moisture applications.

2.4 Microwave radiometry applications

There are many microwave radiometry applications. Mainly, they can be included in two groups: atmospheric applications and Earth surface applications. The main applications and their suitable frequencies are listed below (Table 1-1).

Table 1-1. Relationship between the radiometry application and its suitable frequency

Application	Frequency (GHz)
Clouds water content	21, 37, 90
Ice Classification	10, 18, 37
Sea Oil spills tracking	6.6, 37
Rain over soil	18, 37, 55, 90, 180
Rain over the ocean	10, 18, 21, 37
Sea Ice concentration	18, 37, 90
Sea Surface Salinity	**1.4**, 6.6
Sea Surface Temperature	6.6, 10, 18, 21, 37
Sea Surface Wind Speed	10, 18
Snow Coating	6.6, 10, 18, 37, 90
Soil Moisture	**1.4**, 6.6
Atmospheric Temperature Profiles	21, 37, 55, 90, 180
Atmospheric Water Vapour	21, 37, 90, 180

As shown, the frequency at L band (1.4 GHz) is the most suitable for applications related with the sea surface salinity or the soil moisture.

In this chapter the fundamentals of radiometry theory have been presented. The brightness temperature and the apparent temperature concepts have been defined, as well as the black and gray body relationships through the emissivity. Moreover, the band frequency used for the airborne radiometer has also been explained and justified.

3 Onboard Instrument Controller

This chapter is devoted to the analysis of the onboard instruments and the software designed for controlling the synchronous acquisition of both instrument. Figure 3-1 shows the whole ARIEL system sketch, the red-dotted rectangle shows where this chapter is focused. The left part of the figure is the onboard system, it consist of two sensors and designed software which runs in an embedded computer. The output of this part is the raw file which contains the synchronously acquired data from both instruments, MTi-G, which provides GPS time, position, velocity and attitude of the platform, and Radiometer, which provides antenna brightness temperature, reference temperature and physical temperature. Furthermore, the raw data file is the link between the processor (the right part).

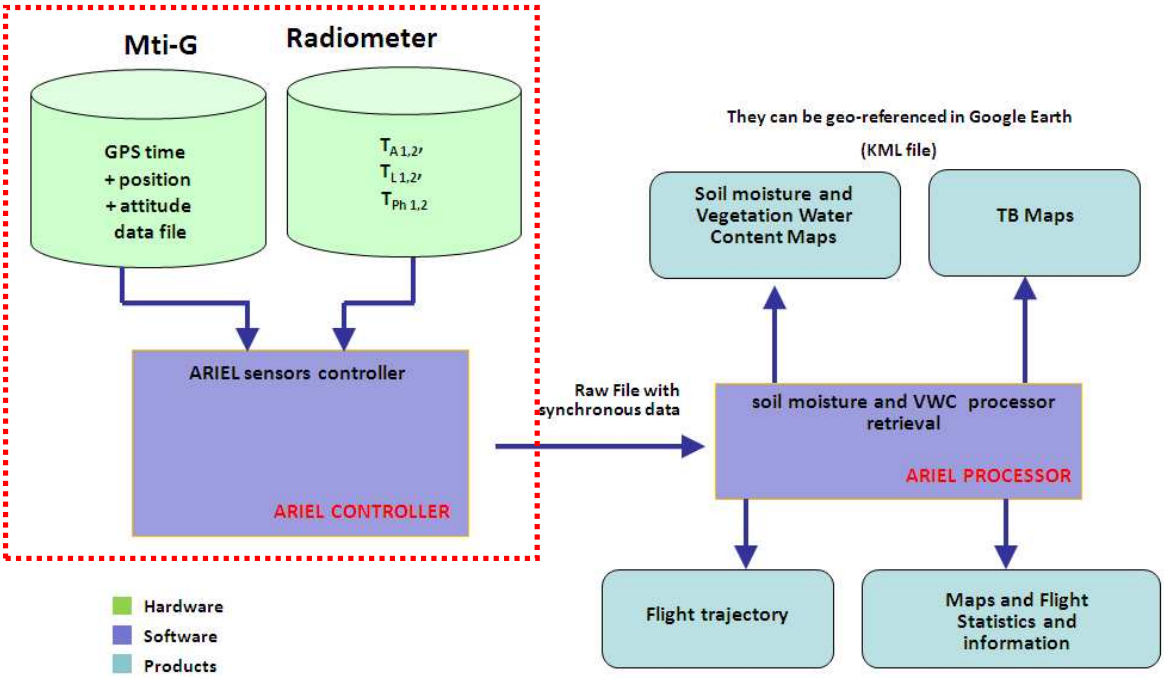

Fig. 3-1 : ARIEL system sketch.

3.1 Introduction

The radio controlled aircraft which carries the radiometer has been designed to fulfill the requirements of the project with to scan an area over land and/or sea. The antenna was designed to not interfere with the aircraft aerodynamics, but preserving a good electromagnetic performance. A GPS receiver (to record position and speed) and attitude sensors are deployed in the aircraft in order to geo-reference the aircraft and so the radiometric data on a map, for that purpose an embedded onboard computer acquires synchronously position and attitude data, and radiometric data. Until now, several flight tests have been carried out in order to test and then improve the prototype and some data have already been acquired [3.1].

Fig. 3-2. Aircraft with the radiometer embedded

The radiometer and the antenna are set up in the aircraft, the antenna is attached below the fuselage as it is noticed on Fig. 3-2.The radiometer incorporates a microprocessor which controls the system and performs the communications using a digital serial protocol RS-232. The microprocessor waits for external measurement inquiries such as brightness antenna, internal match load or physical temperature measurement.

As the platform is moving, the direction that the antenna beam is pointing, and therefore the radiation that it senses, depends on the attitude of the aircraft with respect to a horizontal reference system (Fig. 3-3). Consequently, in order to properly geo-reference the data acquired, the appropriate positioning and attitude sensor must be selected to determine

the correct antenna footprint. For this purpose the X-sens unit MTi-G is the ideal sensor, because it combines a GPS receiver and attitude sensors; its main characteristics, are presented in section 3.3. In addition, the MTi-G unit has a serial interface to provide the data.

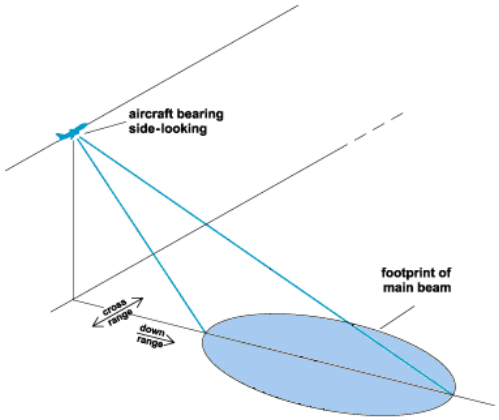

Fig. 3-3: Footprint position regarding to the aircraft attitude

Having on the digitally interfaced radiometer and MTi-G unit, an embedded computer is used to synchronously acquire the information provided for both sensors. This is the aim of the aircraft controller, writing a program which should be capable of running on an embedded computer and acquiring synchronously data from both sensors.

3.2 Analysis of the plane attitude

Using a simple definition, attitude is the orientation of an aircraft with respect to the horizon. This is a function of three angles: pitch, roll and yaw. The pitch angle specifies the orientation of the aircraft's longitudinal axis, that is, whether the nose is pointing upwards or whether it is pointing downwards. The roll angle specifies whether the aircraft is banked left or right, or whether its wings are parallel to the horizon. The yaw angle specifies if the aircraft is derivate to the left or right with respect to the speed vector. These 3 angles constitute rotation around X, Y and Z as it can be seen on the Fig. 3-4 below:

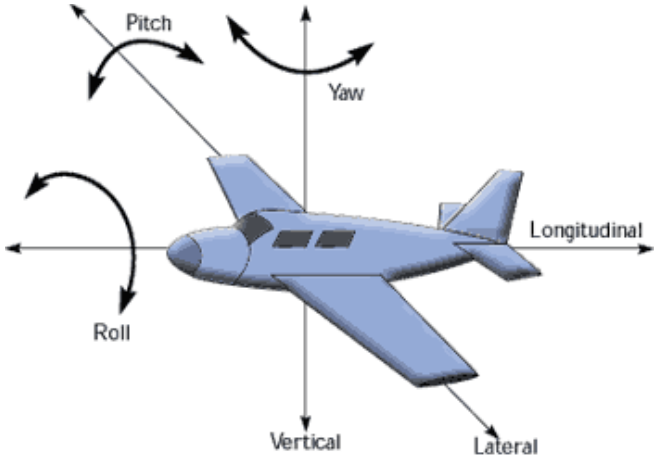

Fig. 3-4. Movement of the plane pitch, roll and yaw.

Pitch, roll and yaw are provided by embedded sensors on the aircraft. These sensors give information about the inclination and the direction of the aircraft with respect to the local Earth magnetic axis.

3.3 The MTi-G sensor

The MTi-G [9] (Fig. 3-4) consist of a GPS aided MEMS based IMU and static pressure sensor.

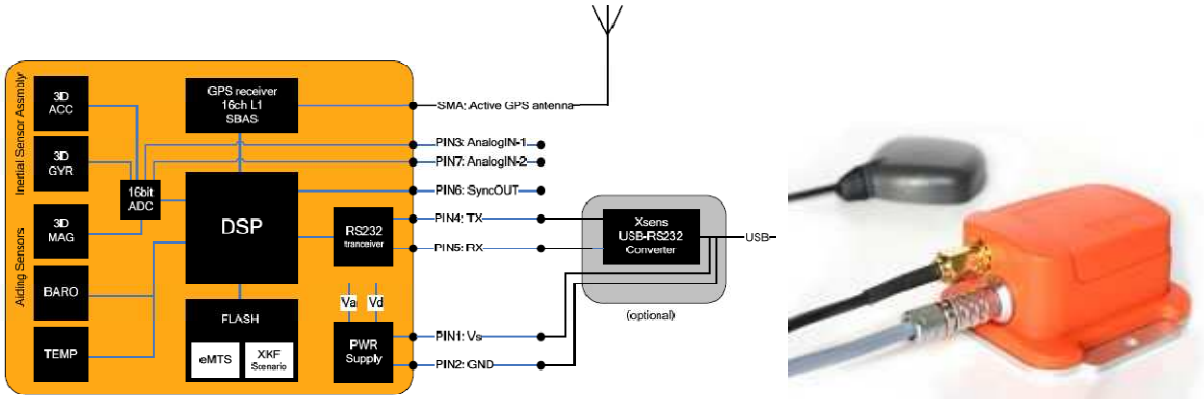

(a) (b)

Fig. 3-4 : MTi-G sensor from X-sens. (a) Functional sketch of the system where the main systems are displayed, such as the DSP, GPS receiver, gyroscopes, magnetometers, accelerometers, barometer…. (b) Overview of the MTi-G system packaged.

The MTi-G's IMU sensors consist of 3 axis magnetometers, 3 axis accelerometers and 3 axis gyroscopes. The data is collected and processed in real-time, with the sensor embedded DSP which runs a sensor fusion algorithm providing enhanced attitude/heading and inertial enhanced position/velocity data. To ensure the data accuracy each sensor is individually calibrated for temperature to detect any 3D misalignment and sensor cross-sensitivity. Finally, another fundamental characteristic of this sensor is the serial digital communication interface (RS-232) that provides a maximum update rate of 120 Hz, which exceeds the instrument requirements (f_s=10 Hz).

Among other detailed properties, listed before and summarized in the Table 3-1, the key features that makes this sensor ideal for boarding in a radio control airborne system are the MTi-G maximum operation limits, an altitude of 16 km and a speed of 515 m/s, which are more than enough for this application, and its small dimensions of 58x58x33 mm weighting only 68 g.

Table 3-1. Range, accuracy and resolution for the MTi-G sensor

For the 3 axis	Gyroscope	Accelerometer	Magnetometer	Barometer
Full Scale (standard)	± 300 deg/s^2	± 50 m/s²	± 750 mGauss	30-120 kPa
Linearity	0.1% of FS	0.2% of FS	0.2% of FS	0.5% of FS
Bias stability (1σ)	1 deg/s	0.02 m/s²	0.1 mGauss	100 PA/yr
Scale Factor stability	-	0.03%	0.5%	-
Noise	0.05 deg/s/√Hz	0.002 m/s²/√Hz	0.5 mGauss (1σ)	4 Pa/√Hz (0.3 m/√Hz)
Alignment error	0.1 deg	0.1 deg	± 750 mGauss	-

The X-sens company provides to the user two different ways to interface the MTi-G through the serial protocol RS-232, one is using a high abstraction level layer and the other is the so called low-level communication protocol. The high-level layer uses dynamic libraries provided by X-sens for C/C++ programming languages. The low-level layer is the one that has been chosen for this project due to the possibility to control the different communication stages and its lower complexity. The low-level communication protocol [10] defines the bytes for each communication word and the structure of the back answer generated by the MT.

Independently of the communication layer, the MTi-G is a high-complex two-state state machine, i.e. Config and Measurement states. In the Config state some settings can be read and written while in the Measurement state the MTi-G will output its data message which contains data depending on the current configuration. There are two different ways to enter the Config state or the Measurement state. At power-up the MTi-G starts the WakeUp procedure and sends the WakeUp message. If no action is taken the device enters the Measurement State. But if the WakeUpAck message is sent within 500 ms after reception of the WakeUp message the MTi-G enters in the Config state. Prior to entering the Measurement State, the Configuration message is always sent to the computer. This is the configuration that is read from the internal non-volatile memory and is used in the Measurement state. The data in the Configuration message can always be used to determine the output mode and settings. Another way to enter the Config or Measurement State is to use the GoToConfig or GoToMeasurement messages while the other state is active.

3.3.1 MT messages

As it has been stated before, the MTi-G is a complex instrument that can be inquired and set a specific configuration or request though a serial port. This can be done using the so called MTi-G commands, MTComm messages. Moreover the MTi-G responses are transmitted fitted in the structure called MTData message, both the MTComm and the MTData have the following predefined structure.

Fig. 3-5 : MTComm and MTData messages structure

Although the datagram structure shown in Fig. 3-5 has 6 predefined containers, the value and length of each one can vary depending on the specific MTComm message, the main characteristic of each datagram part is described in Table 3-2.

Table 3-2. Detailed information for the MTi-G sensor commands

Field	Field width	Description
PREAMBLE	1 byte	Indicator of start of packet 250 (0xFA)
BID	1 byte	Bus identifier or Address 255 (0xFF)
MID	1 byte	Message identifier
LEN	1 byte	Value equals number of bytes in DATA field. Maximum value is 254 (0xFE)
DATA	0–254 bytes	Data bytes (optional)
CHECKSUM	1 byte	Checksum of message

Among other possible commands, in this project only the ones that have been used to configure or inquire the MTi-G system are described in detail.

3.3.1.1 GoToConfig

This command switches the active state of the device from Measurement State to Config State. This message can also be used in Config State to confirm that Config State is currently the active state. This command has the MID container to 48 and it doesn't carry any DATA. The command has been used as it is shown at Fig 3.6:

0xFA	0xFF	0x30	0x00	-	0xD1

Fig. 3-6: The GoToConfig message that has been used.

3.3.1.2 SetOutputMode

This command is only valid when the system is in Config State. It sets the output mode of the MT. The settings here, combined with the SetOutputSettings, define the content of the DATA field in the MTData message. The output mode can be set to various output modes most of which can be combined, for example calibrated sensor data and orientation data. The un-calibrated raw inertial data output however can not be used together with any of the other

outputs. This command has the MID container to 208 and it carries 2 bytes of DATA. The command has been used as it is shown at Fig 3.7:

0xFA	0x01	0xD0	0x02	0x00,0x3E	0xEF

Fig. 3-7: The SetOutputMode message that has been used

Sending this configuration message the output provided by the MTi-G is the GPS PVT data (Position, Velocity, Time and barometric pressure) as it can be seen in the Table 3-3.

Table 3-3. Detailed information for the DATA content of the SetOutputMode message.

MODE bits	Output Mode
Bit 0	Temperature data
Bit 1	Calibrated data
Bit 2	Orientation data
Bit 3	Auxiliary data
Bit 4	Position data
Bit 5	Velocity data
Bit 11	Status data
Bit 12	GPS PVT data (Position, Velocity, Time and barometric pressure)
Bit 14	RAW inertial data (16-bit ADC values) (Can only be combined with GPS PVT data)

3.3.1.3 SetOutputSettings

This command is only valid when the system is in Config State. It sets the current output settings. This command has the MID container to 210 and it carries 2 bytes of DATA. The command has been used as it is shown at Fig 3.8:

0Xfa	0x01	0xD2	0x04	0xD1, 0x00, 0x08, 0x06	0x1B

Fig. 3-8: The SetOutputSetting message that has been used

Sending this configuration message the output provided by the MTi-G is going to be time stamped using GPS Coordinated Universal Time (UTC) time and the orientation matrix

3.3.1.4 SetPeriod

This command is only valid when the system is in Config State. It sets the PERIOD value of the MTi-G, where PERIOD is an unsigned 16-bit value indicating the length of the period. Resolution is in (1/115200) seconds, i.e. 8.68 us. The minimum value is 100 Hz and maximum value is 512 Hz. This command has the MID container to 4 and it carries 2 bytes of DATA. The command has been used as it is shown at Fig 3.9:

0xFA	0x01	0x04	0x02	0x04, 0x80	0x75

Fig. 3-9: The SetPeriod message that has been used

Sending this configuration message the output provided by the MTi-G is going to be updated with a rate of 512 Hz.

3.3.1.5 SetOutputSkipFactor

This command is only valid when the system is in Config State. The MT outputs the MTData at a rate that is not only depending on the sampling frequency but also on the OutputSkipfactor. Normally this factor is zero and the MTData message is sent (1 / sampling period) times per second. A value higher than zero corresponds to how many times the MTData message is NOT sent to the host. This command has the MID container to 212 and it carries 2 bytes of DATA. The command has been used as it is shown in Fig 3.10:

0xFA	0x01	0xD4	0x02	0xFF, 0xFF	0x2B

Fig. 3-10: The SetOutputSkipFactor message that has been used.

Sending this configuration message the output provided by the MTi-G (MTData) is never going to be sent automatically. It only will be send when it would be inquired.

3.3.1.6 GoToMeasurement

This command is only valid when the system is in Config State. It switches the active state of the device from Config State to Measurement State. The current configuration settings are used to start the measurement. This command has the MID container to 16 and it doesn't carry any DATA. The command has been used as it is shown in Fig 3.11:

0xFA	0xFF	0x10	0x00	-	0xF1

Fig. 3-11: The GoToMeasurement message that has been used

By sending this configuration message the output provided by the MTi-G is going to start to measure but as it has been explained it will not provide any MTData because the automatically sending information option has been deactivated.

3.3.1.7 ReqData

This command is only valid when the system is in Measurement State. This message is used to ask the MT to send data to the host. This command has the MID container to 52 and it doesn't carry any DATA. The command has been used as it is shown in Fig 3.12:

0xFA	0x01	0x34	0x00	-	0xF1

Fig. 3-12: The ReqData message that has been used

By sending this message the MT is going to provide a measurement sending back a MTData package.

3.3.1.8 MTData

This message is generated by the MT and it contains the output data depending on the current OutputMode and OutputSettings. This message has the MID container to 50 and the

data field can contain multiple data outputs, but the order of outputs is always the same. The command has been used as it is shown in Fig 3.13:

0xFA	0x01	0x32	0x00	-	0xF1

Fig. 3-13: The MTData message that has been used

If not specifief, each DATA value is 4 bytes long and corresponds with the single-precision floating-point value as defined in the IEEE 754 standard (float).

3.3.2 Packaging

The MTi-G sensor has to be embedded aboard of the aircraft, not the position, neither the packaging nor the orientation are trivial when the sensor is attached.

The sensor has to be carefully installed to avoid strong vibrations from the engine (around 6 g), that otherwise will saturate the sensors (Fig. 3-14).The sensor is totally covered by high density foam and enclosed in a box, the main function of the foam is to absorb the vibrations of the engine, but meanwhile it allows monitoring the movements of the aircraft.

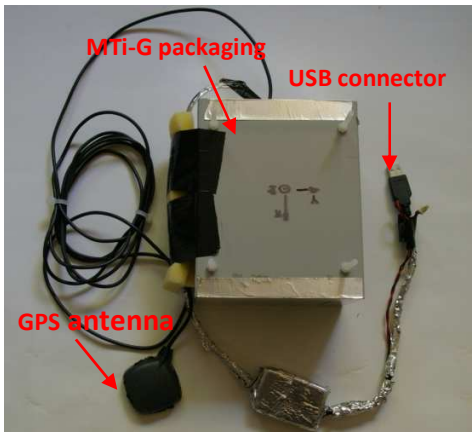

Fig. 3-12 : MTi-G packaged

When positioning the box aboard the aircraft, the axes of the aircraft have to be collinear to the axes of the MTi-G.

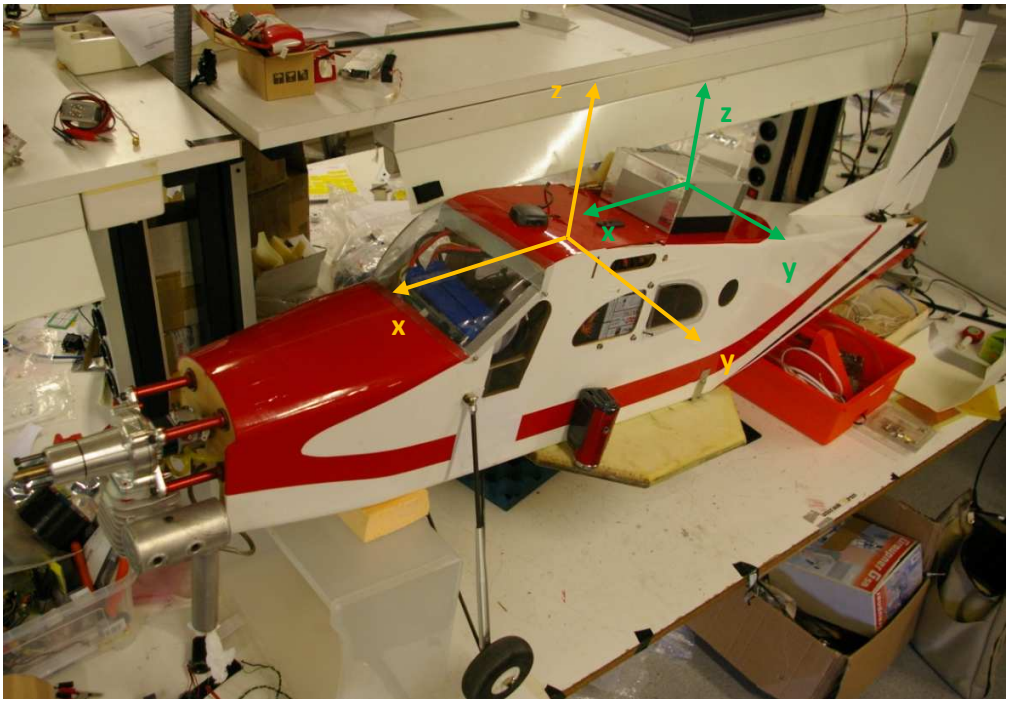

Fig. 3-13 : Axes direction of the MTi-G in green and the aircraft in orange

3.4 The radiometer

The ARIEL radiometer block diagram is shown in fig 3-16. The heterodyne receiver is divided in three main blocks: the RF front-end, the down-converter, and the detection block. Using to the Dicke switch, the RF front-end can switch between the antenna signal and a matched load. Then, the signal is properly filtered, amplified, and down-converted to baseband where it is detected using an rms-to-dc converter (output voltage proportional to signal's standard deviation) and a square law amplifier. Finally the signal is synchronously demodulated, low-pass filtered and conditioned for the analog-to-digital converter.

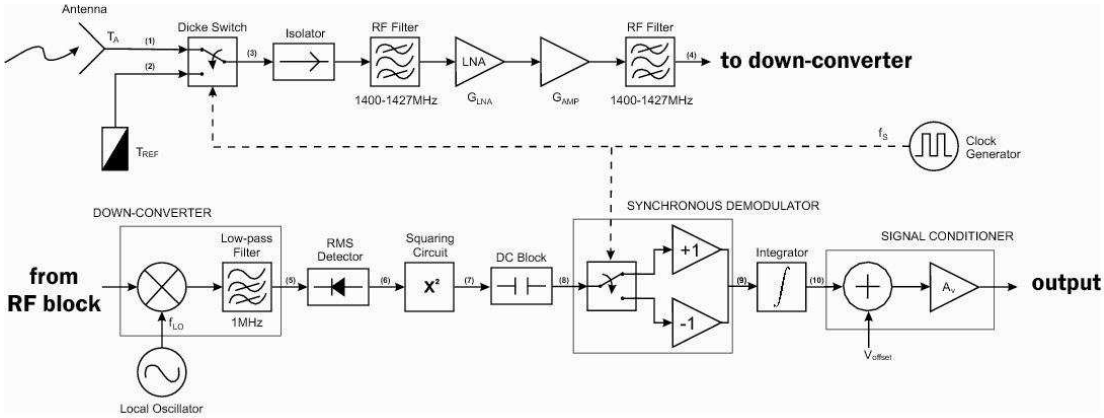

Figure 3-16. ARIEL Block Diagram

When the clock generator, which controls the Dicke switch and the synchronous demodulator, generates a periodic squared signal with a high frequency (about 120 Hz) the system is working as a Dicke radiometer. If not, when the clock doesn't oscillates and has an static high or low value the system is working in a TPR configuration, looking to the antenna (clock stopped at '1') or to a matched load (clock stopped at '0') that is used as an internal calibration reference. So, by enabling or disabling the Dicke clock, it is possible to have a Dicke radiometer or a TPR topology. Choosing which one is the most suitable depends on the application and on the system stability, for example considering a high stable system a TPR topology will provide measurements with a lower level of noise than a Dicke radiometer. By default the radiometer is set in the TPR topology (Dicke clock stopped).

As stated in chapter 2, the radiometric resolution of a balanced Dicke radiometer is $\Delta T = \frac{2(T_{REF} + T_{REC})}{\sqrt{B\tau}}$ and for a TPR is $\Delta T = \frac{(T_{REF} + T_{REC})}{\sqrt{B\tau}}$ where: T_{REF} = 300 K is the reference load physical temperature, T_{REC} is the receiver's noise temperature (T_{REC}=790 K), B = 27 MHz is the system bandwidth and τ is the integration time. Knowing that the maximum integration time is 100 ms, which is determined by the minimum dwell time (smallest footprint / maximum flight speed). With these parameters the theoretical radiometric resolution is ΔT_{Dicke}=1.2 K and ΔT_{TPR} = 0.6 K.

The radio-frequency (RF) front-end of the radiometer was implemented using “off-the-shell” components, but it has to be light-weight and of small dimensions to be installed in a small aircraft. The whole sensor was integrated in a 10x6x1.5 cm monoblock box (Fig. 3-16), and the total weight including the antenna and radome weight less than 2 kg. If the thermal control of the radiometer is included, the total power consumption of the system is less than 10 W (4 W without the thermal control), therefore Lithium Polymer batteries are suitable for being used as power suppliers.

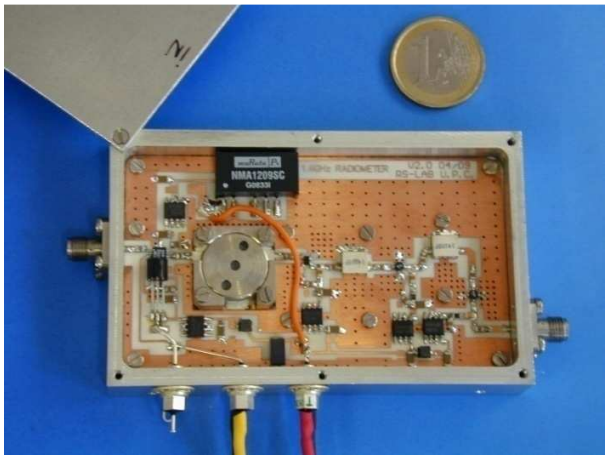

Figure 3-16. ARIEL RF front end compared to 1 euro coin.

3.4.1 Main radiometer commands

The onboard system has a microcontroller (PIC-18F4520) which interfaces the radiometer with any external device using a set of possible inquires and the RS-232 serial protocol. The main functions of the microcontroller are managing the switch (Dicke clock) and to digitizing the signals, which are quantified using a 16 bits and fast external analog to digital converter (ADC) through the serial protocol interface (SPI).

As in the case of the X-sens MTI-G, an easy and simple communication protocol has been defined to communicate the radiometer and the external master device. Basically, the microcontroller has a slave configuration: it digitizes the signals systematically and if an external

inquire is received this is attended by sending the corresponding answer. Table 3-4 provides detailed information about the possible requests and the corresponding radiometer answer.

Table 3-4. Detailed information of the communication protocol between the radiometer and a computer. Note that bytes are written in hexadecimal format.

Parameter	Request Byte	Response Word
T_A	0xAA	0xAB; 0xMSB-T_v; 0xLSB-T_v; 0xMSB-T_h; 0xLSB-T_h;
T_{ref}	0xAC	0xAD; 0xMSB-T_{refv}; 0xLSB-T_{refv}; 0xMSB-T_{refh}; 0xLSB-T_{refh};
T_{ph_ref}	0Xae	0xAF; 0xMSB-T_{phv}; 0xLSB-T_{phv}; 0xMSB-T_{phh}; 0xLSB-T_{phh};
T_{int}	0xB0	0xB1; 0xMSB-T_{int}; 0xLSB-T_{int}; 0x00; 0x00;
T_{ext}	0xB2	0xB3; 0xMSB-T_{ext}; 0xLSB-T_{ext}; 0x00; 0x00;
T_{A_Dike}	0xB4	0xB5; 0xMSB-T_v; 0xLSB-T_v; 0xMSB-T_h; 0xLSB-T_h;

The request always consists of one byte and the answer consists of a 5 bytes word. The first byte that the radiometer sends back is the request byte plus one, having a function of sending preamble, datagram identification and handshake. So, when the brightness antenna temperature (T_A) is requested (request byte = 0xAA) the radiometer switches the input to the antenna (Dicke clock = static 1) and the answer word is composed by the handshake byte, 16 bits for the vertical antenna and 16 bits for the horizontal antenna, in total a 5 bytes word . Although the current system has only one polarization antenna looking to nadir, the communication protocol has been thought to use two polarization antenna or two different antennas to give more versatility to the system. When there is only one antenna the second data measurement is sent zero filled. The data information is sent packaged in 2 bytes, first the radiometer sends the most significant byte (MSB) i.e. from bit 16 to 8, and then it sends the less significant byte (LSB) i.e. from bit 7 to 0.

When the reference temperature (T_{ref}) is requested (Request byte = 0xAC) the radiometer switches the input to the matched load (Dicke clock = static 0) and the answer word is composed by the handshake byte, 16 bits for the vertical matched load and 16 bits for the

horizontal matched load. When there is only one matched load the second part of the measured information is sent zero filled.

When the physical reference temperature (T_{ph_ref}) is requested (Request byte = 0xAE) the ADC input is switched to the matched loads thermal sensors and the answer word is composed by the handshake byte, 16 bits for the vertical physical matched load reference temperature and 16 bits for the horizontal physical matched load reference temperature. When there is only one matched load the second part of the measured information is sent zero filled.

When the physical internal temperature (T_{int}) is requested (Request byte = 0xB0) the ADC input is switched to the internal monoblock box thermal sensor and the answer word is composed by the handshake byte and 16 bits for the physical internal temperature and 16 zeros.

When the physical reference temperature (T_{ext}) is requested (Request byte = 0xB2) the ADC input is switched to the external monblock box thermal sensor and the answer word is composed by the handshake byte and 16 bits for the physical external temperature and 16 zeros.

When the brightness temperature of the Dicke's topology (T_{Dicke}) is requested (Request byte = 0xB$) the Dicke clock switches at 120 Hz and the answer word is composed by the handshake byte, 16 bits for the vertical Dicke's output and 16 bits for the horizontal Dicke's output. When there is only one matched load the second part of the measured information is sent zero filled.

3.5 The software driver

This section focuses on the developed software (Fig. 3-17) to manage the radiometer and the MTiG sensor synchronously acquiring and providing a unique file where all the collected information is packaged for further data processing.

Since now, the attitude and position sensor and the radiometer have been presented, but it remains another essential device located onboard the aircraft that is the computer that manages the information provided by the sensors. The onboard computer is an embedded computer with a Windows XP operative system which has lots of programming tools to create drivers for controlling simultaneously both sensors. Taking into account the time and money costs of every field campaign performed to get measurements, the most critical design criteria parameters are the safety and the reliability, the safety is ensured by avionic system redundancy and the expertness of the pilot, the reliability should be ensured writing a trustable code that is not going to slow down the system neither hang up. Although at the beginning of this project the driver software was though to be written in MatLab, this option was changed to C# for many reasons, the most important is that despite MatLab is a really good tool for fast prototyping code it is not a fast processing and reliable code when system's peripherals, e.g. the serial port, are involved. So that, the controller driver was written in C# using the Microsoft tool Visual Studio 2008.

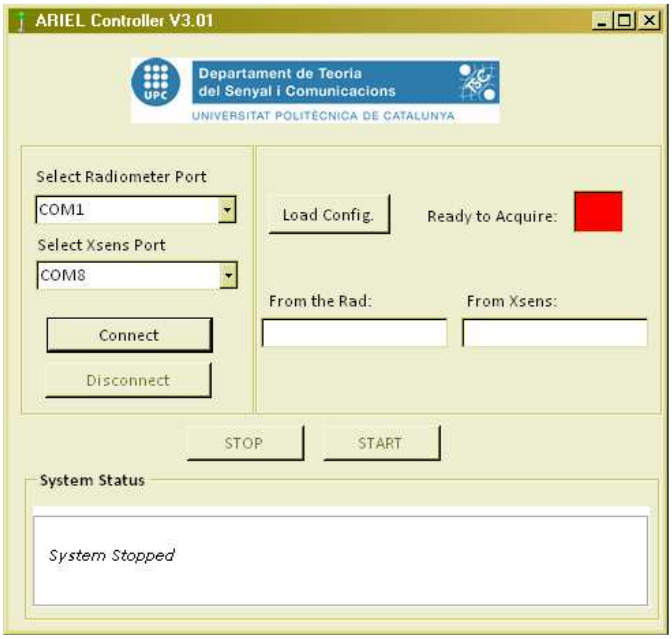

Fig. 3-17. Graphical interface of the system driver which manages and controls the radiometer and the MTi-G sensor.

Figure 3-17 shows the user friendly graphical interface of the controller, on the top left has two combos where it is possible to select the Radiometer and the MTi-G serial port, this is very useful and gives flexibility to connect the system in the desired port depending on the needs of each system configuration. Furthermore, the MTi-G is connected to the PC through a Universal Serial Bus (USB) port but appears to the operative system as a simply serial port, the number assigned to this new serial port depends on the total number of existent ports and how many USB devices are already connected, so that is a good idea to give to the user the possibility to choose the serial port where the system is connected. On the bottom of that part there are two buttons, “connect” and “disconnect” which open or closes the serial port.

At the top right there is a button labeled with “Load config.” This button loads a defined configuration file for the radiometer that determines the working mode, Dicke or TPR, and the relative frequency of the antenna and the matched load measurements. Moreover, there is a label “Ready to Acquire” which has a color code, when is red it means that the system is not capable of acquiring data, when it is orange it means that the system can acquire data but some information is missing and finally, when it turns to green it means that all the information is available and the system is ready to start the acquisition. On the bottom of this part there are two text boxes labeled “From the Radiometer” and “From Xsens”, here are displayed in real time the answers of the system when the driver is checking their information availability.

In the middle of the graphical interface there are two buttons labeled “STOP” and “START” which, once the connection has been established by opening the respective ports, the “START” button starts the acquisition sequence by setting the proper MTi-G configuration and checking the availability and coherence of the data provided by the system. On the other hand, the button “STOP” finalizes the acquisition.

At the bottom of the graphical interface, there is a text box labeled as “System Status” where all the incidences of the system are displayed, such as the status of the system, the number of acquisitions that have been done since now, etc.

3.5.1 Algorithm description

Behind the graphical interface there is the synchronization and acquisition algorithm that is the driver itself. This algorithm follows an easy and intuitive flow chart (Fig. 3-18) as a finite state machine. When initialize the software the first state is the INIT status where the driver waits for an external connection (by pushing the "Connect" button), then the system opens the serial ports and creates a new file with a characteristic and unique name which consist of a character string composed of the year, month, day, hour, minutes, seconds and milliseconds. Once this is done the software waits for the START button.

If the button START is pushed the system goes from INIT status to the VALIDATION mode. The aim of this state is to check that both instruments, the MTi-G and the radiometer, are ready to start the acquisition. First, the software sends the configuration sequence to the MTi-G and analyzes its answers to find out if they make sense, in addition, the driver validates if the GPS coordinates are coherent or not. If they are not, the system flags the acquisition as not full ready to acquire, that it means that the readiness box is orange and a big warning text appears at the top of the graphical interface. Although the inertial and GPS data are crucial for the geo-referencing and correcting the aircraft attitude, it was decided to not stop the acquisition if the test was not successfully passed, the reason is that in case of the user wants to test the radiometer and at that moment it doesn't has the attitude sensor, the user can follow on. The next step is to validate the radiometer, if the test is passed the ACQUISITION mode starts, if not the state goes to INIT again and displays a warning text. Once the radiometer test is passed the system goes automatically to the ACQUISITON mode where the radiometer and the MTi-G are periodically interrogated following a defined pattern to speed up the acquisition.

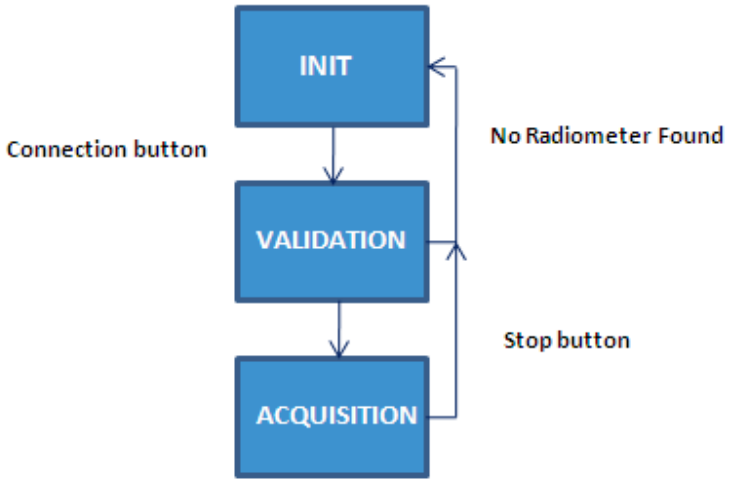

Fig. 3-18. Flight controller driver flow chart

To find the best instrument configuration it was necessary to analyze the delays and identify the stronger restrictions. The first theoretical approach was as follows: the radiometer transmission speed is 56 Kbps and it transmits 5 bytes per answer is an approximated transmission time of 0.7 ms per answer. The MTi-G transmission speed is 109 Kbps and it transmits a maximum of 120 bytes per answer these results with an approximated transmission time of 8.8 ms, by following this analysis the maximum delay between two consecutive radiometric samples is 9.5 ms, but this does not take into account other delays as the ones related to the operative system.

After this theoretical discussion a measured delay test was performed to determine the operative system delay that must be taken into account. The measured time required for the operative system to send a data to the MTi-G, the time needed to get the answer, the time for analyzing if it is consistent and writing it in a raw data file is all about 20 ms, which corresponds to a sample rate of 50 Hz. When both instruments are connected and the system inquires and waits for each answer sequentially, the delay is about 50 ms, which corresponds to a sample rate of 25 Hz. Another possible configuration is to inquire an instrument and instead of waiting for the answer inquire the next instrument, and finally collect both answers, analyze them and write them in a recording file. The best results following this strategy were obtained inquiring the radiometer, inquiring the MTi-G, reading the MTi-G, reading the radiometer and,

finally, storing the data. The total measured delay was 31.25 ms, which corresponds to a sample rate of 32 Hz. At the same time, the radiometric inquires follows the pattern established in the load configuration file switching between antenna, matched load and reference physical temperature. If there is no specific configuration it loads the default one.

The system remains in the ACQUISITION mode forever, unless the button STOP is pressed, then the system closes the collected file and waits in the INIT mode for another acquisition.

3.5.2 Brief analysis of the main functions

In this section the most important functions used in the driver are briefly analyzed to complement and extend the understanding of the algorithm description of the previous section. Not to say that there are other useful functions to handle the graphical interface properly, for example to attend the buttons or to thread the program to keep on attending the graphical interface to disconnect the acquisition mode. These functions are not required to understand this work, so they have been excluded in the following analysis.

public int SendWord2Xsens(byte[] CmdBytes, int id)

This function is used by other functions to send words to the Xsens' MTi-G hardware, it ensures the communication waiting for the answer if the handshake byte is not correct or the transmission is timeout, it waits for 50 miliseconds and sends the word again. As input requires the word to be send (*CmdBytes*) and the flag *id* for control issues. The output is 1 if it is succesfull, or 0 if, after all, the system cannot succeed with the communciation.

public Boolean CheckGPS()

This function is used in the VALIDATION mode to test the Xsens instrument. It sends a set of configuration and request words waiting for the answer, if the handshake is correct then it checks the GPS coordinates, that sould be different of longitude 0 and latitude 0. If any of both tests fails the output is 0, if it is successfull the output is 1.

public Boolean CheckRadiometer()

This function is used in the VALIDATION mode to test the radiometer instrument. It sends a set of configuration and request words waiting for the answer, if the handshake is correct then the output is 1, if not is 0.

public void XsensInit()

This function is used in the INIT mode to initialize and configure the Xsens using the *SendWord2Xsens()* function.

public void XsensAcquire(string s, int flag)

This function is used in the AQUISITION mode to inquire and read the answer of the Xsens' MTiG device. The inputs are *s* which is the specific comand word to ask for a measurements and flag used to mark a particular acquisition, when for example some other event occurs. Once the coherence of the collected answer has been checked, this function time stamps the acquisition and writes all the information in the raw data file.

public void RAD_Request(byte CmdByte)

This function is used in the AQUISITION mode to inquire the radiometer. The input is *CmdByte* which selects the measurement to be done by the radiometer according to the Table 3-4. The main difference between *RAD_Request()* and *XsensAcquire()* is that the *RAD_Request* does not wait for neither reads the radiometer answer, there is another specific function for that task.

public void RAD_Acquire(byte CmdByte)

This function is used in the AQUISITION mode to read the radiometer answer. This function uses the same time stamp done in the *XsensAcquire()* linking each MTiG acquisition to a unique radiometric acquisition, achieving the syncronization between both instruments. Once the coherence of the collected answer has been checked it, writes all the information to the raw

data file, including the byte *CmdByte* to be able to discern in the recorded file between different types of radiometric answers.

3.5.3 The raw output file

As stated in the previous section, all the collected data with no distinction from which sensor has been generated is written into a raw ASCII text file. This file is opened automatically when the button "connect" is pressed, and the name of the file is automatically generated following the current time, to avoid overwriting files and have a clear reference of when the file was created. Furthermore, the file extension is ".dat" which means that it contains data information.

Table 3-5. Detailed information of the content of the raw data file.

Sensor	Header	Datagram
MGi-T	h m s ms Type	Roll Pitch Yow Lat Lon h V_x V_y V_z FLAG
Radiometer	h m s ms Type	T_{av} T_{ah} T_{ph_v} T_{ph_h} 0 0 0 0 0 FLAG

The file generated is the input of the processor software. In order to simplify the loading task in the processor, this file is organized in rows and columns as is shown in Table 3-5. Each new acquisition is written in a new row and each row has exactly the same number of columns (15), which is easy to load to MatLab. Due to the acquisition strategy explained before, the rows content switch between MTi-G and radiometer acquisitions. Two consecutive rows, MTi-G - Radiometer, are considered to be acquired in the same instant, so they are simultaneous. Data coming from the radiometer is codified following the Table 3-4 and in any case the switching row pattern is kept.

In Table 3-5 the header is composed by h (hour), m (minute), s (second), ms (millisecond) and Type (which provides information about the datagram part: 0 means MTi-G datagram, 1 for antenna temperature, 2 reference temperature, 3 physical temperature and 8 Dicke mode). As explained the datagram depends on the Type value, if it is a MTi-G datagram the information contained is: Roll, Pitch and Yaw, which are the three attitude angles, Lat and

Lon, the current coordinates, h, the current height, V_x, V_y and V_z, which is the velocity vector decomposed in the three axes, and FLAG which indicates that in this current time an special event has occurred. On the other hand, the radiometric datagram is composed by T_{av} and T_{ah} which can be the antenna temperatures or the reference matched load temperatures depending on Type, T_{ph_v} and T_{ph_h}, are the physical temperatures of the matched loads, internal or external, depending on Type. After that, it follows five zeros only to match the length of columns of this row with the number of columns of the MTi-G row, and finally, there is FLAG with the same meaning than in the MTi-G datagram.

3.5.4 Test Mode

There is a test mode version of the controller to test the radiometer and the Xsens' MTi-G sensor. Mainly the test mode version has an extra window (Fig. 3-19) where recorded data is displayed in real time. It is useful to detect and identify external interferences, generated by the aircraft's systems or from other systems nearby.

Although this real time displayer had been considered to be included in the main design from the beginning of the project, it was rejected because the displayer slows down the acquisition system and the acquisition rate goes from 33 Hz to 10 Hz. This drawback can be afforded in a test mode, but not during the acquisition flight, when the goal is to record as much data as possible. So that, there are two different programs.

In order not to maintain two different versions of the same software, this mode has been implemented using a compiler label. By changing the Boolean value of this label the software includes the test mode or not.

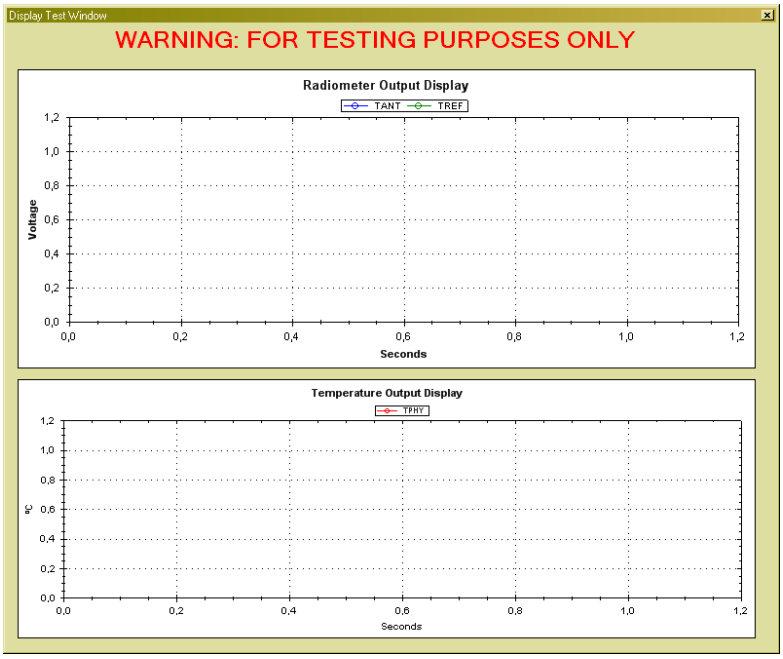

Fig. 3-19. Real time radiometric output display

3.6 Conclusions

This chapter has focused on the onboard instruments needed to create a map from an airborne platform and their synchronous acquisition. First, the MGi-T has been analyzed giving its main features and a glimpse to its working modes and configuration has been provided. Then, the radiometer has been presented giving the features and characteristics, giving an overview over the communication radiometric protocol. On the other hand, the software that controls both instruments has been explained and detailed.

4 ARIEL Processor

As it was said in the introduction, the aim of this project is to obtain brightness temperature maps from which soil moisture and vegetation content could be retrieved. Therefore, it is necessary to implement various procedures and algorithms which will process raw data acquired from sensors. Figure 4-1 shows the whole ARIEL system sketch, this chapter focuses on the red-dotted rectangle part in the right hand side.

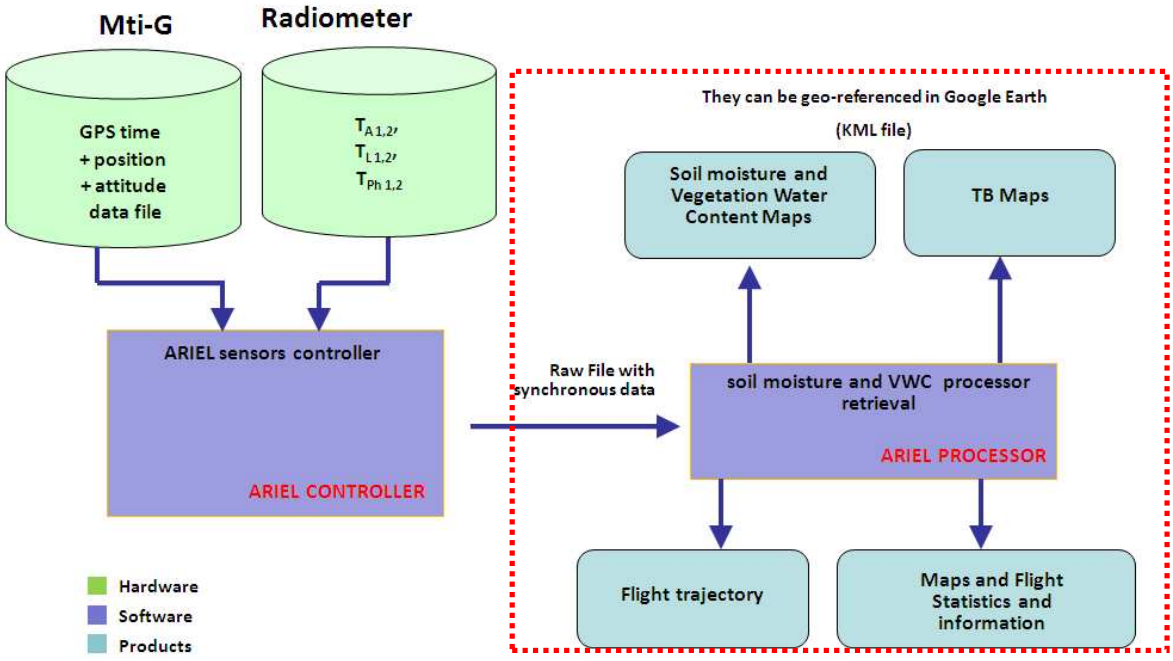

Fig. 4-1 : ARIEL system sketch.

While chapter 3 focused on the onboard instruments and on the software to control the acquisition (left part of Fig. 4-1). This chapter focuses on the ground segment processing, once the aircraft has landed and the data has been download from the embedded computer. This processor software has been written in MatLab and designed to fulfill the entire data processing

from the raw data file to the retrieved product maps that could be displayed over Google Earth maps.

A graphical user interface (GUI) is proposed to allow an easy and fast way to obtain flight information. The main steps of the method used to recover soil moisture and vegetation content are explained (Fig. 4-2):

- read and load the raw data file under processing, discerning between different data types,
- automatic calibration of the radiometer output data,
- projection of the antenna footprint to the Ground,
- soil moisture and vegetation content retrieval from the projected brightness temperature maps, and
- display information in several formats: graphs, histograms, trajectory maps, footprints maps, interpolation maps, error maps...

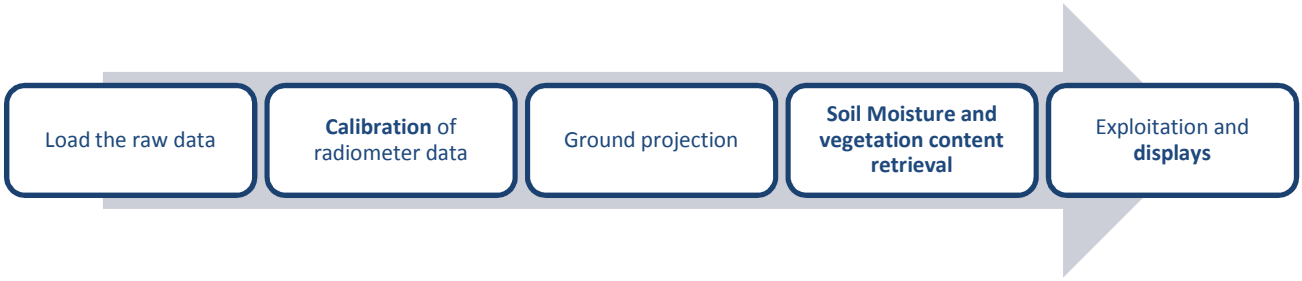

Fig. 4-2 Mains steps of data processing

4.1 Calibration of the radiometer response

4.1.1 Introduction

Once the file has been loaded and the different data types have been spitted into the corresponding arrays, the radiometric data has to be calibrated. The aim of the calibration step is to convert the radiometer's output voltages into antenna temperatures. As the radiometer

ARIEL onboard the aircraft is usually set as a TPR, the relationship between its output voltage and the antenna temperature can be expressed as Eqn. 4.1 [8]:

$$v_0 = aT_A + b \tag{4.1}$$

where:

- T_A is the antenna temperature and
- *a* and *b* are gain and offset to be determined during calibration.

Therefore, a set of two well known pairs *(v_o, T_A)* has to be measured to be able to calibrate the system assuming that the radiometric response is linear within the interval where it has been calibrated. Usually, the first pair is found pointing the antenna to a cold load: the sky. Then the observed voltage corresponds to ≈6 Kelvin, radiation of the sky and the atmosphere at L-band. The other pair is taken when the antenna is pointing to a hot load (a microwave absorber) and T_A corresponds to the ambient temperature (≈300 K), which is taken as the reference. These classical procedures are not practical in the current system, since it is boarded in an aircraft. It is not possible to turn around the aircraft for pointing the sky, neither to put a microwave absorber in front of the antenna to measure the hot load.

The problem of the hot load has been solved by adding an internal matched load and a switch at the radiofrequency input (i.e. Dicke switch at Fig. 3-16), as stated in chapter 2, a matched load generates the same amount of noise as a black-body at the same physical temperature. The main problem of this technique is that despite the receiver chain of the radiometer is being calibrated the antenna losses are not, which can be solved by characterizing it losses and by thermal stabilization of the antenna to minimize temperature fluctuations.

A not easy-to-solve problem is the cold load pair. Two different and complementary solutions have been considered to overcome this problem. The first one consists of flying over a fresh water mass during the acquisition campaign. Generally, fresh water has a characteristic and well-known brightness temperature at nadir (≈100 K) that can be used as a cold load, but this is not always practical or feasible to include this over flight into the scheduled flight route. If

it was not possible then there is still the second possibility: using laboratory accurate calibration coefficients. Previous to board the system in the aircraft, the hot (microwave absorber) and cold load (sky) have been measured obtaining the calibration coefficients, taking into account the whole receiver chain. If there is no information about the cold pair calibration, these stored values are used.

To track gain fluctuations of the radiometer and to compensate them, the Dicke switch alternates periodically the measurement of the antenna and the reference load. Tracking the reference matched load fluctuation is possible to track the system's gain fluctuation. So that, the time measurement ratio between the antenna and the matched load is a parameter that can be changed by the user (through the configuration file, chapter 3) and depends on the stability of the instrument.

The algorithm automatically looks for the pairs $\left(v_0^{hot}, T_A^{hot}\right)$ and $\left(v_0^{cold}, T_A^{cold}\right)$ in the raw data. To do that, it must locate the calibration measurement on the radiometric raw data file. The hot load is easy to find because it has a specific label in the raw data file as stated in section 3.5.3. If there is any cold load, it corresponds to the highest value of the output voltage of the radiometer. To accept that any measured interval can be associated to the cold load calibration, a four level quality test has to be checked by the algorithm:

- ensure that the considered interval has a minimum length (several seconds),
- the voltage difference between the internal hot load and the considered interval has to be the expected one (corresponding to $\sim 100K$),
- the radiometric output has to be stable enough ($\sigma_{T_A} < 2\,K$, ensuring that the measurement is only fresh water), and
- it has to occur in both polarizations,

these precautions avoid using as cold reference any interfered or wrong measurement.

The equations system formed by two calibrations points is then solved and the constants *a* and *b* are found (Eqns. 4.2 and 4.3).

$$a = \frac{(v_0^{hot} - v_0^{cold})}{(T_A^{hot} - T_A^{cold})} \tag{4.2}$$

$$b = v_0^{hot} - a.(T_A^{hot}) \tag{4.3}$$

where T_A^{hot} is the physical temperature of the radiometer matched load, it has been measured with the thermometer onboard during the measures of the hot load($T_A^{hot} \sim 300\ K$). T_A^{cold} is the expected brightness temperature when the radiometer is pointing to a fresh water mass ($T_A^{cold} \sim 100\ K$, depending on the polarization and incidence angle).

Finally, a set of calibrated antenna temperatures *(T_A)* can be obtained (Eq 4.4). These measurements are not yet surface brightness temperatures as they are affected by the antenna main beam efficiency (MBE) and they also have the contributions from the atmosphere, Sun reflections, etc.

$$T_A\ (t) = \frac{v(t) - b}{a} \tag{4.4}$$

Furthermore, it can occur that the radiometer does not have a linear behavior due to physical temperature changes or other non linear variations. That is why the coefficients *a* and *b* in Eq. 4.1 are not constant during the flight. In order to measure this evolution, the hot load is measured periodically by setting the Dicke switch to '0'. From each of these periods a new *a(t)* and *b(t)* are determined, by updating the hot load measurement.

4.1.2 Calibration example

To illustrate what it has been explained in the previous section, two examples with synthetic data are shown. Synthetic data means that the raw data file has been created by a MatLab radiometer and a MTi-G emulator, not from the real system. This emulator has been

very useful during the test of the ARIEL processor. Mainly, it has avoid waiting for real data to start testing.

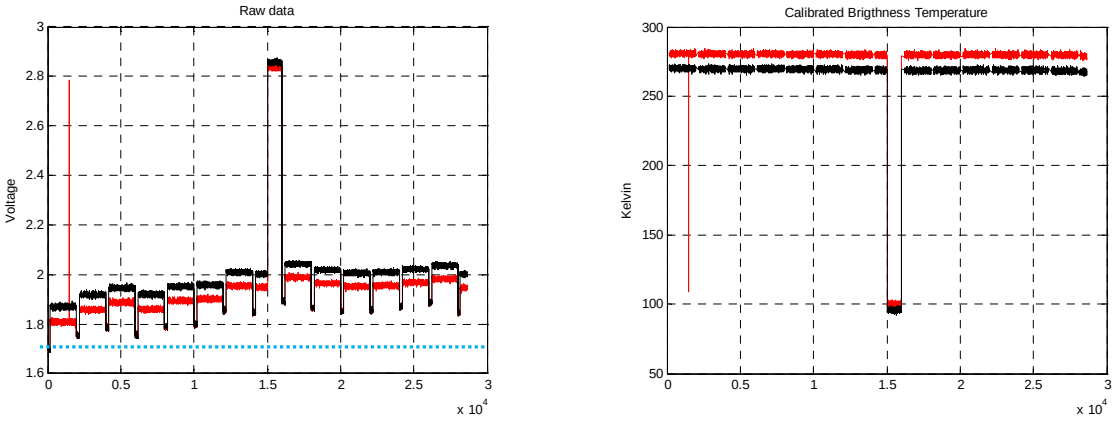

(a) (b)

Fig. 4-3 Calibration example (a) Raw data file, two polarization radiometer's voltages output, (b) calibrated measurement without the internal hot load measurements. Note that the interference it has not been assumed as a cold load.

Figure 4-3 shows a raw data file display, where two polarization radiometer's voltages have been plotted, the red is the horizontal and the black the vertical polarization. The plot starts with a hot load measurement and continues with antenna measurements, following this pattern periodically. This pattern is the system standard measurement pattern, followed by the real raw data files. The blue dotted line shows the radiometer's gain fluctuation (differences between the blue dotted line and the internal hot load measurements).

In this first example has been simulated that the flying route passes over fresh water mass, the algorithm detects this event and uses it as a cold load. Also, there is an interference, but this is not interpreted as a cold load event by the ARIEL processor, because it is too short and only appears in one polarization.

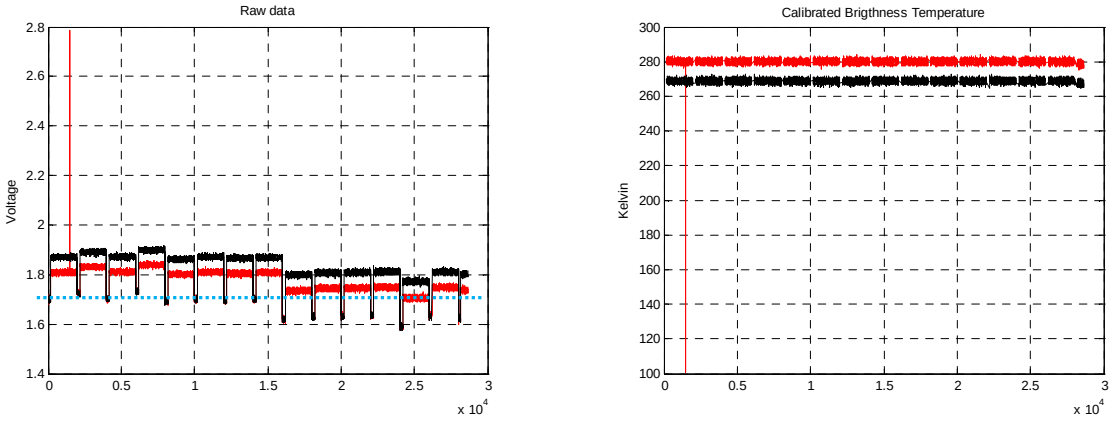

(a) (b)

Fig. 4-4 Calibration example (a) raw data file, two polarization radiometer's voltage output without a water mass measurement, (b) calibrated measurement without the internal hot load measurements. Note that the interference it has not been assumed as a cold load.

Figure 4-4 shows another raw data file display, where two polarization radiometer's voltage has been plotted, the red is the horizontal and the black the vertical polarization. The blue dotted line shows the radiometer's gain fluctuation. The plot has the same measurement pattern than in Fig 4-3. In this second example, it has been simulated that the flying route do not passes over fresh water masses, the algorithm detects this lack of cold reference and uses the stored values. As in the previous example, the interference is not interpreted as a cold load.

4.2 Display of the antenna footprints

On the way to achieve soil moisture or vegetation water content maps it is necessary to obtain brightness temperature maps. In the previous section it has been shown how to convert the radiometric voltage output to brightness temperature using the radiometric calibration T_{hot}-T_{cold}. The next step is to plot the measured brightness temperature over a map using the flight attitude information, knowing the shape and the orientation of the projected footprint. In order to reach this aim, some algorithms have been implemented using mathematical and remote sensing theory, which are going to be presented in the following paragraphs. Actually, they expose the two mains steps to succeed to plot the shape of the footprint: firstly, how determine

the position pointing by the antenna and secondly, the method to specify the shape of the footprint.

4.2.1 Specification of the antenna pointing

The radiometric data acquired by the antenna depends on where the antenna is pointing at. This is why the attitude of the platform is an important issue. The attitude is defined by 3 angles: pitch, roll and yaw (Fig. 4-5).

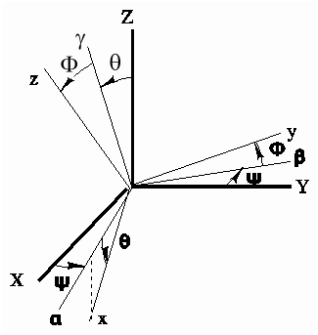

Fig. 4-5 : Attitude angles, Ψ : yaw, rotation around z, Θ : pitch, rotation around y and Φ : roll, rotation around x

These three angles define the position of the platform respect to the local Earth system of coordinate. In order to position the centre of the antenna boresight, a change of coordinate is necessary to pass from the aircraft body and Earth coordinate frame as shown in Fig. 4-6. The system (x', y', z') represents the aircraft, (x, y, z) the local Earth system at the altitude of the platform and finally (x'', y'', z'') its projection over land. The position A represents the point which has to be specified. The first step is to find the direction of the antenna boresight named $\vec{Z}_b$ in the Fig. 4-6.

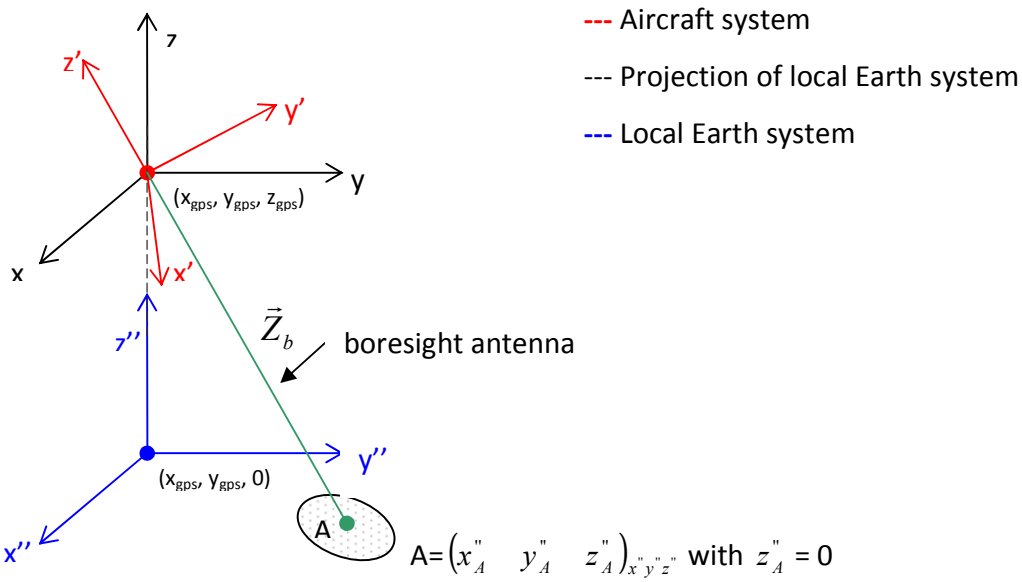

Fig. 4-6 : System of coordinates

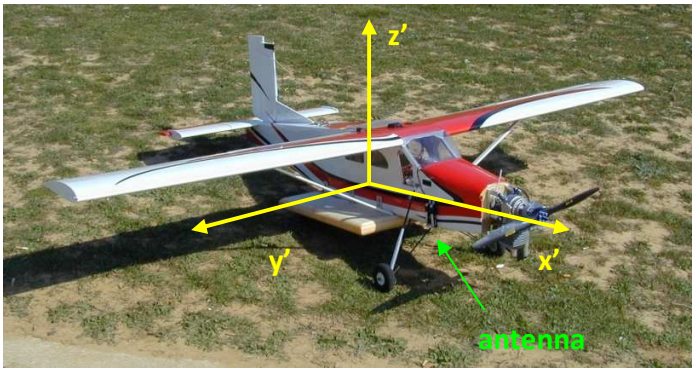

Fig. 4-7 : Coordinate system of the radio control aircraft

As the coordinate system of the aircraft is defined in Fig. 4-6, it appears that the antenna direction is the opposite direction of z'. On the one hand, by using the matrix passage P from the system (x, y, z) to (x', y', z'), and on the other hand, by projecting the vector z' in (x, y, z), the coordinate of this vector is accessed as it is explained below. The first step is to find the direction of $\vec{Z}_b$ in the coordinate frame (x, y, z). The position of the aircraft, referenced by (x_{gps}, y_{gps}, z_{gps}), corresponds to the position provided by the GPS system aboard of the platform. With $\vec{X}'$ = (0, 0, -1)$_{x'y'z'}$ and $\vec{Z}_b$ =(x_b, y_b, z_b)$_{xyz}$ and the transformation matrix $P_{x'y'z'\to xyz}$:

$$\overline{\overline{P}}_{x'y'z'\to xyz} = \begin{bmatrix} \cos\phi\cos\psi & \cos\phi\sin\psi & -\sin\phi \\ -\sin\psi\cos\theta+\cos\psi\sin\phi\sin\theta & \cos\psi\cos\theta+\cos\psi\sin\phi\sin\theta & \sin\theta\cos\phi \\ \sin\psi\sin\theta+\cos\psi\sin\phi\cos\theta & -\cos\psi\sin\theta+\sin\psi\sin\phi\cos\theta & \cos\theta\cos\phi \end{bmatrix} \quad (4.15)$$

with the following elements: ϕ = roll, θ =pitch and ψ =yaw. Then operating mathematically

$$\vec{X}' = \overline{\overline{P}}\cdot\vec{Z}_b\,, \quad (4.16)$$

and finally the projection relationship is achieved (Eqn. 4.17):

$$\vec{Z}_b = \overline{\overline{P}}^{-1}\cdot\vec{X}'. \quad (4.17)$$

The second part of the calculation specifies the coordinate of the point A using a coordinates translation from (x, y, z) to (x'', y'', z''). As the equation of a curve in the system (x,y,z) containing the vector $\vec{Z}_b$ is of the type (Eqn. 4.18). Then if the same reasoning is made for the system (x'', y'', z''), the curve equation resulting is Eqn. 4.19, hence the system of equations is (Eqn. 4.20):

$$\frac{x-0}{x_b} = \frac{y-0}{y_b} = \frac{z-0}{z_b}, \quad (4.18)$$

and

$$\frac{x''_A - x_{gps}}{x_b} = \frac{y''_A - y_{gps}}{y_b} = \frac{z''_A - z_{gps}}{z_b}. \quad (4.19)$$

As z''_A = 0, from (Eqn. 4.18) and (Eqn. 4.19), the following solution is found:

$$\begin{cases} x''_A = \dfrac{-z_{gps}}{z_b} \times x_b + x_{gps} \\ y''_A = \dfrac{-z_{gps}}{z_b} \times y_b + y_{gps} \end{cases} \tag{4.20}$$

Finally the coordinates of A, position of the centre of the antenna footprint, are found. Knowing this information, it is necessary now to determine the shape of the footprint.

4.2.2 The shape of the antenna footprint

4.2.2.1 Antenna characteristics

In order to specify the shape of the footprint, the pattern of the antenna has to be studied. The antenna is a hexagonal 7-patch array with a 22° beam and a Main Beam Efficiency over 90% (Fig. 4-8), that is thermally controlled.

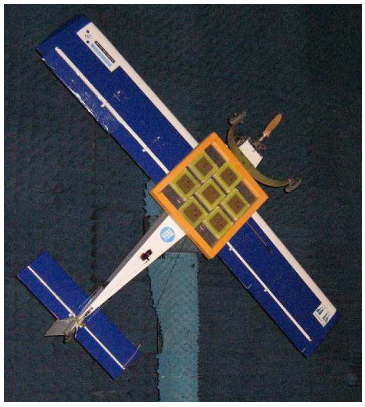

(a)

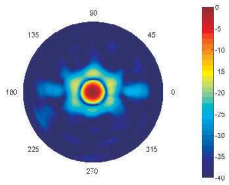

(b)

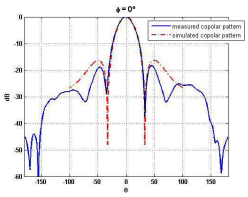

(c)

Fig. 4-8 (a) Antenna pattern measurement mounted on the plane at the anechoic chamber of the Dept. of Signal Theory and Communications, Universitat Politècnica de Catalunya, (b) measured full radiation pattern, and (c) Copolar radiation pattern at E-plane.

It is well known that the projection of a footprint of this type of antenna is an ellipse. So that, its parameters have to be calculated using the altitude and attitude information. Figure 4-9 underlines the shape of the footprint and the incidence angle. This angle then has to be projected over ground in order to know how position the ellipse.

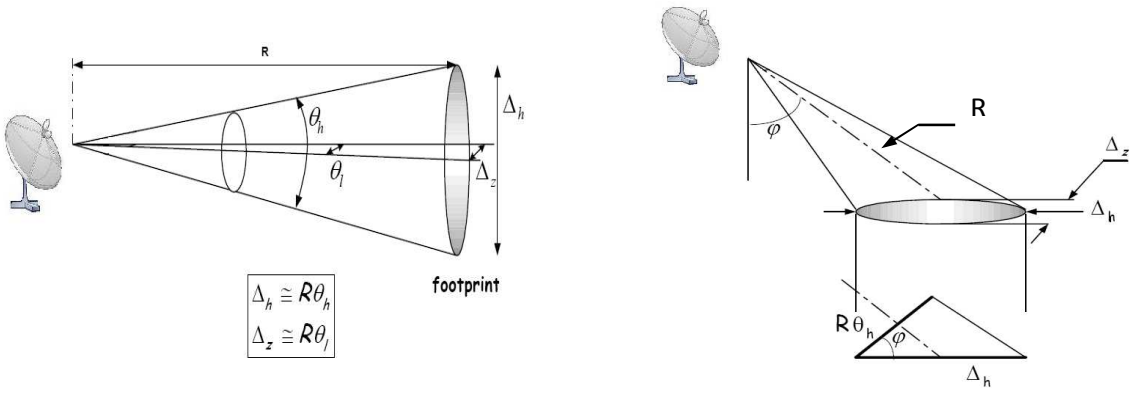

(a) (b)

Fig. 4-9 Antenna's footprint projection (a) Footprint as a function of the height and the antenna's beamwith (b) footprint as a function of incidence angle with the Eq. 4.21, 4.22 and 4.23

$$\Delta h = \frac{R^2 \Delta\theta}{h}; \tag{4.21}$$

$$\Delta z = R\Delta\theta \text{ and} \tag{4.22}$$

$$R = \sqrt{(x''_A - x_{gps})^2 + (y''_A - y_{gps})^2 + z_{gps}{}^2}\ . \tag{4.23}$$

4.2.2.2 Ellipse theory

An ellipse is defined by the semi-major axis *a* and the semi-minor axis *b*, centered at the point *(h,k).* Having its major axis parallel to the x-axis, it may be specified by the equation:

$$\frac{(x-h)^2}{a^2} + \frac{(y-k)^2}{b^2} = 1\,. \tag{4.24}$$

This ellipse can be expressed parametrically as:

$$x = h + a\cos t\,, \tag{4.25}$$

$$y = k + b\sin t\,, \tag{4.26}$$

where *t* is restricted to the interval $-\pi \le t \le \pi$. In the particular case, where the axes of the ellipse are not parallel to the x and y axes, the parametric form of an ellipse rotated counter clockwise by an angle ϕ is more adequate:

$$x = h + a\cos t\cos\phi - b\sin t\sin\phi \tag{4.27}$$

$$y = k + b\sin t\cos\phi + a\cos t\sin\phi \tag{4.28}$$

Using these formulas, it will be easy to draw an ellipse with the semi mayor axis *a*, the semi minor axis *b*, and the position of the centre of the ellipse are already known. Indeed these parametric formulas calculate a set of points; the ellipse can be then approximated by connecting the points with lines. One interesting consequence of using the parametric formula is that the density of points is greatest where there is the most curvature. Thus, the change in slope between each successive point is small, reducing the apparent "jaggedness" of the approximation. According to what it has been said before, most of the parameters are known except the angle ϕ: the projection of the incidence angle. In order to specify it, the dot product theorem has to be applied (Fig. 4-10).

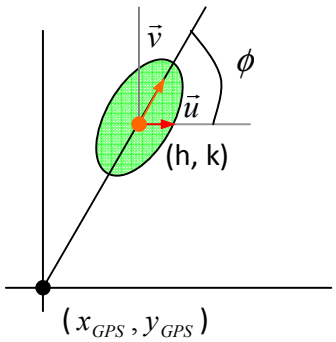

Fig. 4-10 : Scalar theorem to determine the incidence angle

If $\vec{u}$=(1,0,0) and $\vec{v}$=(h-x_{GPS} k-y_{GPS},0), then:

$$\cos\ \phi = \frac{\vec{u}.\vec{v}}{\|\vec{u}\|.\|\vec{v}\|}. \tag{4.31}$$

Finally, all the needed parameters to specify ellipse shape and orientation are determined.

4.3 Data merging and interpolation

Once the radiometer outputs have been calibrated into antenna temperatures, the flight trajectory has been determined, as well as the footprint size and shape, it is the turn to compose antenna temperature maps. Radiometric data has to be properly processed to obtain a geocoded map, which can be linked to a KML file to be overlaid with Google Earth maps.

For geo-statistical applications the Kriging method [10] provides the optimal interpolation, if it is applied with right criteria. The value of each point is assigned by adding all the contributing points weighted accordingly to a data-driven weighting function (spatial covariance values obtained through the semivariogram analysis). When the region is homogeneous the weights still high for far contributing points. It makes possible to create an accurate and extended grid by filling the gaps that the aircraft has not flight over. It is important to note that in the most cases is not possible to assume that the region is heterogeneous, only if it is a very small area. Otherwise, when the region is heterogeneous, which is generally the case specially in agricultural fields, the weights are zero for points far away and very small for closer points, which makes impossible to fill all the gaps interpolating. When the region is especially heterogeneous, with agricultural fields, buildings, roads and man-made structures the semivariogram gives no correlation between adjacent points which makes the Kriging method useless. Although the Kriging method was considered at the beginning of this project, it was later discarded, as well other interpolation methods, and a different approach has been implemented. The implemented algorithm merges different footprints that overlap an area, so that is based on a high level of measurement overlapping.

In the alternative method finally implemented by the algorithm, a modified two dimensional (bivariate) Gaussian function is taken as approximation of the antenna pattern, which is a common approximation. This bivariate function weights the footprint, the center having more impact than the edges. The weighting function of each footprint has been adjusted to ensure that at the edges of the footprint the weighting function value has fall to half the maximum value (-3 dB in antenna terms). Then, a fine pixel grid is defined, the separation between pixels is the spatial resolution that it can be defined by the user, and it can be as fine as required. Actually, the pixel spatial resolution depends on the number of footprints that overlaps in a pixel, no more information is going to be added due to a finer grid is applied, only repeated values will be obtained.

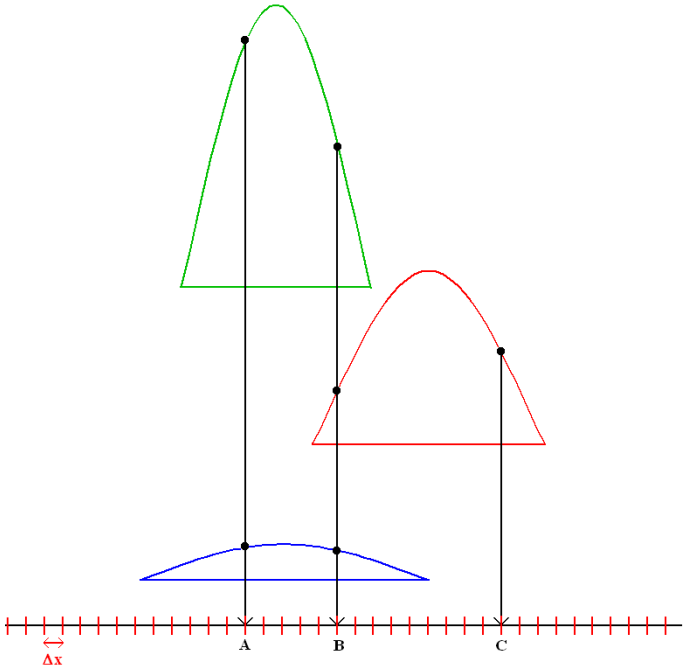

Fig. 4-11: *y*-cut of the two dimensional data merging algorithm. There is three footprints, green, blue and red. The red grid is the pixel along the x axis and Δx is the spatial resolution. Each pixel is calculated by merging the weighted overlapping footprints.

Finally, the merged value is obtained (Fig. 4-10) by computing the distance between the centers of the pixel to all the center footprints. A footprint overlaps a pixel, so it contributes to each final value, only if the computed distance is lower then the footprint radius. The computed distance is used to weight the footprint value thought its weighting function and finally all the

values are added and divided by all the weighting contributions to do not change the mean value (Eqn. 4.32).

$$Z_i = \frac{\sum_{k=1}^{n} W_k(d_k) \cdot Z_k}{\sum_{k=1}^{n} W_k(d_k)} \tag{4.32}$$

where:

- Z_k is the value of the k^{th} contributing antenna footprint,
- Z_i is the estimated value for the pixel i^{th},
- d_k is the distance to the center of the pixel to the center of the k^{th} contributing antenna footprint,
- W_k is the Gaussian weighting function of the k^{th} contributing antenna footprint, and
- n is the total number of contributing footprints.

In this procedure the footprints generated at lower altitudes (those which are smaller) have a higher influence on the obtained pixel, and as much close to the center of the footprint the weight is higher and the contribution increases significantly.

Following the example shown in Fig. 4-11, the pixel A is composed by the green and blue footprints, the green contribution is higher because is closer to the center and the footprint is smaller as well. Pixel B is composed by the three footprints and the pixel C only by the red footprint. Each pixel can be obtained by adding an arbitrary number of footprints (depends on the overpasses), the more contributing footprints more reliable is the pixel. Because of this difference of reliability a map of number of averages per pixel should be provided to show how the generated map is created.

Other configurations have been tried to optimize this method, such as enlarging the footprint from -3 dB to -6 dB, in this particular case the problem was that the resulting image was smoother (at the limit the map will have only one value with the mean of all the brightness temperatures), it is the same problem of using a Kriging in a heterogeneous area.

4.4 Soil moisture and vegetation water content retrieval

Once the processor is able to compute antenna tempreature images merging all the contributive footprints the soil moisture (SM) and vegetation water content (VWC) are retrieved using the two polarization information. In this section, the principles used in order to retrieve soil moisture ad vegetation water content from the antenna temperature and the underlying assumptions are explained.

4.4.1 Preliminary assumptions

Usually, retrieving SM and VWC is an ill posed problem, which means that there are more input parameters required than available data, and independent measurements. To simplify the algorithm and to be able to retrieve these parameters, the algorithm takes into account the following working assumptions:

- Assumption 1 (the geophysical assumption): in this approach, the soil is considered to be smooth (surface roughness = 0), the elevation of the terrain, the soil type and soil temperature are constant within the whole spatial range of the flight. A further analysis on the error increasing when this assumption is not fulfilled is provided in the following.

- Assumption 2 (the polarimetric assumption): the nadir antenna only takes into account the horizontal polarization while in the fore-looking antenna the polarization is vertical. This assumption is true when the aircraft attitude angles are within small fluctuations from its reference axis. If not, the measurement of each antenna is a combination of the vertical and horizontal polarizations. To ensure this assumption a roll and pitch filter can

be applied to discard acquisition samples that do not fulfill this requirement, with a maximum allowed fluctuation of ±10^{o}.

- Assumption 3 (the radiation assumption): As stated in Fig. 2-4, the brightness temperature of the surface is measured by an antenna far away. In this case, the apparent temperature T_{AP} is the key parameter that depends on the brightness temperature of the surface under observation (T_B), the atmospheric upward radiation (T_{UP}), the atmospheric downward radiation scattered reflected by the surface (T_{SC}), and the atmospheric attenuation (L_a). The downward radiation is mainly generated by the cosmic radiation level of the sky T ≈ 2.7 K at L-band, and the downwelling atmospheric contribution T_{DNatm} ≈ 2.1 K at zenith. These values are fairly constants and will not affect the quality of the measurement and are usually ignored. Since T_{UP} ≈ 0 K at low altitudes (which is right for SM applications but not for SSS), T_{SC} is much smaller than the required accuracy and L_a ≈ 1 (for $\theta = 0^\circ$), at low altitudes, So that, the apparent temperature T_{AP} at L-band is approximated by the temperature emitted by the surface (T_B) weighted by the antenna pattern.

4.4.2 Retrieval algorithm

There are several possibilities for solving an inverse problem like the one that is faced here. For this application the designed retrieval process seeks at minimizing the following non-linear last-squares function using the two available measurements:

$$\chi = \alpha \left[\left(e_v - e_{v,model} \right)^2 \right]_{\theta=0} + \beta \left[\left(e_h - e_{h,model} \right)^2 \right]_{\theta=22} \tag{4.33}$$

where:

- e_v and e_h are the measured emissivities, coming from the brightness temperature maps obtained in the previous section divided by the physical temperature (Eqn. 2-16),
- $e_{v,model}$ and $e_{h,model}$ are the modeled emissivities including the antenna pattern,

- $\theta = 0^{o}$ and $\theta = 22^{o}$ are the two beams available in the system, nadir-looking at v polarization and fore-looking at h polarization, and
- α and β are two empirical coefficients to give different weights to different observations in the retrieval. This method is called Tikhonoff regularization and is the most commonly used method of regularization of ill-posed problems. It is related to the Levenberg-Marquardt algorithm for non-linear least-squares problems. It is named after Andrey Tychonoff.

Once the retrieval method has been presented, the next step is to analyze the ill posed problem to clarify the chances to solve it. The measured soil emissivities depend on 8 main parameters:

- the central frequency, the polarization and the incidence angle. Although the emissivity depends on these three parameters, they do not contribute to the ill posed problem since they are design specifications,
- the soil moisture, which is one of the parameters to retrieve,
- h_r, the surface roughness,
- the τ (vegetation opacity), which is related with the VWC,
- ω (vegetation albedo), which is the ratio of scattering efficiency to total extinction efficiency (which is the a sum of scattering and absorption), and
- the soil physical temperature.

For a pencil beam antenna and assuming that the temperature of the vegetation is the same temperature of the soil, the previous parameters are related as it shows in eqn. 4.34, in the well known τ-ω model, which is a valid and simple forward model to be used in optimal estimations approaches:

$$e_p(\theta) = (1-\omega)\left(1-\exp\left(-\frac{\tau}{cos\theta}\right)\right)\left(1+\Gamma_{S,p}(\theta)\exp\left(-\frac{\tau}{cos\theta}\right)\right) + \left(1-\Gamma_{S,p}(\theta)\right)\exp\left(-\frac{\tau}{cos\theta}\right) \quad (4.34)$$

where the reflection coefficient at the air-ground interface ($\Gamma_{S,p}(\theta)$) is computed using the Wang model as [11]:

$$\Gamma_{S,p}(\theta) = \left[(1-Q)\Gamma_{S,p}^{Fresnel}(\varepsilon_r(SM,\dots),\theta) + Q\Gamma_{S,q}^{Fresnel}(\varepsilon_r(SM,\dots),\theta)\right]\exp\left(-h_r cos^n\theta\right). \quad (4.35)$$

Where n is a semi-empirical parameter, Q is the mixing polarization parameter and $\Gamma_{S,p}^{Fresnel}(\theta)$ the Fresnel specular reflectivity of the air-ground interface for the *p* polarization, which depends on the permittivity (ε_r) of the soil and the incidence angle:

$$\Gamma_{S,p}^{Fresnel}(\theta) = \frac{cos\,\theta - \sqrt{\varepsilon_r - sin\theta^2}}{cos\,\theta + \sqrt{\varepsilon_r - sin\theta^2}} \quad (4.36)$$

$$\Gamma_{S,q}^{Fresnel}(\theta) = \frac{\varepsilon_r cos\,\theta - \sqrt{\varepsilon_r - sin\theta^2}}{\varepsilon_r cos\,\theta + \sqrt{\varepsilon_r - sin\theta^2}} \quad (4.37)$$

Where p and q are two linear and orthogonal polarizations and the permittivity is a complex value ($\varepsilon_r = \varepsilon_r^r + j.\varepsilon_r^i$). The real part ($\varepsilon_r^r$) and the imaginary part (ε_r^i) of the permittivity depends on the volumetric content of soil moisture. This dependence is approximated by the Wang model [12]:

$$\varepsilon_r^r = 3{,}1 + 17{,}36 \cdot SM + 63{,}12 \cdot SM^2 \quad (4.38)$$

$$\varepsilon_r^i = 0{,}031 + 4{,}65 \cdot SM + 20{,}42 \cdot SM^2 \quad (4.39)$$

On the other hand the vegetation opacity is defined as the product of the vegetation water content and a constant that depends on the vegetation.

$$\tau = b \cdot VWC \quad (4.40)$$

$$b_{Typ} = 0.14\ [Np/(Kg/m^2)] \quad (4.41)$$

Where Eqn. (4.41) (b=0.14 *Np/(Kg/ m^2)*) has been stated empirically. The selected value is a standard one for agricultural crops, for instance in grass is 0.02 and in forest is 0.33 Np*/(Kg/ m^2)*.

4.4.3 Emissivity equation analysis

Once the equations of the retrieval algorithm has been stated, the emissivitiy of both polarizations has been analyzed following the Eqn. 4-34 and swapping the possible soil moisture values and the vegetation water contennt values (through the vegetation opacity parameter (Eqn. 4.40))

Analyzing Fig. 4-12 it is possible to determine that there is a sensitibility range where it is possible to determinte both parameters, SM and VWC. As spected, SM is more sensitivity (it is easy to retrieve) when there is no vegetation layer (bare soil). When the vegetation starts to grow, the SM sensitivity decreases. It saturates (there is no SM sensitibity or is not possible to retrieve the SM) for values of vegetation opacity higher that 2 Np, which it means that the VWC is higher than 14 Kg/m^2. Despite this it can be seen as a problem, this value is a high value and is only possible to find in some tropical rain forest.

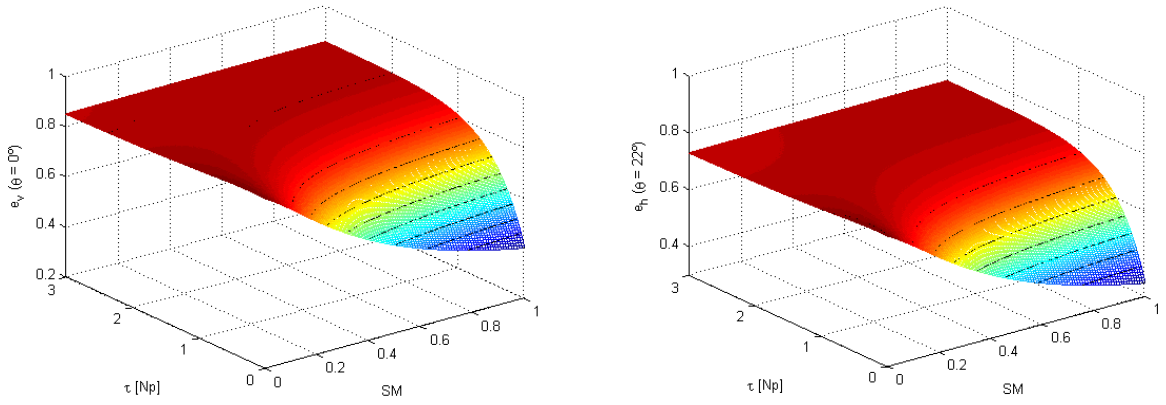

(a) (b)

Fig. 4-12: Emissivity evaluation following the Eqn. 4.34 and swapping the soil moisture and vegetation opacity parameters. (a) evaluation for vertical polarization and 0° incidence angle, (b) evaluation for horizontal polarization and 22° incidence angle.

It is important to say that for nearly all types of crops and forest, the albedo is lower than 0.2 (ω <0.2) and the vegetation opacity is lower than 0.8 Np (τ <0.8 Np). The maximum values corresponds to a vegetation density up to 100 Tm/ha (10 kg/m^2), which is valid for the most type of forest [13].

4.4.4 Solving the minimization equation

Once the retrieval method has been presented, performed by the minimization of two non-linear last-squares functions, and the involved equations have been analyzed, it is time to find an effective method to solve it. The first method studied is a common solution that finds the solution iteratively. It is the Gauss-Newton method. Although this is a widely used method to solve this kind of problems, in this case is not operative because it has to be solved for each obtained pixel and this will take a long time. So that, an intuitive and simpler method has been presented to solve the minimization problem.

4.4.4.1 Gauss-Newton solving method

The Gauss–Newton algorithm is a method used to solve non-linear least squares problems. It can be seen as a modification of Newton's method for finding a minimum of a function. Unlike Newton's method, the Gauss–Newton algorithm can only be used to minimize a sum of squared function values, but it has the advantage that second derivatives, which can be challenging to compute, are not required.

Using the Eqn. 4-33, the method starts with an initial guess (S_0 = (SM_0, VWC_0)) for the minimum, the method proceeds by the following iterations:

$$S_{i+1} = S_i + \Delta \tag{4.42}$$

Where the Δ is the solution to the normal equation:

$$J_r^T J_r \Delta = -J_r^T r \tag{4.43}$$

Where, r is the function and J_r is the Jacobian matrix of r with respect of *S,* both evaluated at S_i. Although this definition it can result strange and difficult to follow at the first glimpse, it is easily implementable in MatLab with just few code lines, computing numerically the solution of the normal equation and the Jacovians. Using a not too strict stop iteration condition, it converges after some iterations and the loop ends. The main problem is when trying to code this algorithm in MatLab, because a loop instruction has to be used and it is well known that despite of MatLab is very fast in matrix computation, it is too slow performing loops. So that, the computation time will increases dramatically and this solution becomes unpractical.

4.4.4.2 Alternative method

After this theoretical solution trial, an easer method to solve the minimization equation has been implemented to be the core of the retrieval algorithm. This method pre-calculates the emissivity for the v and h polarization for all the range of possible SM and VWC values. The results of this calculation are the two matrix plotted at Fig. 4-12. Once the two polarization values are ready for each pixel they are compared to the pre-calculated matrix, the SM and VWC values that better match are the ones assumed to be the correct solution. After some analysis it was concluded that this method is the most efficient and it is as accurate as the iterative method with a resolution determined by the grid size of the precalculated esmissivities. The computation speed increases significantly, no loops are coded now, but two matrices are allocated in the processor available memory.

4.4.5 Validity threshold of the geophysical assumption

To be able to retrieve the soil moisture and vegetation water content it has been mandatory to assume as constant some geophysical parameters that they are not. This section focuses on the validity of these assumptions.

First of all, a simulation to get the brightness temperature for each beam and for each possible pair (SM, VWC), and some extra conditions have been made, and then the retrieval algorithm has been applied. Fig. 4-13 shows the ideal case, the simulation parameters are a ideal radiometer (ΔT_B=0 K), the albedo is constant (ω=0.1), the soil roughness is constant (h_{ref} =0.1) as well and the topography, is flat and it does not change in the whole flight range, and the soil temperature has no variations. The retrieval parameters are the same used in the simulation. As expected the retrieval has no error. To enhance the retrieval analysis, a red-slashed line has been drawn for reference, at 20% in SM and at 1 Np in τ. In Fig 4-13a, the reference follows perfectly the 20% retrieved line for any value of τ. In Fig 4-13b the reference follows perfectly the 1 Np retrieved line for any value of SM.

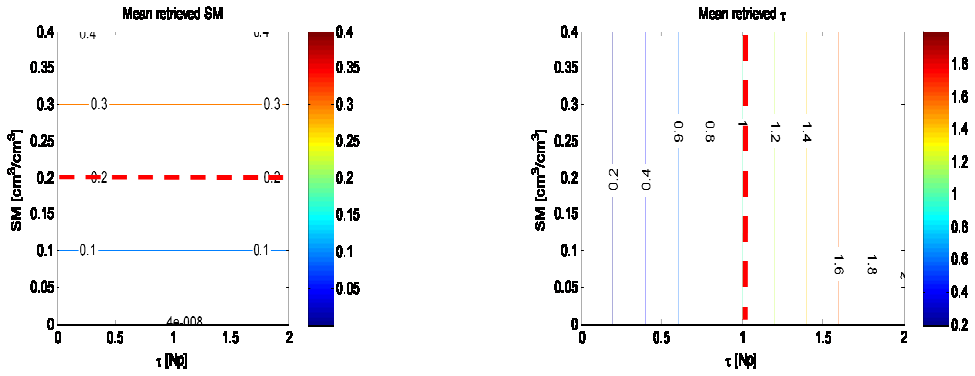

(a) **(b)**

Fig. 4-13: SM and VWC retrieval under ideal conditions (ΔT_B=0 K), ΔT_{ph}=0 K, ω= ω_{ref}=0.1 and h_r = h_{ref} =0.1. The red slashed line is the reference (a) SM retrieval (b) VWC retrieval

Figure 4-14 shows the first non-ideal case, the simulation parameters are a non-ideal radiometer (ΔT_B=0.1 K), the albedo is constant (ω=0.1), the soil roughness is constant (h_{ref} =0.1) as well, the topography is flat and it does not change in the whole flight range, and the soil temperature has no variations. The retrieval parameters are the same used in the simulation. As expected the retrieval has some error. In Fig 4-14a, the retrieved value is lower than the original one for middle values of τ. There is not any trend for low values of τ, and finally the algorithm overestimates the SM when τ is high. The standard deviation of the retrieved SM is high for middle values of τ. In Fig 4-14b the retrieval has a problem for low values of SM and τ. At SM

20% the algorithm underestimates τ. The standard deviation of τ is reasonable for all the retrieval condition. Despite in this case the retrieval works well except for low values of SM and τ, it is important to realize that a radiometer which has ΔT_B=0.1 K is a good performance radiometer taking into account that the integration time is limited by the airplane high and velocity.

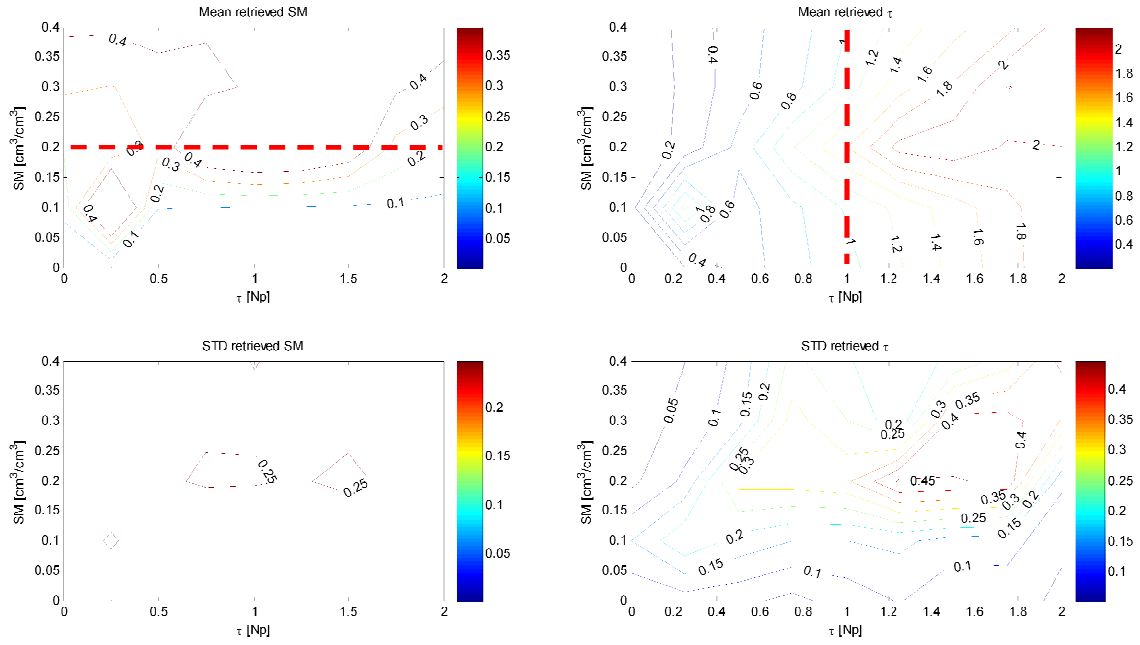

(a) **(b)**

Fig. 4-14: SM and VWC retrieval under non-ideal conditions (ΔT_B=0.1 k), ΔT_{ph}=0 K, ω= ω_{ref}=0.1 and $h_r = h_{ref}$ =0.1. The red slashed line is the reference (a) SM retrieval mean and standard deviation (b) VWC retrieval mean and standard deviation.

Figure 4-15 shows another non-ideal case, the simulation parameters are noisier radiometer (ΔT_B=1 K), the albedo is constant (ω=0.1), the soil roughness is constant (h_{ref} =0.1) as well and the topography is flat and it does not change in the whole flight range, but not the soil temperature that has no variations. The retrieval parameters are the same used in the simulation. As expected the retrieval has important errors. In Fig 4-15a, the retrieved algorithm underestimates SM for low values of τ and overestimates it for high values of τ. The standard deviation of the retrieved SM is high. In Fig 4-15b the retrieval has a problem for any value of SM and τ. It seems that the general trend is to underestimates τ. The standard deviation of τ

has increased for all retrieval conditions. It has been shown that the retrieval limit is when ΔT_B=1 K, for higher values it is impossible to retrieve any parameter without a too significant error in the mean and in the standard deviation.

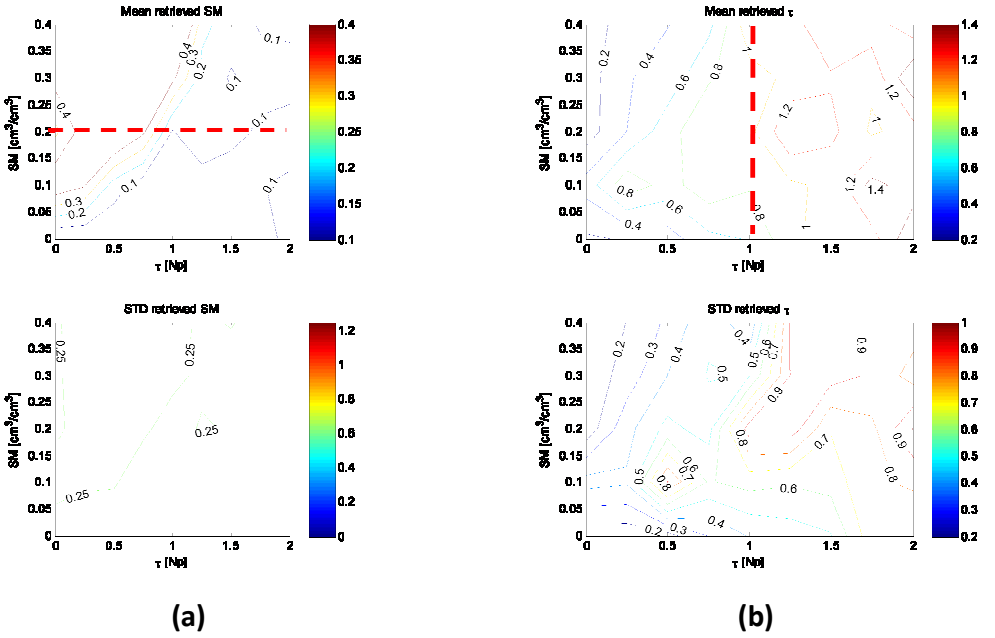

Fig. 4-15: SM and VWC retrieval under non-ideal conditions (ΔT_B=1 K), ΔTp_h=0 K, ω= ω_{ref}=0.1 and hr = h_{ref} =0.1. (a) SM retrieval mean, (b) VWC retrieval mean and standard deviation.

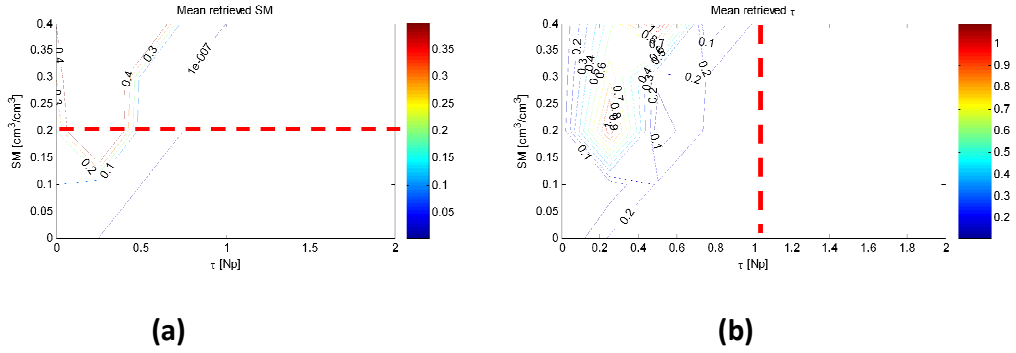

Fig. 4-16: SM and VWC retrieval under non-ideal conditions (ΔT_B=0 K and ΔT_{ph}=2 K) and ω≠ ω_{ref}=0.1 and hr = h_{ref} =0.1. (a) SM retrieval mean, (b) VWC retrieval mean.

Figure 4-16 shows another non-ideal case, the simulation parameters are ideal radiometer (ΔT_B=0 K), the albedo is constant (ω_{ref}=0.1), the soil roughness is constant (h_{ref} =0.1) as well and the topography is flat and it does not change in the whole flight range, but not the

soil temperature that has a variation of 2 K (ΔT_{ph}=2 K). The retrieval parameters are the same used in the simulation except for the albedo that has been assumed as zero (ω=0.1). As expected the retrieval has important errors. In Fig 4-16a, the retrieved algorithm totally underestimates SM. In Fig 4-16b the retrieval has a problem for any value of SM and τ. It underestimates τ as well. It seems that an underestimation of the albedo has a big impact on the retrieval.

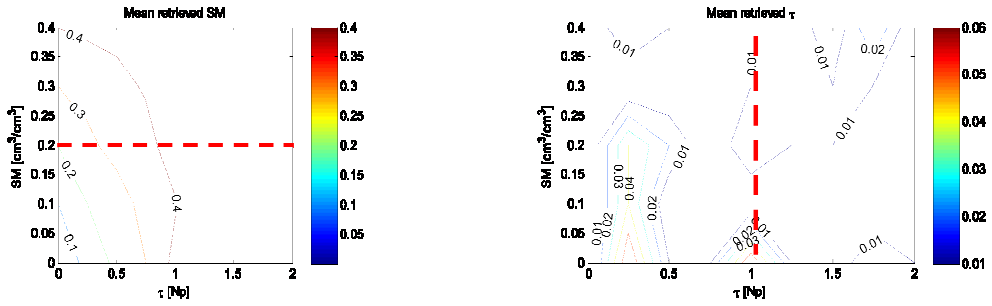

(a) (b)

Fig. 4-17: SM and VWC retrieval under non-ideal conditions (ΔT_B=0 K), ΔT_{ph}=2 K, ω= 0.5 vs ω_{ref}=0.1 and $h_r = h_{ref}$ =0.1. (a) SM retrieval mean, (b) VWC retrieval mean.

Figure 4-17 shows another non-ideal case, the simulation parameters are ideal radiometer (ΔT_B=0 K), the albedo is constant (ω_{ref}=0.1), the soil roughness is constant (h_{ref} =0.1) as well and the topography is flat and it does not change in the whole flight range, but not the soil temperature that has a variation of 2 K (ΔT_{ph}=2 K). The retrieval parameters are the same used in the simulation except for the albedo that has been assumed as 0.5 (ω=0.5). As expected the retrieval has important errors. In Fig. 4-17a, the retrieved algorithm underestimates SM, except for low values of τ. In Fig. 4-17b the retrieval has a problem for any value of SM and τ. It underestimates τ as well. It seems that a good estimation of the albedo is crucial to get a good retrieval.

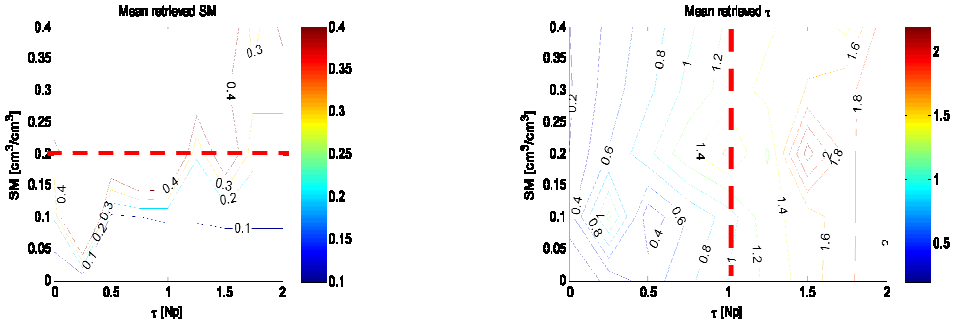

Fig. 4-18: SM and VWC retrieval under non-ideal conditions (ΔT_B=0 K), ΔT_{ph}=0 K, ω= ω_{ref}=0.1 and hr = 0 -h_{ref} =0.1. (a) SM retrieval mean (b) VWC retrieval mean.

Fig. 4-18 shows another non-ideal case, the simulation parameters are ideal radiometer (ΔT_B=0 K), the albedo is constant (ω_{ref}=0.1), the soil roughness is constant (h_{ref} =0.1) as well and the topology is flat and it does not changes in the whole flight range, and soil temperature that has no variations (ΔT_{ph}=0 K). The retrieval parameters are the same used in the simulation except for the surface roughness that has been assumed as 0 (h_s=0). As expected the retrieval does not have important errors. In Fig. 4-18a, the retrieved algorithm estimates SM quite well. In Fig. 4-18b the retrieval is quite good any value of SM and τ.

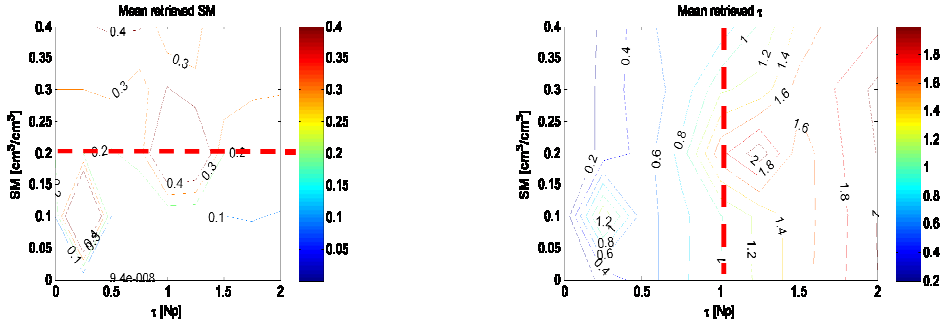

Fig. 4-19: SM and VWC retrieval under non-ideal conditions (ΔT_B=0 K), ΔT_{ph}=2 K, ω= ω_{ref}=0.1 and hr =h_{ref} =0.1. (a) SM retrieval mean, (b) VWC retrieval mean.

Fig. 4-19 shows another non-ideal case, the simulation parameters are ideal radiometer (ΔT_B=0 K), the albedo is constant (ω_{ref}=0.1), the soil roughness is constant (h_{ref} =0.1) as well and the topography is flat and it does not change in the whole flight range, but not the soil temperature that has a variation of 2 K (ΔT_{ph}=2 K). The retrieval parameters are the same used

in the simulation except for the surface roughness that has been assumed as 0 (h_s=0). As expected the retrieval has important errors. In Fig 4-19a, the retrieved algorithm estimates SM wrongly. In Fig 4-19b the retrieval is quite good any value of SM and τ.

As a conclusion of this section it is important to highlight that the radiometer has to have a good performance $\Delta T \leq 0.1$ K (long integration time due to large footprint), good estimations of ω and hr are required (vegetation type and soil surface parameters) and the soil temperature changes within the flight are has to be low $\Delta T_{ph} \leq 2ºC$, then it has not a critical impact on the retrieval. As expected, the best performance is for bare soils, but reasonably good for wet vegetation-covered soils as well.

4.5 ARIEL processor graphical user interface

This section is devoted to the graphical user interface (GUI) that implements all the algorithms described in previous sections (Fig. 4-20). As stated in the introduction the main objective of this GUI is to provide an easy tool to a non-expert user, so that it has to be easy and intuitive. Although it was considered to include more options in the GUI, they were discarded focusing on the most important ones to avoid mistakes.

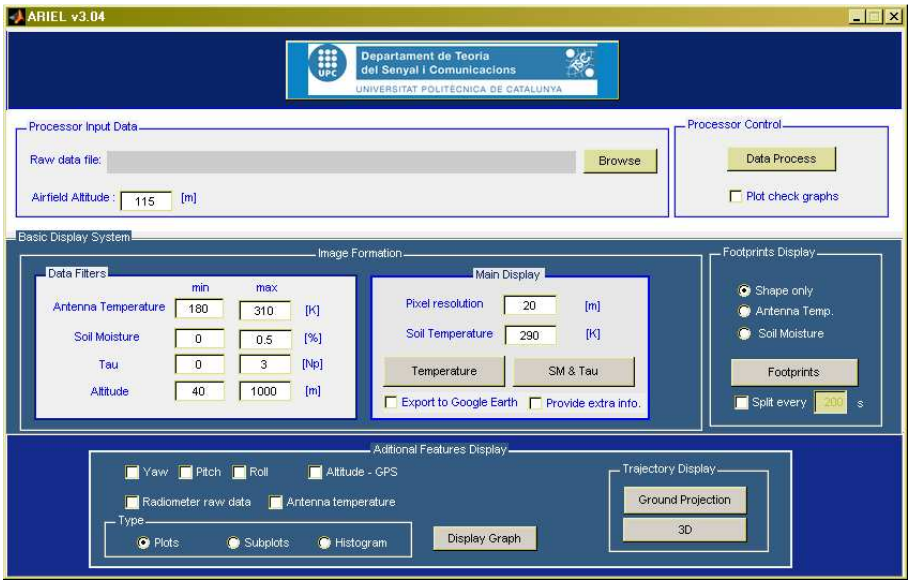

Fig. 4-20: ARIEL processor graphical user interface.

Figure 4-20 shows the main panel of the ARIEL processor GUI, at the top there is the "Processor Input Data" box from where the raw file to be processed is selected, this file contains all the attitude and radiometric information (section 3.5.3). When pushing the "Browse" button a system browser window pops up (Fig. 4-21), from where is possible to select the desired file.

Another important input data, which is placed in the same text box, is the "Airfield Altitude" which will be subtracted to the sensors provided altitude to correct the pixel size. This is done because the GPS altitude takes as reference the World Geodetic System (WGS-84), not the ground level.

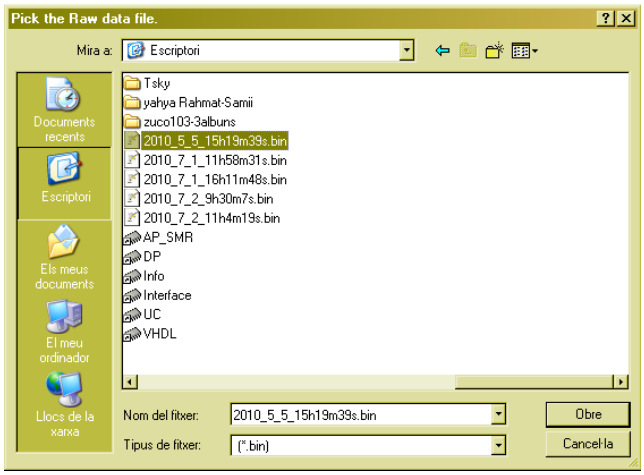

Fig. 4-21: Raw data file pop up window

Once the raw data file has been selected, the top right "Processor Control" text box contains the "Data Process" button which starts all the procedure. Pressing down this button the processor reads the raw input file and splits the attitude and radiometric data. Furthermore, the system calibrates the radiometric data as explained in previous sections, first looking for a water mass measurement and if not possible, then using the laboratory calibration coefficients. In order to help the user, as many information as possible is displayed. So that if was not possible to found the water mass measurement a pop up window is displayed giving a warning information for the user knowledge (Fig. 4-22).

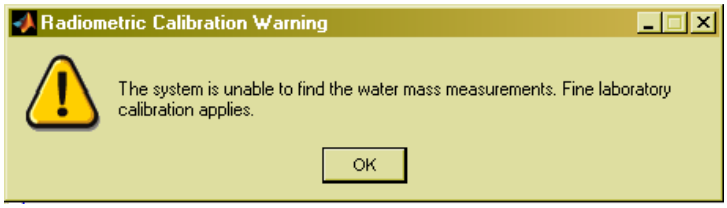

Fig. 4-22: Pop up window warning that it was not possible to find water mass measurements

In any case, at the end of this procedure if the calibration has been performed successfully another pop up window appears providing this information for the user confidence on the procedure (Fig. 4-23). If it is not successfully finished, the same pop up window provides information of the error and suggestions to debug the problem.

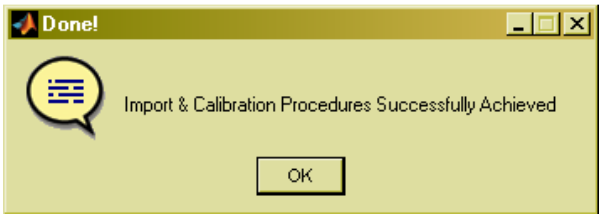

Fig. 4-23: End of the import and radiometric calibration information pop up window

In the same text box there is a check button called “plot check graphs”. If selected, the system displays three plots which are crucial and it will easy to find a problem on the raw data file just glimpsing these plots. The first one shows the raw radiometric output for both polarizations, the second shows the antenna temperature, the calibrated radiometric raw data, for both polarizations, the third one shows the aircraft attitude and finally, the fourth one, shows the aircraft altitude.

Below the top text box there is the “Basic Display System” which contains at the same time two text boxes, the first one is labeled “Image Formation” and the second is labeled “Footprints Display”. The “Image Formation” text box contains all the options to create SM and VWC images. This box has a part labeled “Data Filters”, which contains four different filters, brightness temperature, soil moisture, τ (vegetation opacity) and aircraft altitude. These filters are very useful and have lots of possibilities, for example, to filer radiofrequency interferences

(by selecting the maximum brightness temperature as 300 K) or to select only the driest regions of the image (by selecting a low maximum soil moisture value) or it is even possible to select some footprint size selecting a suitable altitude interval, which can be useful in downscaling algorithms. The default values are displayed in Fig. 4-20, and are the expected ones when flying over a regular zone. There is still another filter defined implicitly without any tuning options in the GUI that is the attitude filter. By default all the footprints with any of the attitude angles larger than 10^{o} are discarded to ensure the second assumption in section 4.4.1. These "Data Filters" information are collected by the "Main Display" text box where Brightness temperature images (by pushing down the "Temperature" button) or SM and VWC images (by pushing down the "SM&Tau" button) are created. Images are created using the merging and interpolation techniques described in a previous section. Furthermore if the displayed image provides the soil moisture and vegetation opacity information, the retrieval algorithms described in previous sections are here applied.

The image creation procedure needs 5 inputs, the filtered data information, the pixel size of the resulting image, the soil temperature (which it has to be assumed as homogeneous in the whole flight region), the "Google Earth export" check button and the "Provide extra info." Check button. Checking the "Google Earth export" the processor creates an image with a transparent background and it is being directly exported to the Google Earth for a better understanding and interpretation of the results. Checking the "Provide extra info." the processor shows information of the confidence of each pixel, showing how many footprints has contributed to the pixel formation. The procedure provides information about the image dimensions and the image resolution achieved by pop up a new information window (Fig. 4-24).

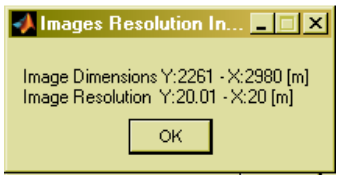

Fig. 4-24: Image dimensions and resolution pop up window

As previously stated the system can work with one or two polarizations, of course the retrieval is better in the case of two polarizations, but still in the case of having just one of them the system can provide some retrieval information about SM and VWC. If only one polarization is found the system gives a warning to the user that the retrieval has been performed using only the nadir beam (Fig. 4-25). It also provides suggested action in case that is an error for debugging, i.e. there are both polarizations, but only one is detected.

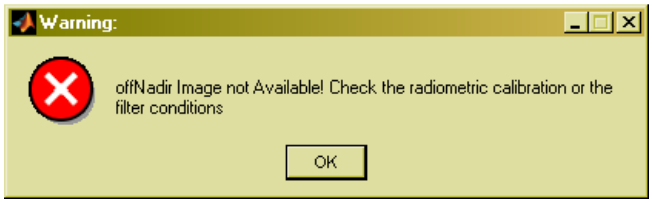

Fig. 4-25: Only one polarization found pop up window

The other part of this test box is the “Footprint Display”, in this case pushing down the “Footprints” button, the footprints are displayed without merging or interpolation. These footprints can be empty or filled with the antenna temperature or SM, depending on which radiobutton is selected. Furthermore, there is a check button labeled “Split every” that splits the flight in blocks equal to the number of seconds defined in the associated test box, creating as many figures as necessary.

At the bottom of the GUI, there is the text box labeled “Additional Features Display”, which, by pressing the “Display Graph” button, displays any of the selected radiobutton flight information in different ways, in subplots, plots or in histograms as selected by the radiobuttons in the “Type” label. The histogram plot feature is very useful because it allows to the user to analyze the data from a statistical point of view, identifying if the image has water mass, radiofrequency interferences or any other anomalies. The quality of the retrieval can be significantly improved by analyzing previously in a statistical way the signal, and using the inferred information in the “Data Filter” text box. The subplot and plot features are also very useful because allow the user to plot more than one flight information parameter in the same plot to detect any correlation or contrast the robustness of the measurements. In this text box

there is still another box labeled as “Trajectory Display” which simply displays the aircraft trajectory with no more information, it can be plotted in 2D (“Ground Projection” button), without altitude information, or in 3D (“3D” button), including the altitude information.

4.6 Conclusions

In this chapter the ARIEL processor has been presented. The whole retrieval algorithm, which is composed by different algorithm parts: calibration, footprint projection, merging and interpolation, and finally the SM and VWC retrieval has been deeply analyzed. The retrieval algorithm is an ill-posed problem which requires eight input parameters and the system has only two independent measurements, so that three assumptions are required: the geophysical, the polarimetric and the radiation assumptions have been described and analyzed how to avoid them has been analyzed or which are their range of validity. It has been found that the radiometer has to have a good performance $\Delta T \leq 0.1$ K, good estimations of ω and h_r are required and the soil temperature changes within the flight have to be lower than $\Delta T_{ph} \leq 2^{o}C$, then it has not a critical impact on the retrieval. As expected, the best performance is for bare soils, but reasonably good for wet vegetation-covered soils as well.

Finally, the ARIEL processor GUI has been presented with a brief user manual indicating where each algorithm applies.

5 Experimental results

After presenting the ARIEL controller and processor, they should be tested. Due to the complexity of the validation, where lots of variables are involved, this has been spitted in two different and complementary tests.

The first test consists of a flying test that has been done in the Ripollet aerodrome (close to Barcelona) to analyze the controller and processor performance without taking into account the radiometric values. On the other hand, the second test consisted of testing the retrieval algorithm without taking into account the flight information. In order to carry out the second tes, a ground based field campaign was conducted in Palau d'Anglesola (Lleida) where several measurements were performed over different types of soil and vegetation layers.

5.1 Controller and Processor software test

The first test took place the May 5th of 2010 in Ripollet (Barcelona), within a controlled environment. The coordinates of the experiment were in latitude 41^{o} 30' 14.91" North and in longitude 2^{o} 57' 57.13" East (Fig. 5-1).

Fig. 5-1: Ripollet experiment site. The radio control aerodrome and adjacent fields.

As described in the introduction, a long history behind the ARIEL radiometer exist and although this was not the first flight of the ARIEL concept, it was the first flight test of a new and improved design. So that, as it needed to be tested as it was the first time, the aircraft was prepared to only carry a one polarization radiometer (v polarization nadir beam) to test the system capabilities avoiding overloading the system.

Figure 5.2 a shows the ARIEL controller software, on the left it shows the controller working and acquiring samples. The indicative color box is green, which means that the system is acquiring normally, the radiometer and the MTi-G have been found in the serials ports COM1 and COM3, respectively. There is a red warning indicating that the MTi-G does not have yet available GPS data, this happens in the first moments of the acquisition when starting the GPS from a cold initialization. Furthermore, some raw data from the radiometer and form the attitude system is displayed in text boxes.

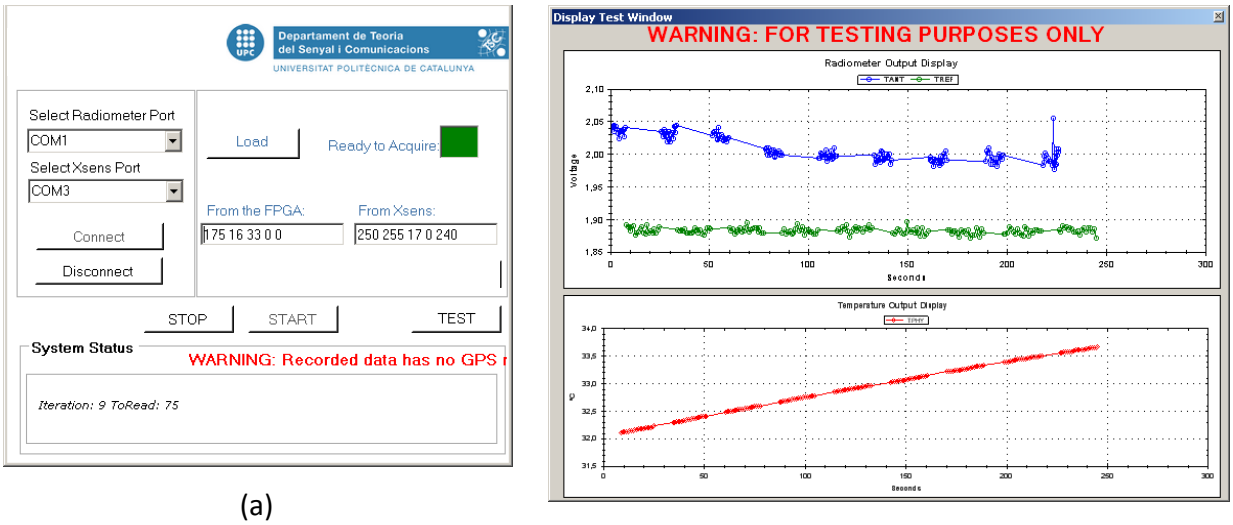

(a) (b)

Fig. 5-2: Verifying the controller software. (a) ARIEL controller acquiring data, (b) display test window for testing purposes only.

Figure 5.2 b shows the test window mode, when the acquired data is real time displayed. The blue dotted line is the antenna brightness, which fluctuates significantly because is measuring random antenna inputs, the green dotted line is the internal reference (a matched

load), which is stable, and the red line is the physical temperature. It is obvious that the system is not yet stabilized in temperature, so that the physical temperature is increasing finding the stabilization value (40^{o} C). This test mode is useful to check that everything is as expected and to determine when the system is ready for acquisition, i.e. when the thermal temperature is stable. As mentioned in chapter 3, when the system is ready to start to flight, this window has to be close, otherwise the sampling rate decreases dramatically.

After some avionic and radiometric preparation the flight test was conducted satisfactorily and, once finished, the output file was ready to process. Despite the Ripollet zone was since that day a pretty clean radiofrequency interference area, that time some interferences were detected specially when calibrating the cold reference using the sky, pointing to the North to measure the background cosmic radiation (≈6 K at L-Band). Furthermore, as it was the first time that the whole system was tested under real conditions some internal interference was found. These interferences come from the onboard computer, specifically from the communication cables, since then some actions have been taken to neglect these interferences. In this first test, interferences totally masked the radiometric information but not the functional system test, which was the aim of this first test. So that, in this section results are not analyzed from a radiometric point of view, which is done in the next section. They are analyzed considering only the controller and processor software.

Figures 5-3 show the radiometric results of the flight test, as it can be observed there is only the v polarization (red-dotted) was measured, the h polarization (black-dotted) is zero. At the beginning of the acquisition there is a stable zone, which corresponds to the hot load calibration (microwave absorber), then there is a valley, which corresponds to the cold load. In Fig. 5-3a the raw data is presented, antenna temperature and internal reference values are intercalated. Furthermore, there is too much fluctuation of output values. In Fig. 5-3b the calibrated data is presented and the internal reference values have been removed remaining only the antenna temperature. The mean value during the flight is slightly over the 600 K, which makes no sense at all taking into account that the soil temperature is around 300 K, then it is

easy to infer that the radiometric data is interfered by something, as stated before some self system interference.

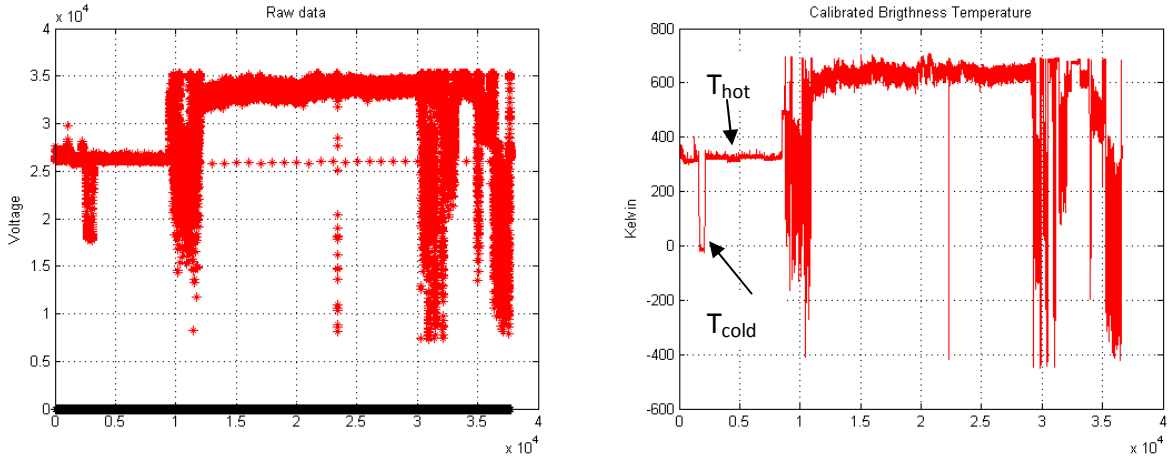

(a) **(b)**

Fig. 5-3: First flight results analysis. (a) raw voltage data from the radiometer, (b) calibrated output

Using the "Advanced Features Display" box of the ARIEL processor (chapter 4), the altitude information of the flight is displayed in Fig. 5-4.

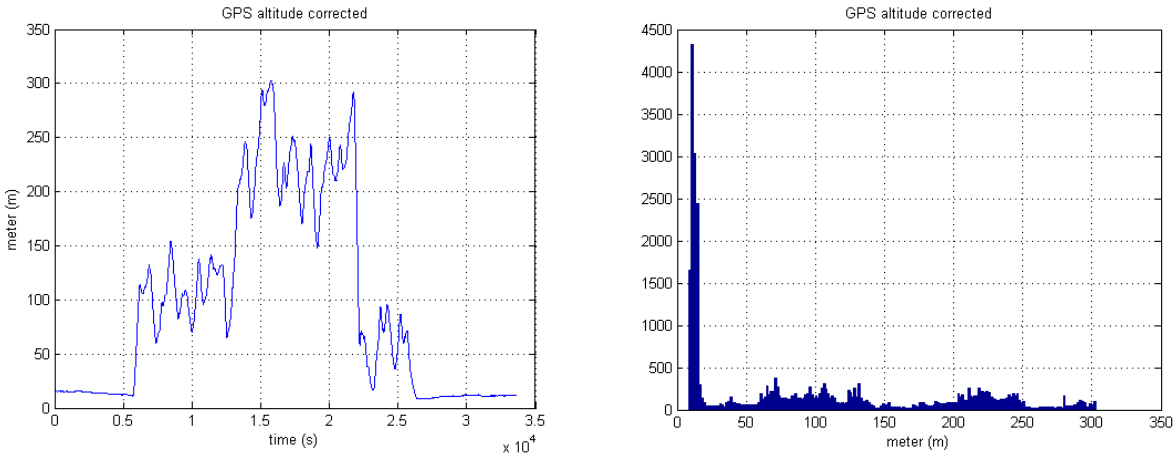

Fig. 5-4: Flight altitude from the MTi-G GPS data (a) time plotted (b) histogram

As it can be observed, the flight height goes from 50 m to 300 m. The flight is not stable in altitude, which generates a wide range of different size footprints. In both plots can be observed when the system is on the aircraft field, in Fig. 5-4a shows the exact times when the

aircraft takes off and when it lands. The histogram provides statistical info for apply the height filter knowing acquisition properties.

Keep on using the "Advanced Features Display" box of the processor, the antenna temperature histogram is displayed (Fig. 5-5). The plot shows again clearly that the system has an interference problem, there is a peak in 300 K, which is the expected value when measuring soil, and there is another peak at 700 K which indicates a saturation in the system (is not symmetric). Furthermore, there are values under the 0 K, which is physically impossible, and it is another indication to infer that the system is not working properly.

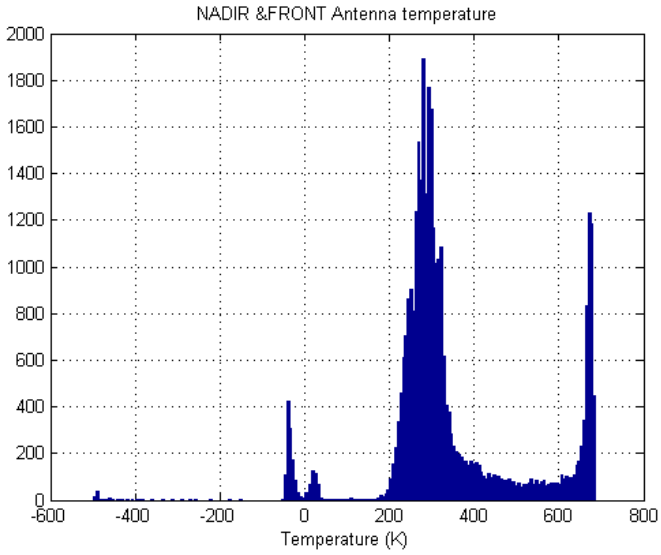

Fig. 5-5: Statistical analysis of the antenna temperature

Another feature in the "Advanced Features Display" box is to plot the three attitude angles of the plane. Figure 5-6 shows this information. As it can be observed in Fig. 5-6 the three angles are not stable as expected in a field measurement experiment. Information that can be inferred from this plot is that it is just a test flight with no intention of having stabilized measurements in pitch and roll angles. At the beginning of the acquisition and especially in the roll angle there is a high rotation corresponding to the T_{sky} calibration.

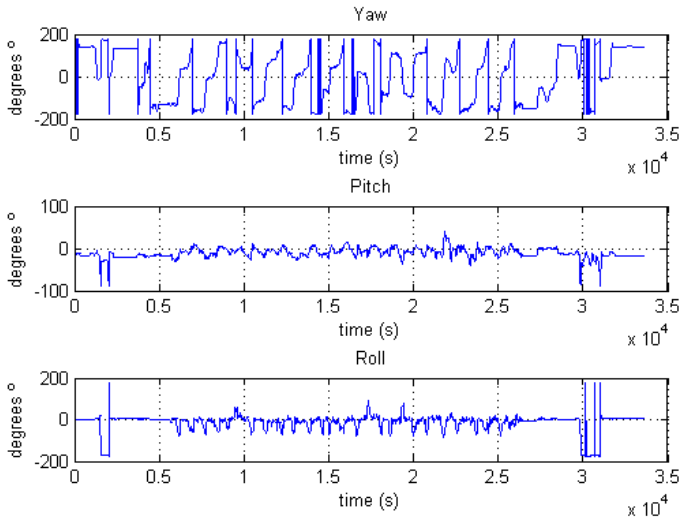

Fig. 5-6: Attitude of the aircraft obtained during the test flight using the MTi-G

Another yet application of the Using the "Advanced Features Display" box is the display trajectory, that can be projected in the ground (Fig. 5-7a) or displayed as a 3 dimensional plot (Fig. 5.7b). In both plots it is clear the aim of the pilot, to totally cover by over passing and as much as possible the observed area.

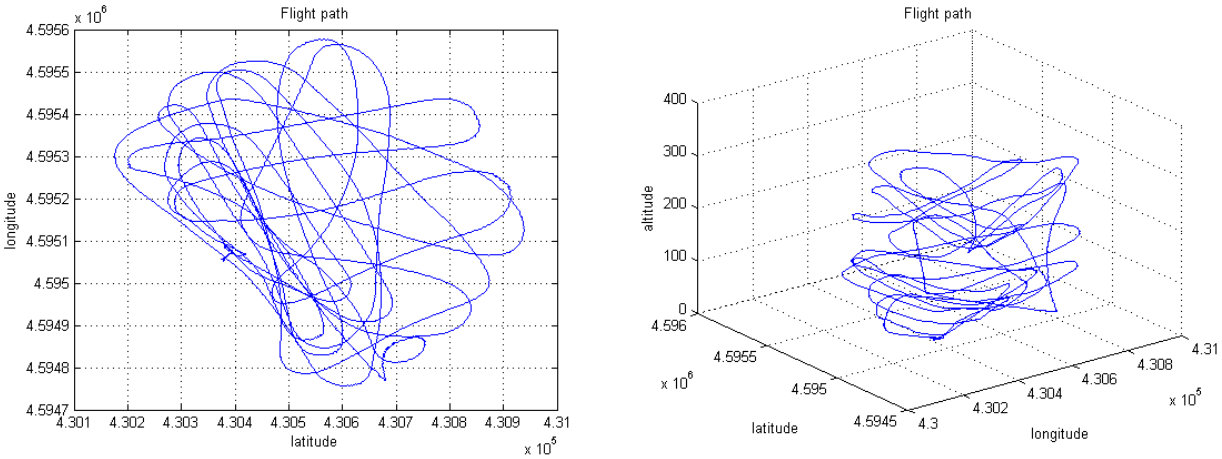

(a) (b)

Fig. 5-7: Trajectory of the flight. (a) ground projection, (b) a 3 dimensional representation.

Fig. 5-8 shows the merged brightness temperature. The plot has the latitude and longitude coordinates and a colour code which indicates the value of each pixel. The pixel resolution is 20x20 meters.

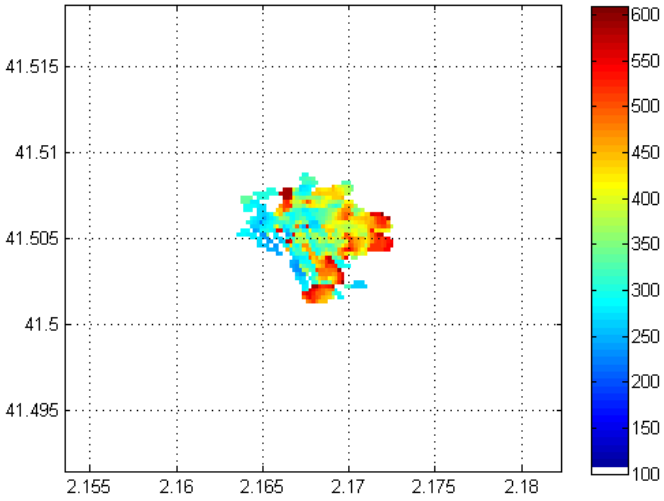

Fig. 5-8: Merged antenna temperature map, with a pixel resolution of 20x20 meters.

Although the pilot intention was to cover all the area by over passing, there are some empty spaces due to the attitude angle filter. This image has been created by merging different footprints with different weights as previously explained in chapter 4.

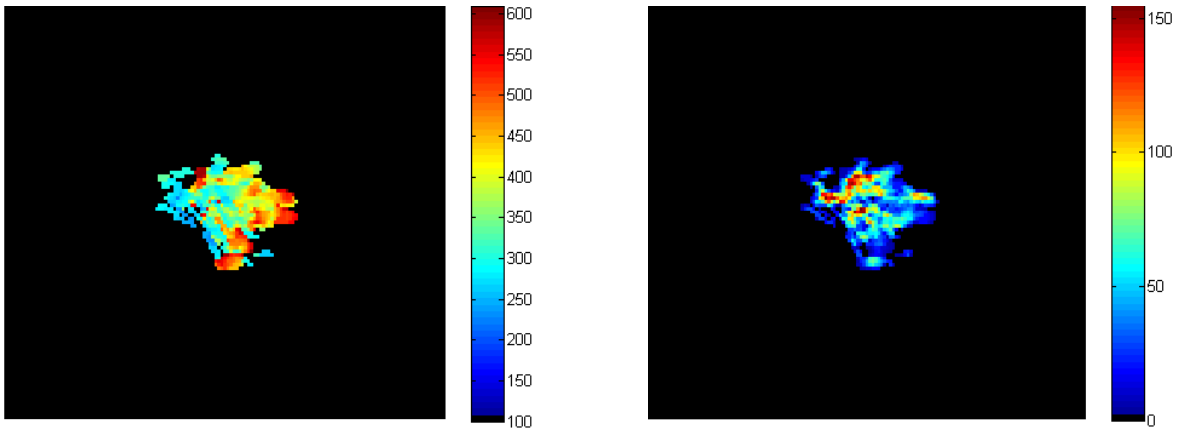

(a) **(b)**

Fig. 5-9: Antenna temperature map. (a) merged data, (b) number of used footprints for calculating the value of each pixel.

A very useful option is to display the merged images in the Google Earth to geolocate the measurement and correlate the map information with the resulting image. The previous step is to plot the images on a black background (Fig. 5-9), to easily convert the black colour to a transparent one in the .png format.

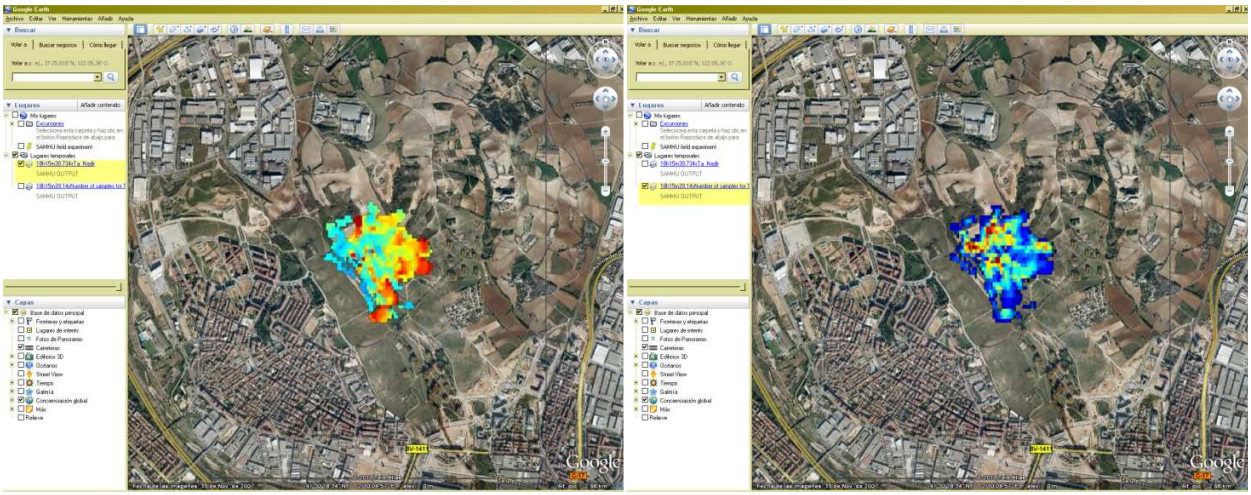

(a) (b)

Fig. 5-10: Antenna temperature map over Google Earth, for geolocated analysis (a) merged data (b) number of used footprints for calculating the value of each pixel.

Once the image has been computed and the black background converted to transparent the ARIEL processor automatically opens the Google Earth software (if installed) and geolocates the obtained images as shown in Fig. 5-10.

Another thing to test the functionality was the pixel resolution, which is a trade off between computational time and image quality. Obviously there is a limit on the information added when the pixel resolution decreases and this is determined by the number of footprints that contributes to each pixel, as explained in chapter 3. Figure 5-11 shows an example of the pixel resolution. Both pictures have been generated using the same raw data file, the only difference between them is the pixel resolution (20x20 and 100x100 meters). It can be observed that the main values of each part are the same but the higher resolution image provides more information.

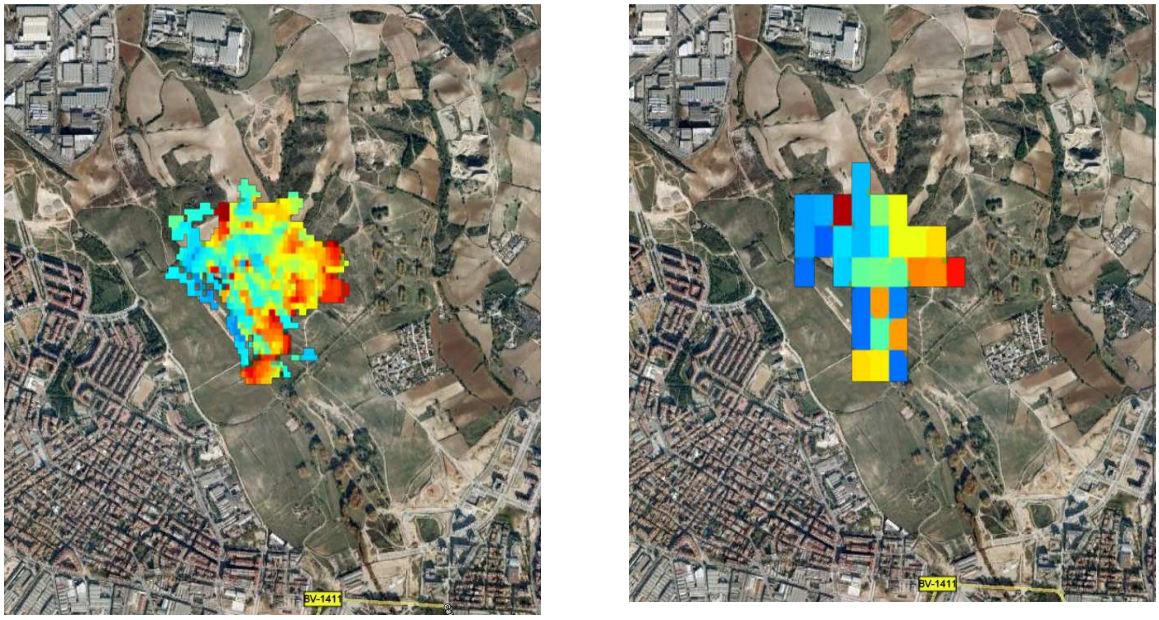

(a) (b)

Fig. 5-11: Antenna temperature merging images. (a) 20x20 meters resolution (b) 100x100 meters resolution.

This section ends without a retrieval algorithms analysis because the collected radiometric data has too much interferences and a special test campaign was conducted to test the algorithm, which is reported in the following section.

5.2 Radiometric retrieval test

This second test took place the June 29th of 2010 in Palau d'Anglesola (Lleida), within an intensive agricultural environment. The coordinates of the experiment site were latitude 41^{o} 38' 16.33" North, and longitude 0^{o} 50' 53.03" East (Fig. 5-20 a b). In order to have different contrast during the experiment, three different fields were used, one with a huge vegetation layer (maize), another with no vegetation (bare soil) and the last one with a thin layer of vegetation (harvested alfalfa). Furthermore, to increase the variability of the measurements a water tank was provided to irrigate the different fields and change the soil moisture values.

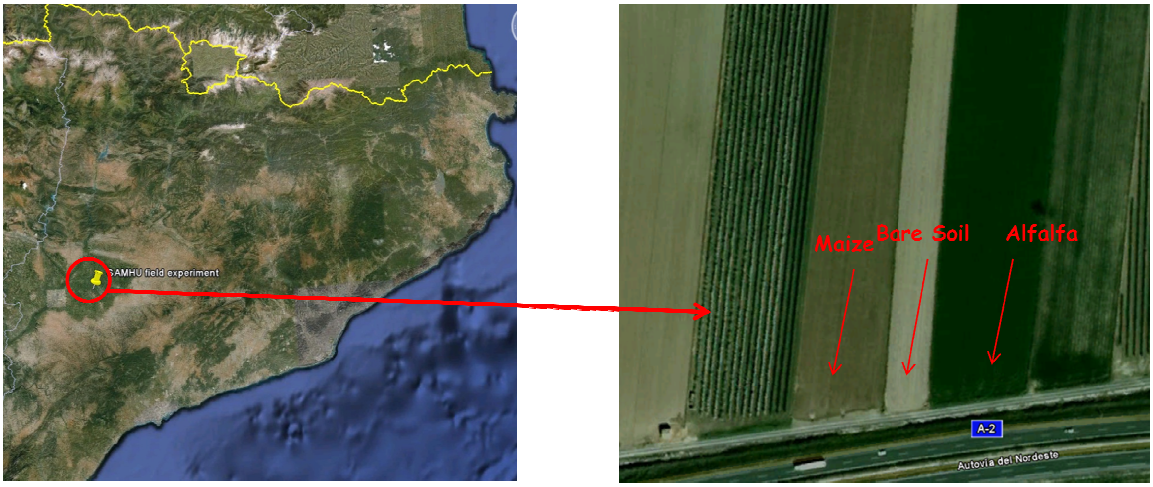

(a) (b)

Fig. 5-20: Palau d'Anglesola experiment site. (a) The test site in the Catalonia context (b) the three agricultural fields used in the experiment with maize, alfalfa and bare soil.

To successfully develop the field experiment, the campaign logistics and scheduling was planned in detail. Therefore, before going to the test site, some calculus and estimations were performed in order to conduct the experiment. First of all, for practical reasons it was decided to measure from 3 meters of height, which satisfies the far field condition of the antenna and provides a nadir footprint of 1.3 meters ($\Delta\theta_{Beam}=25^{o}$) and a fore-looking footprint of 1.5 meters ($\theta_{Beam}=25^{o}$ and $\theta_{incidence}=22^{o}$) centered at 1.1 meters from the nadir center. Another important issue is that the structure to support the ARIEL radiometer could not interfere the radiometric measurements, so that the radiometer should be hold from a certain distance from the main structure as shown in Fig. 5-21

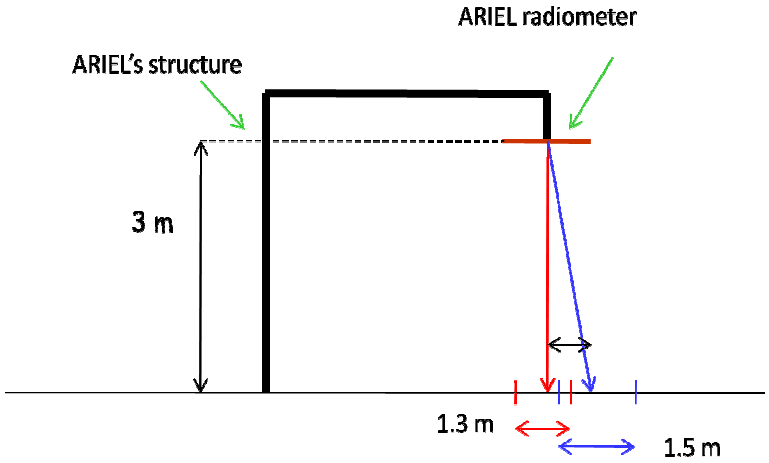

Fig. 5-21: ARIEL's structure and sketch for the Palau d'Anglesola test.

Not only the footprints have to be taken into account, a security margin to ensure the homogeneity of the measured soil had to be considered. Usually this security margin includes another footprint around the central one being measured.

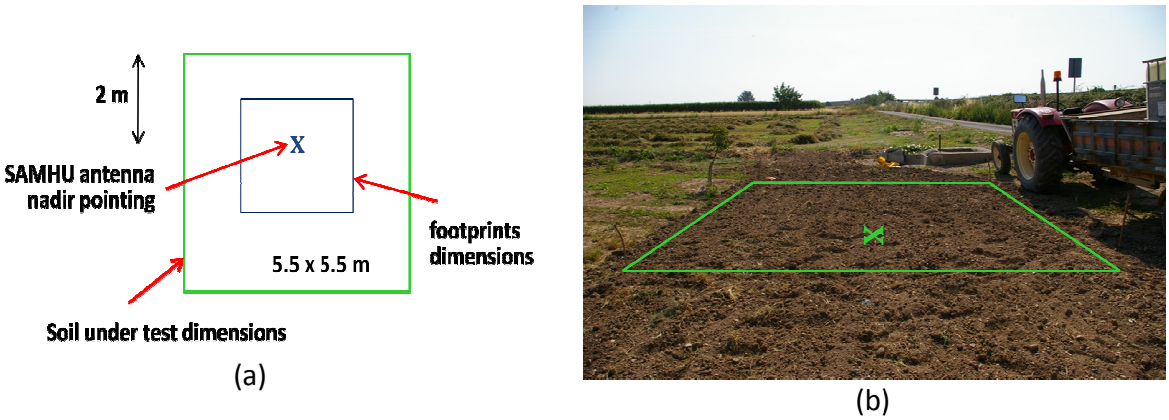

Fig. 5-22: ARIEL footprint (a) theoretical sketch (b) real footprint in the bares soil field

These requirements are fulfilled and sketched of Fig. 5-22a, where the center footprint, where the nadir beam are pointing is 2 meters from the edge of the soil under test dimensions (marked with and 'X'). The total dimensions of the soil under test are a square of 5.5 per 5.5 m. Figure 5-22b shows the real square within the radiometric measurements for bare soil were taken.

After this theoretical analysis, the field campaign was conducted on June the 29th of 2010 at 9 h and finished at 13 h. Some previous preparations were carried out to measure, such as preparing the radiometer (Fig. 5-23a), preparing the radiometer support to a lift through a Mecalux structure (Fig. 5-23b), mounting the antenna and the radiometer to the structure (Fig. 5-23c) and finally checking that the computer software (ARIEL controller) and everything else was ready for the test (Fig. 5-23d). Note that the ARIEL's structure stated in Fig. 5-21 was replaced by a lifter and a tractor which gives more mobility and fulfills the requirements (Fig. 5-23 b).

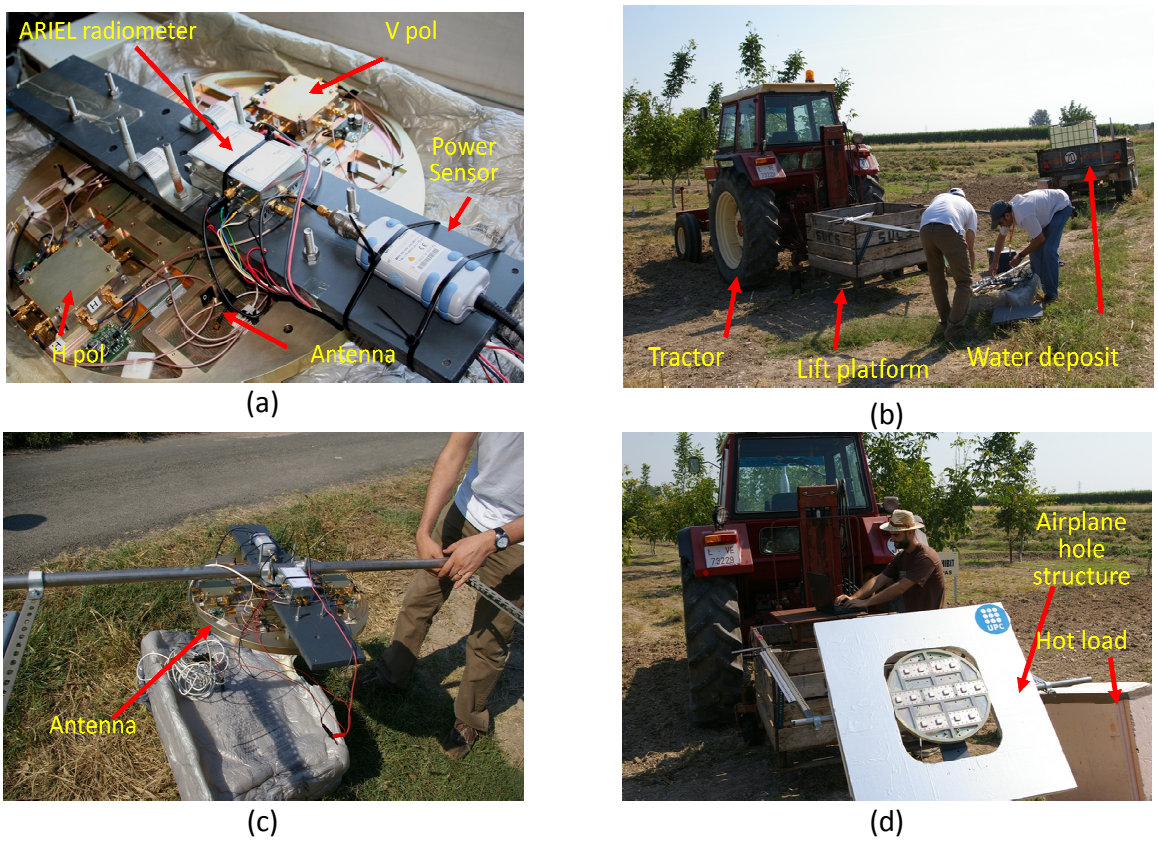

Fig. 5-23: Palau measurements preparations (a) radiometer overview, (b) the system lifter (a tractor with a lifter) with a Mecalux structure to attach the radiometer, (c) antenna and radiometer hitch up, and (d) verifying the readiness of the whole system by checking the controller software .

In order to be able to compare the retrieved values with the real values, which will determine the goodness of the retrieval algorithms, it was mandatory to deploy in situ measurement instruments on the three different soils under test. To get this ground truth

measurements several instruments were used such as a Decagon soil moisture probe [14] buried at 5 cm (Fig. 5-24a). Figure 5-24b shows the measurement of one of these probes in dry bare soil, a multimeter and batteries were required for this measurement. Figure 5-24c shows another soil moisture probe in the maize field and a GPS receiver used to exactly identify in a map each ground truth measurement. As it has been stated in the previous chapter, another important measurement is the soil temperature. To measure this variable a mercury thermometer was used (Fig. 5-24d).

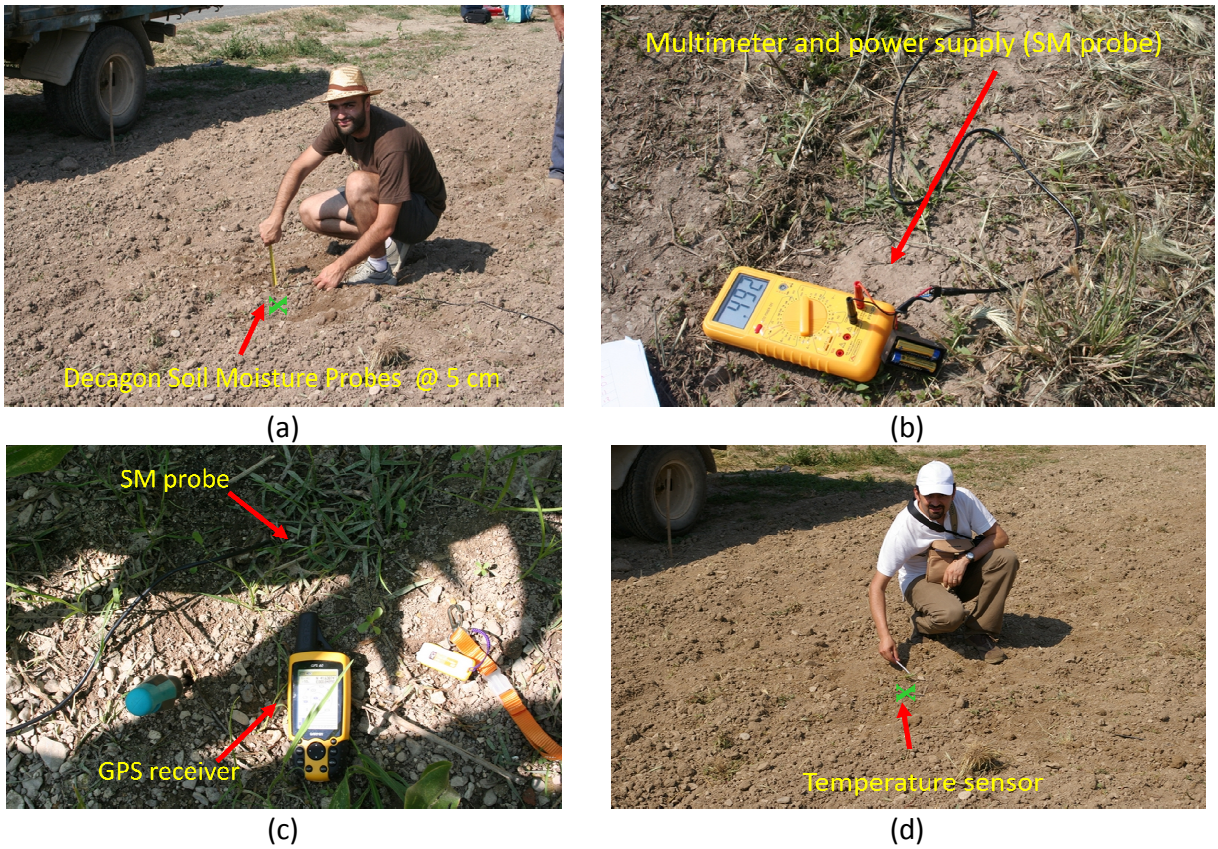

Fig. 5-24: Instruments for measuring the ground truth deployment (a) installing a soil moisture probe in a dry bare soil, note that the 'x' shows were the nadir antenna will point, (b) measurement of soil moisture over bare soil, (c) deploying the probes over the maize field and (d) installing a thermometer in the nadir antenna pointing area.

After preparing the ARIEL antenna and radiometer, and deploying the ground truth instruments, the campaign was ready to start. As shown in Fig. 5-25a, the measurements started with the bare soil. First, a measurement was carried out as the soil was dry (SM=18%). Then the soil was irrigated using water specially prepared for this purpose, and a second

measurement took place (SM=29%). In this second measurement (Fig. 5-25b), the soil had not time enough to filter all the water and some puddles appeared. And finally, the soil was irrigated again (Fig. 5-25c) and measured again (SM= 35%).

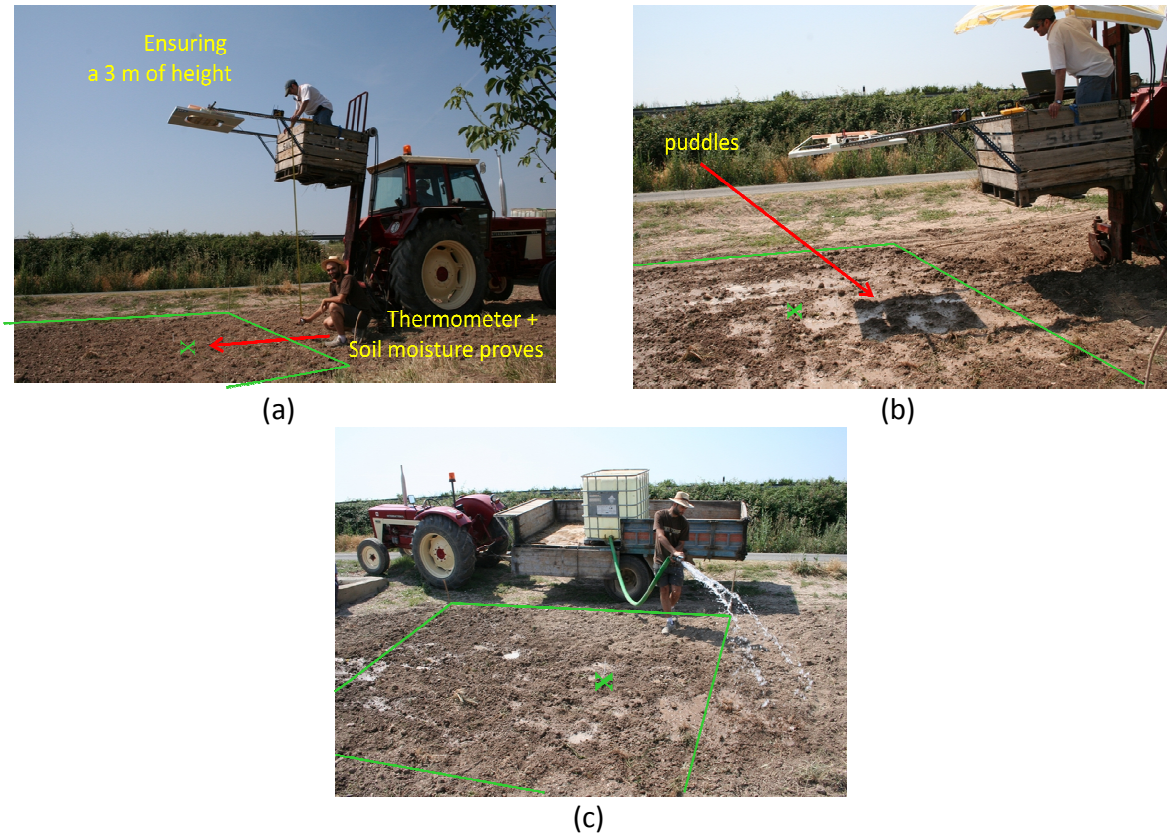

Fig. 5-25: Bare soil measurements (a) preparing the measurement over dry bare soil, (b) preparing the measurement over wet bare soil, and (c) irrigating for second time to prepare the third measurement, soil really wet.

After the bare soil experiment it was the turn of a thin vegetation layer soil measurement. For that an alfalfa field was selected. The measurements were carried out as the soil was (SM=14%). In this case was impossible to irrigate the field because the owner had harvested the alfalfa in the previous days and irrigating it could cause economical damages to the owner. Despite of that a measurement was done to have some representative data of a thin vegetation layer. Figure 5-26a shows the preparations for the alfalfa measurements, and Fig.5-26b shows the alfalfa soil which was drier and more compact than in the case of the bare soil.

(a)

(b)

Fig. 5-26: Alfalfa measurement (a) preparing the measurement, and (b) overview of the alfalfa soil.

The last experiment conducted was over a maize soil. In this case the vegetation layer was really dense (Fig. 5-27a) (16 plants/m^2 with a measured VWC of 4.5 Kg/m^2). First of all a measurement as the soil was at the beginning of the experiment was performed (SM=25%, Fig. 5-27b). Then the field was irrigated by flooding (Fig. 5-27c) and a second measurement was done (SM=50%, Fig. 5-27d). In this case the soil was not able to absorb all the water and by the time of the second measurement the soil as still flood, it was some water over the soil.

(a)

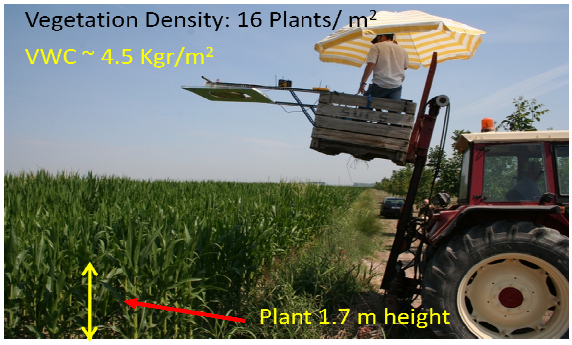

(b)

(c)

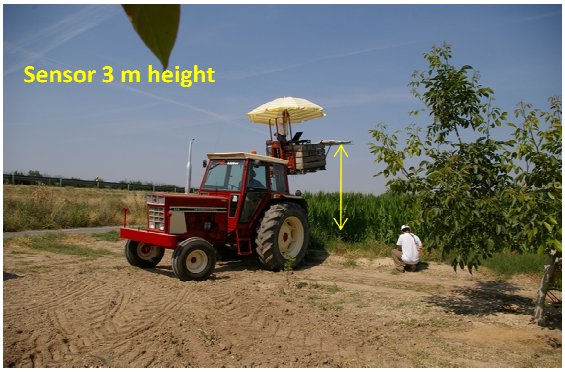

(d)

Fig. 5-27: Maize measurement (a) vegetation layer overview, this picture offers a good view of the mecalux structure, (b) preparing the first measurement, (c) irrigating the maize field by flooding, and (d) preparing the second measurement over the maize field.

The T_{hot}-T_{cold} radiometric calibration was performed before and after each measurement to be able to convert the radiometric raw output to antenna brightness temperature. For the T_{hot}, a microwave absorber was used (300 K) and for the T_{cold} the radiometer was pointed to the North sky (≈6 K at L-Band). Figure 5-28a shows one of these calibrations: the T_{hot}-T_{cold} measurements for both polarizations, using with 1 second of integration time during 300 seconds.

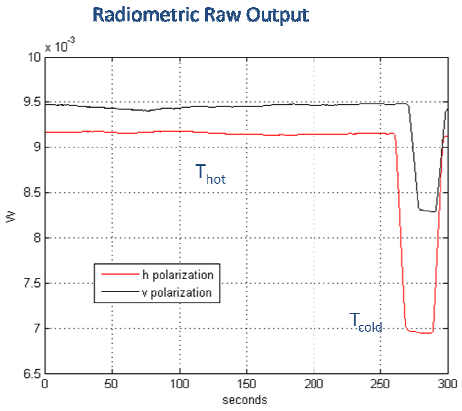

(a)

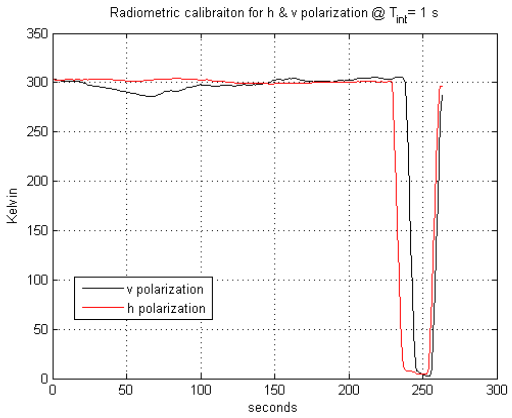

(b)

Fig. 5-28: ARIEL radiometric calibration (a) radiometric raw output (b) antenna brightness temperature from the radiometric raw output.

As it can be inferred the v polarization has less dynamic range than the h polarization which it means that the measurement will be noisier. Figure 5-28 b shows the radiometric data calibrated. As expected the hot load has a value of 300 K and the cold load is 6 K. Furthermore,

from these plots it is possible to calculate the radiometric resolution by computing the standard deviation of the radiometer response when measuring the hot load. The computed radiometric sensitivity for the h polarization is 0.53 K and for the v polarization is 0.96 K for 1 s. of integration time.

Table 5-1 shows the antenna brightness temperatures and the ground truth values of the field experiments. At first glimpse, results are coherent accordingly with the theory. As expected, there is a correlation between soil moisture and brightness temperature. For example for bare soil as the soil moisture increases the brightness temperature decreases clearly.

In the bare wet+ surface type, the brightness temperature has decreased too much with respect the soil moisture increase this is due to the puddles that were in the soil under measurement. Hence, this measure cannot be used as a candidate for testing the retrieval algorithm. For the other two bare soil measurements, the ratio between soil moisture and brightness temperature is 4.84 K/% for the v polarization and 5.67 K/% for h polarization. This it means that the ARIEL radiometer is capable to distinguish variations on the soil moisture of 0.11% for v polarization and 0.17% for h polarization, which is a pretty good accuracy.

Table 5-1.Field experiments measurements summarized

Surface Type	TA_v [k]	TA_h [k]	T_{soil} [^oC]	Soil Moisture
Bare Dry	270.5	270.4	25	18%
Bare wet	226.9	219.3	26	29%
Bare wet+	137.7	179.1	27	35%
Alfalfa	273.5	273.3	25	14%
Maize	290.8	293.3	25	25%
Maize flooded	251.2	243.4	27	53%

Another remarkable issue is that the maize surface type has a high brightness temperature despite of the soil moisture is high. There is 60 K of difference between maize and

bare wet soil surface types, having similar soil moisture values. This is due the high density vegetation layer that masks the soil emission. As expected, the radiometer is not able to see well through dense vegetation layers. Despite of that, when the maize is flooded, the radiometer detects a high variation, this is due to the low brightness temperature of the water. On the other hand the alfalfa surface type has a coherent brightness temperature, which means that the radiometer gets radiation from the soil through thin vegetation layers.

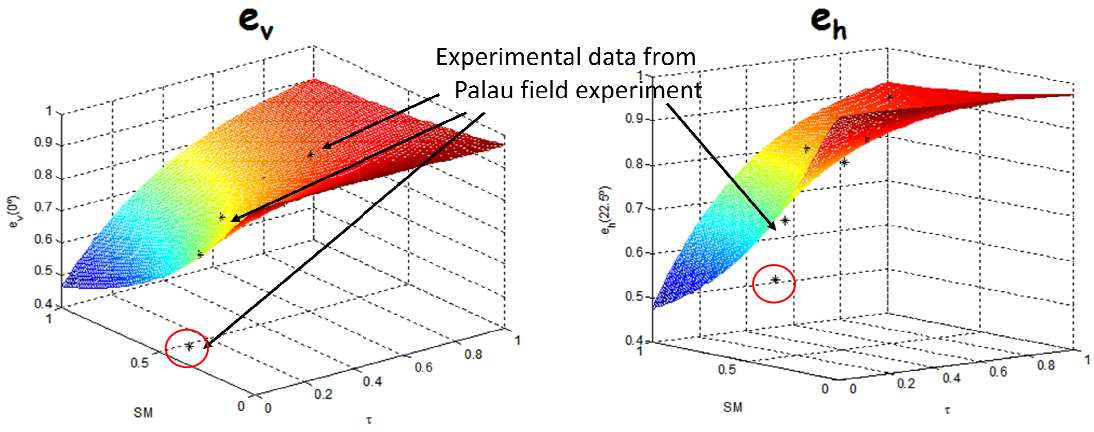

(a) **(b)**

Fig. 5-29: Analysis of the retrieval method. Theoretical emissivity vs measured emissivity (a) evaluation for vertical polarization and 0^0 incidence angle, and (b) evaluation for horizontal polarization and 22^0 incidence angle.

For a first performance analysis of the retrieval, the vertical and horizontal emissivity matrix, which have been obtained by swapping the soil moisture and vegetation water content (Section 4.4.3), have been used. The field campaign emissivity values have been displayed in the same plot of the theoretical emissivity, the measured ground truth has been used as the SM and VWC coordinates of each measured point. Figure 5-29 shows the theoretical emissivity (the surface) and the measured points for both polarizations, as it can be observed there is a great agreement between the theoretical surface and the measured points, except for one point (red-circled), which corresponds to the wet bare soil with puddles measurement.

As explained in chapter 4, the retrieval algorithm consists of minimizing a cost function (Eqn. 5.1). Three different variations of this equation have been considered to tune the retrieval algorithm and get better results. Note that Eqn. 5.1 is the Eqn. 4.33, but it is written here again for a better comprehension of the text.

$$\chi = \alpha \left[\left(e_v - e_{v,model} \right)^2 \right]_{\theta=0} + \beta \left[\left(e_h - e_{h,model} \right)^2 \right]_{\theta=22} \quad (5.1)$$

The first variation, so called Model1, takes into account only the vertical polarization (α= 1 and β=0). The second one, Model 2, uses only the horizontal polarization for the retrieval (α= 0 and β=1). And finally, Model 3 uses both polarizations for the retrieval (α= 1 and β=1). Results are presented in Table 5.2.

Table 5-2. Retrieved values summarized. Highlighted in red the best results.

Surface Type	Model 1		Model 2		Model 3		Retrieved VWC	Ground truth SM
	SM	τ	SM	T	SM	T	VWC=τ/b (b=0.14)	
Bare Dry	0.98	1.04	0.87	0.85	0.1	0.01	133 g/m^2	0.18
Bare wet	0.91	0.40	0.60	0.19	0.29	0.01	67 g/m^2	0.29
Bare wet+	1.00	0.00	0.70	0.04	0.97	0.00	0 g/m^2	0.35
Alfalfa	0.80	1.09	0.74	0.88	0.09	0.03	200 g/m^2	0.14
Maize	0.01	0.16	0.02	0.56	0.00	0.65	4.33 kg/m^2	0.25
Maize flooded	0.65	0.55	0.38	0.21	0.18	0.00	0 g/m^2	0.53

As it can be observed in Table 5-2, the best results are obtained when both polarizations are used (model 3). Models 1 and 2 have larger errors in the SM and VWC estimation. The algorithm does not find any coherent value for the bare wet+ surface type, as stated in Fig. 5-29. And, as expected, it cannot estimate the soil moisture value when there is a dense vegetation

layer. Although it is impossible to retrieve the soil moisture, the vegetation water content is well estimated (measured 4.5 Kg/m^2). As it is already know, when there is water in the scene, flooded maize surface type, the algorithm does not work at all.

The soil moisture retrieval for the dry bare soil, wet bare soil and for alfalfa surfaces has some errors but they are on the error range where the measurement is useful and gives information about the surface. In the SMOS the soil moisture target resolution was 4% [CITA], here the system has an error of 8%, 0% and 5% respectively, which are more than acceptable errors. The WVC works reasonably well in all the surfaces, in bare soil should be 0 but is 0.01, which is in practice no vegetation layer.

Despite this two wrong measurements (bare soil with puddles and flooded maize), which was already expected to be wrong because they do not fulfill the hypothesis that there is no water in the scene, the algorithm works reasonably well, taking into account that the instrument had no thermal control system.

5.3 Conclusions

This chapter has focused on the whole system validation. The general validation has been done in two different field campaigns, in the first one (Ripollet) the avionics and ARIEL software were tested, except for the retrieval algorithm. In the second test (Palau d'Anglesola) the goal was to only test the retrieval algorithm without taking into account the flight complexity, this was done on a ground based measurement test.

For the first test, the main conclusion is that both software programs, the controller and the processor, were ready and they fulfill the design specification.

For the retrieval algorithm test the conclusion is that it works reasonably well taking into account that the instrument had no thermal control system.

6 Conclusions and future work lines

6.1 Conclusion

The aim of the present work was to culminate the knowledge acquired in the previous versions of the system into a non-expert user instrument. So that, new sensors were placed in the aircraft and new acquisition and processor software was designed.

Chapter 3 has focused on the onboard instruments needed to create a map from an airborne platform and their synchronous acquisition. Firstly, the MGi-T has been analyzed giving its main features and a glimpse to its working modes and configuration has been provided. Then, the radiometer has been presented giving the features and characteristics, giving an overview over the communication radiometric protocol. On the other hand, the software that controls both instruments has been explained and detailed.

In chapter 4, ARIEL processor has been presented. The whole retrieval algorithm, which is composed by different algorithm parts: calibration, footprint projection, merging and interpolation, and finally the SM and VWC retrieval has been deeply analyzed. The retrieval algorithm is an ill-posed problem which requires eight input parameters and the system has only two independent measurements, so that three assumptions are required: The geophysical, the polarimetric and the radiation assumptions have been described and analyzed to minimize the impact to the measurement or which are their validity range. It has been found that the radiometer has to have a good performance $\Delta T \leq 0.1$ K, good estimations of ω and h_r are required and the soil temperature changes within the flight are has to be lower than $\Delta T_{ph} \leq 2^{o}C$. As expected, the best performance is for bare soils, but reasonably good for wet vegetation-covered soils can be achieved as well. Finally, the ARIEL processor GUI has been presented with a brief user manual indicating where each algorithm applies.

Chapter 5 has devoted on the whole system validation. The general validation has been done in two different field campaigns, in the first one (Ripollet) the avionics and ARIEL software were tested, except for the retrieval algorithm. In the second test (Palau d'Anglesola) the goal was to only test the retrieval algorithm without taking into account the complexity of the flight, this was done on a ground based measurement test.

For the first test, the main conclusion is that both software programs, the controller and the processor, were ready and they fulfill the design specification.

For the retrieval algorithm test the conclusion is that it works reasonably well taking into account that the instrument had no thermal control system.

6.2 Future work lines

At the end of this work, some future work lines have been envisaged to improve the system performance:

1. Self interferences have to be neglected,
2. auxiliary data information from existent data bases should be include into the retrieval algorithms, such as thermal measurements of the soil or using a digital elevation map,
3. multiple and complementary sensors should be joined to the AIREL radiometer to increase the performance of the retrieval algorithm, such as an infrared radiometer to estimate the soil or vegetation temperature or a 36 GHz radar to estimate the vegetation water content from an alternative way, and
4. a flight campaign for testing the retrieval algorithm is required, using a high sampled ground truth measurement for both parameters, SM and VWC.

Bibliography

[1] Bou F., “Disseny i implementació d’un radiòmetre/GNSSR embarcat en avió de control i remot;” advisors: A. Aguasca and X. Bosch. Master Thesis UPC, 2007.

[2] Ibáñez C., “Diseño e implementación de un sistema híbrido GPS - Inerciales para determinar la trayectoria de un avión RC y de unos módulos de comunicación en bandas ICM con la estación base;” advisors: A. Aguasca. Master Thesis UPC, 2007.

[3] Benedicto P., “Emisividad del terreno en banda L: Estudio y medida del efecto de la topografía;” advisors: A. Camps and S. Morrenis. Master Thesis UPC, 2007.

[4] Glénat, M., “Georeferencing in Google Earth radiometric data from UAV: Simulation and experimental data processing;” advisors: A. Camps and X.Bosch. Master Thesis UPC, 2008.

[5] Duperrier, A., “Soil Moisture Retrieval Using an Airbone L-Band Radiometer;” advisors: A. Camps and X.Bosch. Master Thesis UPC, 2008.

[6] Acevo, R., “UAV/airborne active and passive remote sensing instruments for Earth monitoring,” advisors: A. Aguasca. Diploma of Advanced Studies UPC, 2008.

[7] Monerris, A.; Rodriguez-Alvarez, N.; Vall-llossera, M.; Camps, A.; Piles, M.; Martinez-Fernandez, J.; Sanchez-Martin, N.; Perez-Gutierrez, C.; Baroncini-Turricchia, G.; Acevo, R.; Aguasca, A. “The GPS and RAdiometric Joint Observations Experiment at the REMEDHUS Site (Zamora-Salamanca Region, Spain).” *In Proceedings of the IEEE International Geoscience and Remote Sensing Symposium 2009*, Cape Town, South Africa 2009.

[8] Ulaby F. T., Moore R. K. & Fung A. K., “Microwave Remote Sensing. Active and Passive Vol I. Fundamentals and Radiometry,” Artech House, 1981a.

[9] Skou N., “Microwave Radiometer Systems: Design & Analysis,” Artech House, 1989.

[10] Stein, A., Van der Meer, F.; Gorte, B. “In Spatial Statistics for Remote Sensing: Remote Sensing and Digital Image Processing,” Eds. Kluwer Academic Publishers: Dordrecht, The Netherlands 1999.

[11] Monerris, A., “Experimental estimation of soil emissivity and its application to soil moisture retrieval in the SMOS mission”. PhD thesis dissertation, UPC, 2009.

[12] Wang, James R. Schmugge, Thomas J., “An Empirical Model for the Complex Dielectric Permittivity of Soils as a Function of Water Content”, Laboratory for Atmospheric Sciences, NASA/Goddard Space Flight Center, Greenbelt, 1980.

[13] Ferrazzoli P., Guerriero l., and Wigneron J.P., “Simulating L-Band Emission of Forests in View of Future Satellite Applications”, *IEEE Transactions on Geoscience and Remote Sensing,* Vol. 40, No. 12, pp. 2700-2708, December 2002.

[14] ECH2O Soil Moisture Sensor.
Available: http://www.decagon.com/ag_research/soil/ec5.php.

[15] Kerr, Y.H.; Waldteufel, P.; Wigneron, J.-P.; Delwart, S.; Cabot, F.; Boutin, J.; Escorihuela, M.-J.; Font, J.; Reul, N.; Gruhier, C.; Juglea, S.E.; Drinkwater, M.R.; Hahne, A.; Martín-Neira, M.; Mecklenburg, S.; , "The SMOS Mission: New Tool for Monitoring Key Elements of the Global Water Cycle," *Proceedings of the IEEE ,* vol.98, no.5, pp.666-687, May 2010

APENDIX A

Remote Sensing **2010**, *2*, 1-x manuscripts; doi:10.3390/rs20x000x

OPEN ACCESS

Remote Sensing

ISSN 2072-4292

www.mdpi.com/journal/remotesensing

Article

Design and First Results of an UAV-Borne L-Band Radiometer for Multiple Monitoring Purposes

Rene Acevo-Herrera [1,*], Albert Aguasca[1], Xavier Bosch-Lluis[1,2], Adriano Camps[1,2], José Martínez-Fernández[3], Nilda Sánchez-Martín[3], and Carlos Pérez-Gutiérrez[3]

1 Remote Sensing Lab, Dept. of Signal Theory and Communications, Universitat Politècnica de Catalunya, UPC Campus Nord D3, E-08034 Barcelona, Spain; E-Mail: aguasca@tsc.upc.edu

2 IEEC CRAE/UPC; E-Mails: xavier.bosch@tsc.upc.edu (X.B.-L.); camps@tsc.upc.edu (A.C.)

3 Centro Hispano-Luso de Investigaciones Agrarias (CIALE) Universidad de Salamanca - Parque Científico Campus de Villamayor C/ Río Duero, 12, E-37185 Villamayor (Salamanca), Spain; E-Mails: jmf@usal.es (J.M.-F.); nilda@usal.es (N.S.-M.); carpegu@usal.es (C.P.-G.)

* Author to whom correspondence should be addressed; E-Mail: rene.acevo@tsc.upc.edu; Tel.: +34-934017362.

Received: / Accepted: / Published:

Abstract: UAV (unmanned Aerial Vehicle) platforms represent a challenging opportunity to deploy a number of remote sensors. They are a cost-effective option in front of manned aerial vehicles (planes and helicopters), easy to deploy due to the short runways needed and they allow to meet the critical requirements of spatial and temporal resolutions imposed by the instruments. L-band radiometers are an interesting option to obtain soil moisture maps over local areas with relative high resolution spatial for precision agriculture, coastal monitoring, estimation of risk of fires, flood prevention, etc. This paper presents the design of a light-weight airborne L-band radiometer to be deployed in a small UAV, including the hardware and specific software developed for calibration, geo-referencing and soil moisture retrieval. First results and soil moisture retrievals from different field experiments are presented.

Keywords: UAV; Airborne sensors; Radiometer; Soil Moisture.

1. Introduction

The interest of the scientific community on the remote measurement of geophysical parameters such as the soil moisture (SM) or the sea surface salinity (SSS) has increased in the last years and much effort has been spent in that direction mainly by the European Space Agency (ESA) with the MIRAS/SMOS [1], and the National Aeronautics and Space Administration (NASA) with AQUARIUS/SAC-D [2, 3] and SMAP [4] missions. These space-borne radiometers have been optimized to measure these variables globally, at mesoscale resolution with short revisit time (~ 3 days): pixel size ~ 100 km for a 0.1 psu SSS accuracy, or pixel size ~ 50 km for a 4% SM accuracy. However, they are not adequate for regional or local applications where higher resolution imagery is required. Airborne microwave radiometers flying at low altitudes can fulfill this lack of information, improving the spatial resolution up to tens of meters and virtually without revisit time restrictions. Furthermore, these platforms are less sensitive to atmospheric effects. The SLFMR aboard a Beaver de Havilland [5] and MIRAMAP's radiometers [6] are examples of airborne radiometers. In this context, small unmanned aerial vehicles (UAV) have been found to be the ideal platforms for this kind of remote sensing applications [7], because they are easy to deploy, more flexible and offer a high level of re-configurability.

This work describes a radiometer system to perform soil moisture mapping from low altitude small UAVs platforms. The paper is organized as follows: Section 2 presents an introductory overview to the system. Section 3 analyses the onboard airborne radiometer. The software processor is presented in Section 4, focusing on the radiometer calibration, data geo-referencing and representation, data interpolation, and SM retrieval algorithms. Section 5 is devoted to analyze soil moisture measurements. Finally, Section 6 summarizes the main conclusions of this paper.

2. System description

There are a number of restrictions in the design process of the microwave radiometer and the platform. Assuming their use in precision farming, it is desired to have an absolute accuracy

lower than ≈ 10 K to determine SM with errors lower than 4%, and with a spatial resolution between 30 to 150 m flying at altitudes up to 300 m.

The use of UAV platforms to carry remote sensors imposes not only strong constrains in size, weight, power consumption, but an extra effort has to be made to increase the robustness of the instrument due to the strong vibrations induced by the engine. These can reach more than 6 g for gasoline engine powered radio-controlled aircrafts, so that special care must be taken in the whole system design process.

The main parts of the system that are deployed in the UAV platform are: the L-band Radiometer including the antenna, a Global Positioning System (GPS) receiver, an Inertial Motion Unit (GPS-IMU), and the datalogger. Different UAVs platforms have been used, all of them with 2.5 m wingspan and 2 m length (Figure 1).These UAV are able to fly at altitudes up to 400 m, with cruise speeds between 25 - 45 m/s, with an endurance up to 20 min carrying a payload up to 3.5 kg.

The platform is provided with the GPS-IMU for the purpose of geo-reference the collected radiometric data. Radiometer's output signal, the attitude (roll, pitch and yaw), the altitude, and the aircraft speed (v_x, v_y, v_z) are properly recorded at a sampling rate of 50 samples per second, by the on-board data-loggers for later data processing.

Figure 1. The UAV during a test flight. The ARIEL antenna is located below the fuselage.

3. Airborne L-band radiometer

A single polarization nadir-looking Dicke radiometer was selected and implemented, due to its simplicity and sufficient stability, when thermally stabilized. The system was designed to require external periodic calibration only at the beginning and at the end of each flight (≥20 min).

An important issue to take into account is the antenna. The antenna dimensions at L-band are comparable to the size of the UAV itself if a narrow beamwidth is desired (e.g. less than 25º in

both planes). Furthermore, it has to be specifically designed in order to reduce its influence in the UAV aerodynamics, while preserving the desired performance for radiometric applications. The designed antenna (Figure 2a) is a flat hexagonal 7-patch array with a 22º beam width in both dimensions [8]. The measured gain, directivity and radiation ohmic efficiency of this antenna are 15.88 dB, 16.03 dB and 96.5 %. The effect of a variation of the antenna ohmic losses due to temperature fluctuations is minimized by incorporating a thermal control attached to antenna ground plane.

Figure 2. (a) Setup for the antenna pattern measurement showing the antenna mounted on the UAV at the anechoic chamber of the Dept. of Signal Theory and Communications, Universitat Politècnica de Catalunya [9]. **(b)** Measured full radiation pattern. **(c)** Simulated and measured Copolar radiation pattern at E-plane. Simulation only considered ideal isotropic radiation elements thus slightly differences between simulated and measured results can be distinguished. **(d)** Measured cross-polar radiation pattern for the E-plane.

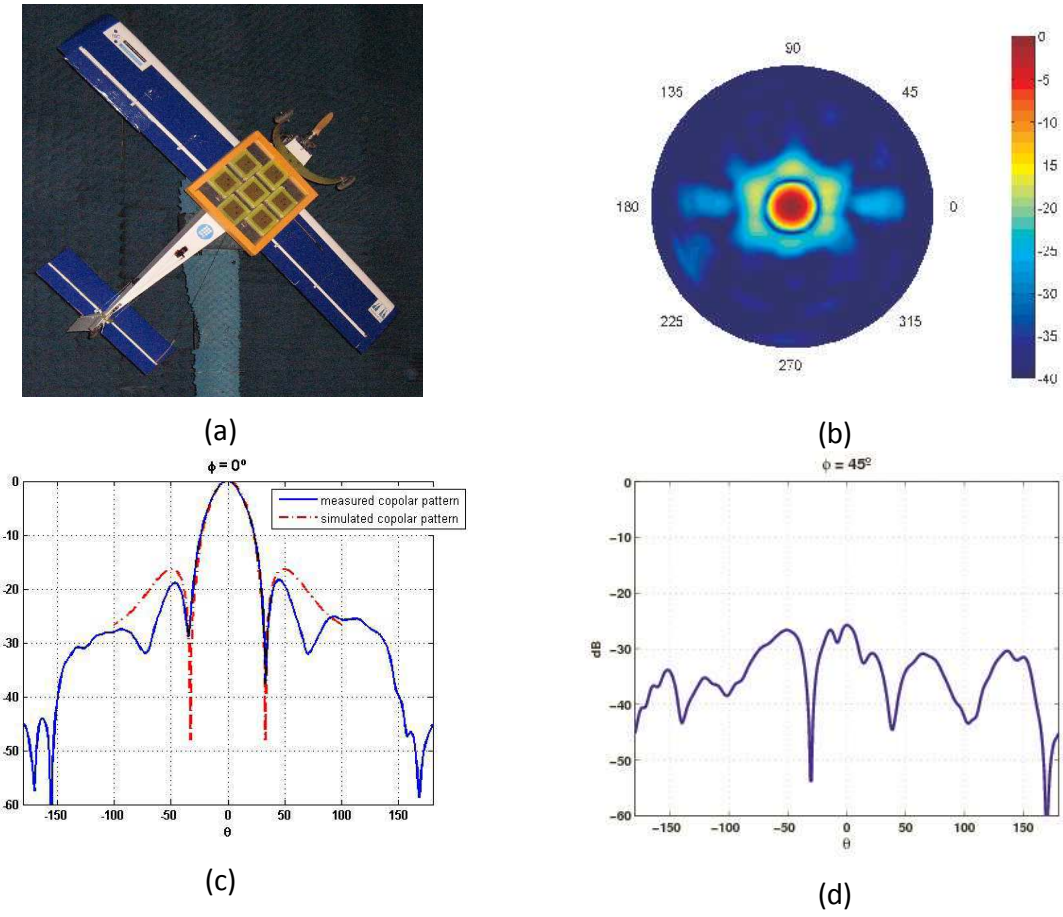

The Airborne RadIomEter (ARIEL) at L-band (1.4 GHz) block diagram is shown in Figure 3. The heterodyne receiver is divided in three main blocks: the RF front-end, the down-converter, and the detection block. The RF front-end (1400 MHz to 1427 MHz) includes the Dicke switch, alternating the detected power between the signal from the antenna and from a matched load. This signal is properly filtered, amplified, and down-converted to baseband where it is detected using a true rms-detector (output voltage proportional to signal's standard deviation) followed by a square law amplifier. Finally, the signal is synchronously demodulated, low-pass filtered and conditioned before the analog to digital conversion process.

Figure 3. ARIEL Block Diagram.

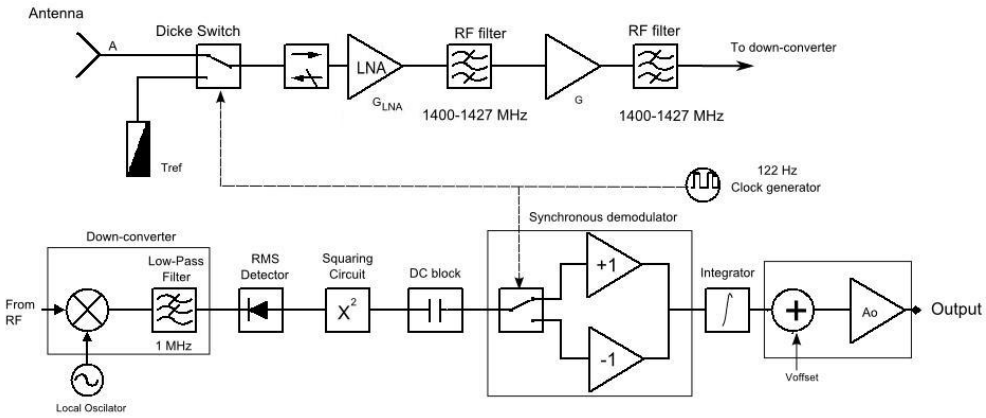

The radiometric sensitivity ΔT of a balanced Dicke radiometer is [10]:

$$\Delta T = \frac{2(T_{REF} + T_{REC})}{\sqrt{B\tau}}, \tag{1}$$

where T_{REF} = 315 K is the physical temperature of the reference load, $T_{REC} \approx$ 790 K is the receiver's noise temperature, $B \approx$ 30 MHz is the system's noise bandwidth, and τ is the integration time.

The maximum integration time is determined by the minimum dwell time according to,

$$\frac{FP_{\min}}{v_{\max}} = \frac{BW \cdot h_{\min}}{v_{\max}}, \tag{2}$$

where $FP_{\min}$ is the smallest footprint, BW is the antenna beamwidth, $h_{\min}$ is the minimum flight height, and $v_{\max}$ is the maximum flight speed. With these parameters the theoretical radiometric resolution is ΔT = 1.27 K for an integration time τ=100 ms.

The radiometer was implemented using commercial "off-the-shelf" components. The radiometer front-end was integrated in a 100 x 60 x 15 mm monoblock box (Figure 4). The total

weight including the batteries, the antenna and its radome is less than 3 kg. If the thermal control of the radiometer is included, the total power consumption of the system is less than 10 W, which facilitates the use of light weight Lithium Polymer batteries as the main power supply.

Figure 4. ARIEL RF front end 100 x 60 x 20 mm compared to a 1 euro coin.

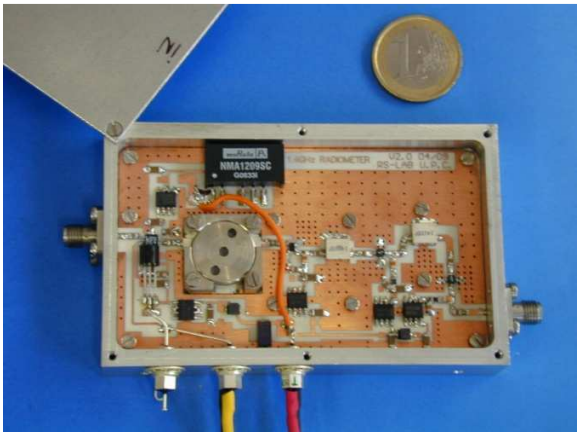

4. ARIEL soil moisture retrieval processor

A specific software processor for soil moisture retrieval has been developed to retrieve soil moisture maps from the radiometric measurements. The input data files (GPS, IMU, attitude, and raw radiometric data) are selected from a specific graphical user interface (GUI), where the radiometric calibration procedure is defined. This radiometric data calibration procedure is performed before, after or before and after the flight according to an established protocol. Figure 5a shows this calibration process. The calibration is based on the selection of the intervals in the raw data where the hot/cold loads were measured.

Two independent dataloggers are used, one for the GPS and the other for the inertial/radiometric data. To synchronize their data cross-correlation techniques using the altitude information from GPS and the one from barometer are used (Figure 5b).

Figure 5. Data processing **(a)** selection of calibration intervals, **(b)** data synchronization.

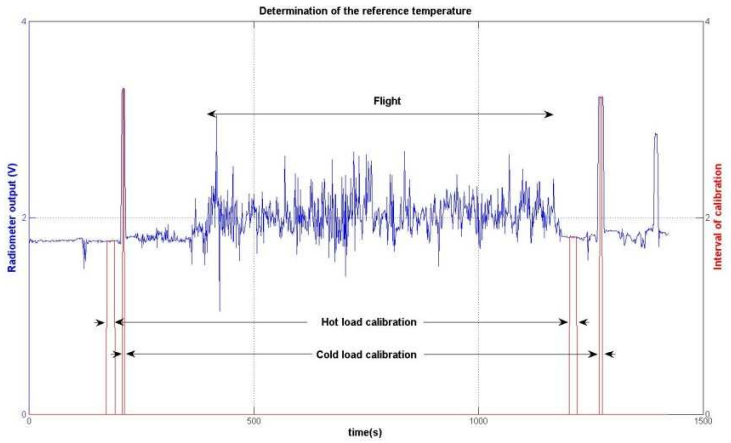

(a) Calibration of radiometer output

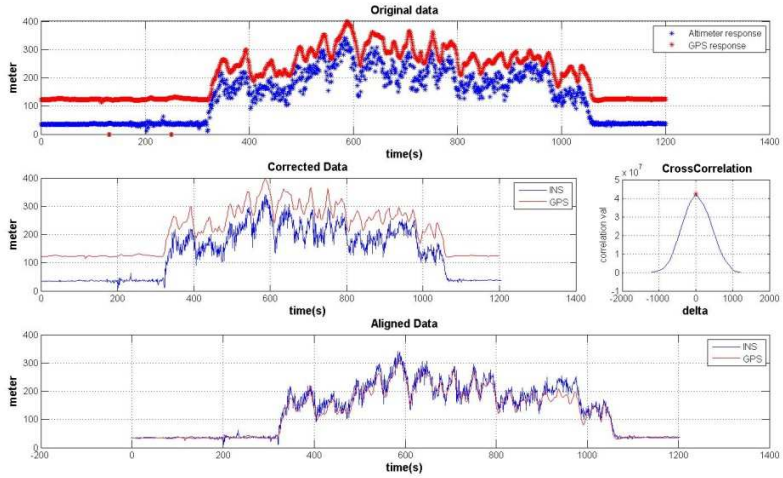

(b) Synchronization of the altitude data from GPS data and barometric information

Histograms can also be plotted to detect relevant information such as intervals of interest, and extracting the desired ranges of antenna temperatures or aircraft height; as shown in Figure 6a. Interesting parameters to be displayed are the antenna temperature and soil moisture maps in time intervals. The flight trajectory can be illustrated together with the corresponding antenna footprints plotted along the ground track (Figure 6b). The processor includes attitude and altitude filters to limit the range of valid incidence angles, eliminate Sun glints at high banking angles, radio frequency interference (RFI) peaks, or potential recording errors of the dataloggers.

Figure 6. Images showing the kind of target present in the scene. Test performed in a coastal zone. **(a)** Histogram plot in which different targets and other signals could be distinguished during the measurement: soil, water, calibration, sun glints. **(b)** Trajectory plot of the flight superimposed with brightness temperatures.

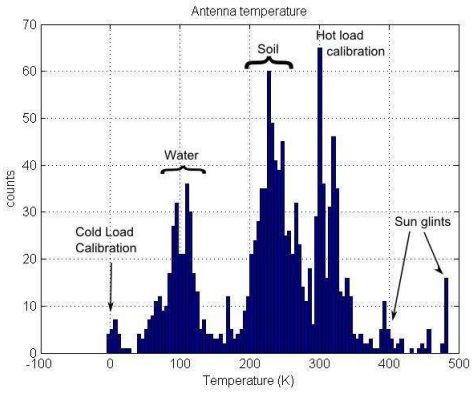

(a)

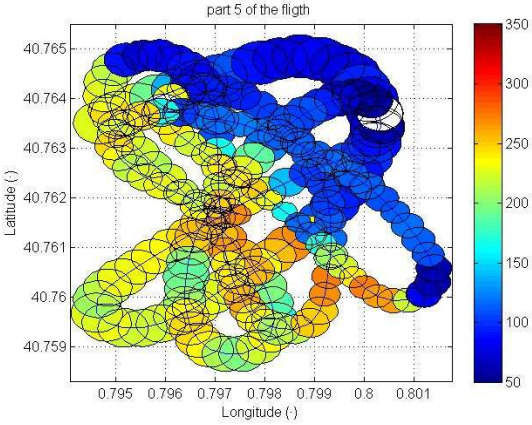

(b)

Finally, in order to fully cover a specific area (typically 1 km x 1 km) with the UAV flying at low altitudes (under 300 m), the flight plan is designed in such a way that several overpasses at different heights (i.e. with different spatial resolutions) are obtained. In order to merge all the collected information, each footprint has to be properly weighted with the antenna's radiation pattern. Therefore, interpolation techniques have been developed to obtain images with soil moisture or antenna temperature information (Section 4.1.3). These images are then geo-referenced and linked to a map using Keyhole-Mark-up-Language (KML) [11] files that can be superimposed on Google Earth maps for a better interpretation.

4.1. Algorithm description and procedures

The soil moisture retrieval algorithm proceeds as follows:

- Raw data re-sampling.
- Radiometric calibration.
- Ground projection of the antenna footprint, taking into account the attitude and position of the platform.
- Spatial interpolation.
- Soil moisture retrieval.

The algorithm is described step by step in the following sections.

4.1.1. Data re-sampling

GPS largest errors are in the vertical direction. A barometric sensor is used to correct this information, and to refer all heights to ground level to properly compute the antenna footprints. In order to geo-reference the radiometric data it is necessary to synchronize the barometric

altimeter, the GPS and the radiometric data, since they are acquired at different sampling frequencies and different dataloggers. The altitude is referenced to ground's altitude in order to properly compute the antenna footprints.

4.1.2. Radiometric calibration

Radiometer's raw-data are converted into antenna temperatures through the radiometric calibration. In a Dicke radiometer, the relationship between its output voltage v_o and the antenna temperature can be expressed as [10]:

$$v_o = a(T_{REF} - T_A) + b\,, \tag{3}$$

where T_{REF} is the temperature of the reference load (measured with a thermometer), T_A is the antenna temperature, and a and b are gain and offset constants to be determined during the absolute calibration with the hot-cold method [12]. A thermally isolated microwave absorber placed just in front of the antenna is used as hot load, and pointing the antenna to the sky gives the equivalent to a cold load.

In case of temperature drifts during the flight, a linear behaviour between two hot/cold load calibrations, performed just before and after the flight, is assumed. In this case the calibrations parameters can be determined as follows:

$$a(t) = a_b + \frac{a_f - a_b}{t_f - t_b}(t - t_b), \tag{4a}$$

and

$$b(t) = b_b + \frac{b_f - b_b}{t_f - t_b}(t - t_b), \tag{4b}$$

where t is the time and the subscripts b and f mean before and end the flight.

Finally, the time dependent coefficients $a(t)$ and $b(t)$ are used with T_{REF} to compute the calibrated antenna temperature at each sample. In case of failure of all calibrations, a laboratory calibration with constant coefficients measured in the anechoic chamber can be used. For an integration time of τ = 100 ms the measured calibration standards have standard deviations of σ_{hot} = 0.0045 V and σ_{cold} = 0.0052 V, which translate into sensitivities of ΔT_{hot} = 0.84 K and ΔT_{cold} = 1.22 K, in agreement with theoretical predictions (section 3).

4.1.3. Data merging and spatial interpolation

Once the flight trajectory has been determined, the ground projection is performed and the footprint size and shape are determined. Then the radiometric data have to be properly processed

in order to obtain the geocoded SM map that can be linked to a KML file, to be finally overlaid with Google Earth maps. As described before, the data sampling rate is $f_s = 50\,\text{Hz}$ and the UAV speed is $v_{UAV} \approx 40\,m/s$. That means that the aircraft has moved 0.8 m between consecutive samples. If an average footprint of 100 m is considered, the pixels have a high-level of overlapping, and so data must be properly interpolated.

For geo-statistical applications the Kriging method [13] provides the optimal interpolator. It assigns weights according to a data-driven weighting function (spatial covariance values obtained through a semivariogram). However, for simplicity and computational speed considerations, the algorithm performs an alternative method assigning a weight to each footprint according to the modified two-dimensional (bivariate) Gaussian density function (*GDF*) that best fits the antenna pattern mainlobe. Each GDF has been adjusted to ensure that at the 3dB antenna footprint contour the GDF value falls to the half of the maximum (-3 dB in antenna terms).

Finally, the resulting pixel is the merge of all values of such footprints that intersect a given pixel. Every temperature value of the pixel is obtained from a weighted average of the different looks:

$$\hat{Z}_i = \frac{\sum_{k=1}^{n} GDF_k(d_k) \cdot Z_k}{\sum_{k=1}^{n} GDF_k(d_k)}, \tag{5}$$

where Z_k is the value of the k^{th} contributing antenna footprint, $\hat{Z}_i$ is the estimated value for the pixel i^{th}, d_k is the distance to the center of the pixel to the center of the k^{th} contributing antenna footprint, GDF_k is the *GDF* of the k^{th} contributing antenna footprint, and n is the total number of contributing footprints.

In this procedure the footprints generated at lower altitudes will have a higher influence on the obtained pixel. In addition, only footprints with incidence angles lower or equal to 10º are computed in the process to ensure nadir look observations, as it will be further explained in the following section.

4.2. Soil Moisture retrieval

The brightness temperature of the surface is measured by an antenna far away. In this case, the apparent temperature T_{AP} is the key parameter that depends on the brightness temperature of the surface under observation (T_B), the atmospheric upward radiation (T_{UP}), the atmospheric downward radiation scattered reflected by the surface (T_{SC}), and the atmospheric attenuation (L_a). The downward radiation is mainly generated by the cosmic radiation level of the sky T ≈ 2.7 K at L-band, and the downwelling atmospheric contribution T_{DNatm} ≈ 2.1 K at zenith. These values are

fairly constants and will not affect the quality of the measurement and are usually ignored. Since $T_{UP} \approx 0$ at low altitudes, T_{SC} is much smaller than the required accuracy and $L_a \approx 1$ (for $\theta = 0°$), at low altitudes, the apparent temperature T_{AP} at L-band can be approximated by the temperature emitted by the surface (T_B) weighted by the antenna pattern.

$$T_A = \frac{1}{\Omega_p} \iint_{4\pi} T_{AP}(\theta,\phi) \left| F_n(\theta,\phi) \right|^2 d\Omega, \tag{6}$$

where $F_n(\theta,\phi)$ is the normalized antenna voltage pattern, and Ω_p is the equivalent antenna beam solid angle, and θ is the incidence angle.

The brightness temperature T_B of a soil covered by vegetation is usually estimated as the contribution of three terms: (i) the radiation from the soil that is attenuated by the overlying vegetation, (ii) the upward radiation from the vegetation, and (iii) the downward radiation from the vegetation, reflected by the soil, and attenuated by the canopy [12]

$$T_{Bp}^{\text{model}} = \left(1 + \frac{1 - e_{bs}}{L_{veg}}\right)\left(1 - \frac{1}{L_{veg}}\right)(1-\omega) T_{veg} + \frac{e_{bs}}{L_{veg}} T_{soil}, \tag{7}$$

where $e_{bs} = \left(1 - \Gamma^p\right)$ is the bare soil emissivity, Γ is the reflection coefficient, p is the polarization, T_{veg} and T_{soil} are the physical temperatures of the vegetation and soil respectively, $L_{veg} = \exp(\tau \cdot \sec\theta)$ [Np] is the attenuation due to the vegetation cover, $\tau = b \times VWC$ is the optical thickness, b [m^2/kg] is a vegetation dependent factor [14], VWC is the vegetation water content [kg/m^2], and ω is the single scattering albedo. This formulation is known as the τ-ω model [14] and is based on the single scattering approach proposed in [15].

In the case of bare soil: τ =0, $L_{veg} \approx 1$ and ω=0 and (7) reduces to

$$T_B^p(\theta) = \left(1 - \Gamma^p(\theta)\right) T_{soil} \tag{8}$$

where the reflection coefficient at the air-ground interface $\Gamma^p(\theta)$ is computed using the Wang model [16] as:

$$\Gamma^p(\theta) = \left[(1 - Q_s) \cdot \Gamma^{spec,p}(\theta) + Q_s \cdot \Gamma^{spec,q}(\theta)\right] \cdot \exp\left(-h_s \cos^n \theta\right), \tag{9}$$

where Q_s is the mixing polarization parameter and h_s is the surface roughness, and both are functions of the frequency. Recent studies have shown that h_s also depends on soil moisture [17]. In order to retrieve soil moisture from the antenna temperature at a single direction some assumptions are made:

- The soil is bare and smooth (surface roughness parameter h_s = 0).

- Only incidence angles smaller than 10º have been retained, since the angular dependence of T_B around 0° is weak.

To determine the impact of the incidence angle, the emissivity of a bare flat soil is plotted versus soil moisture for three different incidence angles (θ = 0°, 10°, 30°; Figure 7a). It could be seen that for incidence angles up to 10° the error is smaller than 1% compared with a 0º incidence. For incidence angles up to 30° the error rises to 6%. In Figure 7b the impact of vegetation cover is illustrated, showing the emissivity of soil versus SM for two different kinds of soils: bare soil and wheat. Compared with a bare soil, the error is 6% for 22 cm height vegetation and 15% for 60 cm vegetation, these values are obtained with an incidence angle of θ =0º.

Figure 7. Emissivity as a function of SM for **(a)** a bare flat soil versus SM at three different angles (θ = 0°, 10°, 30°). The error compared with a θ = 0º is: 1% at θ =10º, and 6% at θ =30º, **(b)** for two different kind of soils: bare soil and pasture. The error is: 6% for 22 cm height vegetation and 15% for 60 cm height vegetation at θ =0º.

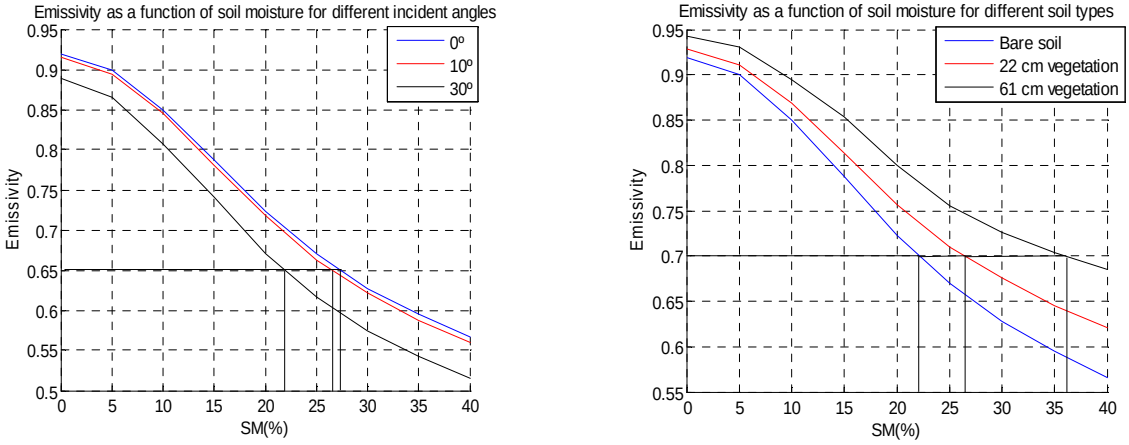

(a) (b)

In order to speed up the retrieval process an emissivity look up table has been created with SM entries. The scattered radiation is also included for average soil moisture conditions [12]. Then for a given T_{ph} and T_A the SM is readily estimated.

5. Experimental results

Three experimental field campaigns have been conducted over different scenarios to retrieve soil moisture maps. The selected scenarios were:

1) Ripollet site surroundings (Barcelona, Spain), used for agricultural applications: land and crop monitoring, with different irrigation levels,

2) Ebro river mouth (Deltebre, Spain), not presented in this work, used for agricultural (rice fields) and coastal applications [18], and

3) REMEDHUS site (Salamanca, Spain), used for SMOS calibration and validation (CAL/VAL) activities [19].

5.1. Soil moisture measurements at Ripollet site surroundings

The Ripollet site surroundings were chosen because it has a radio control model flying club near agricultural fields, which showed interesting changes in soil moisture during the first half of 2009 due to the different irrigation levels along winter and spring. A measured soil moisture map from the Ripollet field is displayed in Figure 8a. The flight correspond to April 29th (DoY = 119), 2009. *In situ* ground truth measurements were taken with a moisture sensor ECH$_2$O EC-5 [20] at a vertical depth of 5 cm. Measurements were performed averaging 2 samples, the positions of the soil moisture measurements were geo-coded using a commercial GPS receiver. The soil moisture ground truth (SM-GT) map was spatially interpolated with the same pixel resolution of the retrieved SM map and is shown in Figure 8b.

Figure 8. Experimental results of the Ripollet site surroundings, April 29th (DoY=119), 2009. Google earth image size 1.5 km x 1 km. **(a)** Soil moisture map of Ripollet agricultural fields. **(b)** Ground truth soil moisture map of Ripollet.

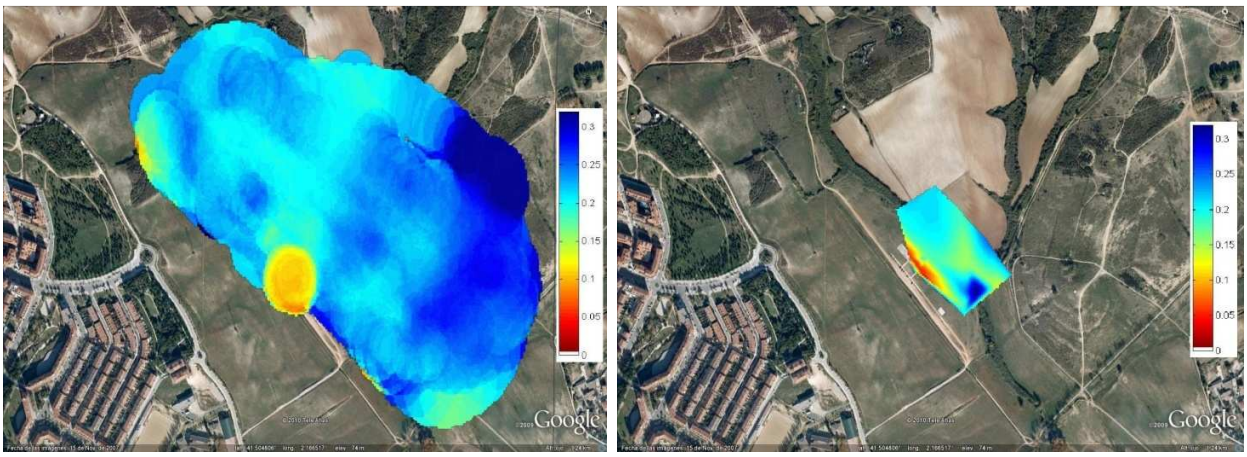

(a) (b)

Figure 9 shows an error map of the retrieved soil moisture with ARIEL versus the ground truth measurements. In the upper left part of the error image the absolute value varies from 6 % to 9 %. In this zone there is a hill with a 10% slope covered by dense wheat fields. In the center of the image the error reaches to 1%. There are two noticeable regions (shown in red) where the error reaches up to 16%. One region corresponds to the aircraft runway made of concrete, and the other is covered by tall vegetation (3 m height cane).

Figure 9. Retrieved soil moisture error map with ARIEL compared to ground truth measurements. In the center of the image the absolute error reaches 1% and rises up to 9 % in the upper left (data cursor value is 8.27%). Two noticeable zones (red and yellow), where the error reaches up to 16% being the runway and a tall vegetation area (3 m height cane).

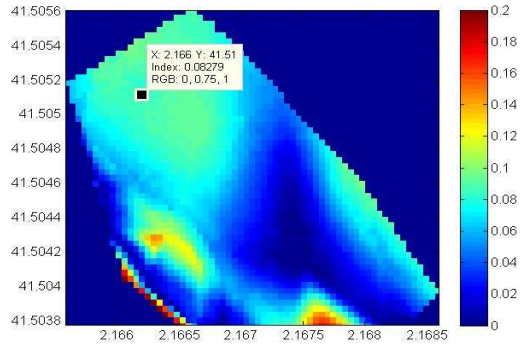

5.2. Soil moisture retrieval tests at the REMEDHUS, SMOS CAL/VAL site Zamora, Spain

GRAJO (GPS and Radiometric Joint Observations) is a joint initiative between UPC and the Centro Hispano Luso de Investigaciones Agrarias (CIALE)/ Universidad de Salamanca (USAL). The CIALE group is in charge of the *in situ* measurements using TDR and Hydra Probes automatics sensors [21] in order to obtain simultaneously soil moisture and temperature at 5, 25, and 50 cm depth. UPC is in charge of the radiometric and the GPS reflectometer data acquisitions.

The GRAJO field campaigns in support to the SMOS calibration/validation have been carried out in Vadillo de la Guareña, Zamora, Spain from November 2008 until May 2010 [19].

The objectives of GRAJO are threefold:

- Validation and calibration of the SMOS-derived soil moisture map, at SMOS pixel-size level.
- Study of the variability of soil moisture within the SMOS footprint.
- Test of pixel disaggregation techniques development in order to improve the spatial resolution of SMOS observations. These algorithms have been tested using airborne radiometric measurements over REMEDHUS acquired with the ARIEL radiometer.

The experiment with ARIEL at the REMEDHUS test site was planned to be performed over this very heterogeneous area, where the measured SM has variations from 2 through 50% in a 2 km^2 area. These conditions allowed to validate the SM retrieval algorithm over those different kind of terrains and SM values. Its feasibility could be tested thanks to the information from a ground-truth SM map provided by CIALE.

Figure 10 shows a land use map of the area where four kinds of soil can be distinguished: cereal, vineyard, human made buildings, and rangeland. There are also rural ways, trees, and a creek. This kind of land use implies a high degree of variability of the SM with abrupt changes.

Figure 10. Land use map for the experiment in Vadillo de la Guareña (Zamora, Spain).

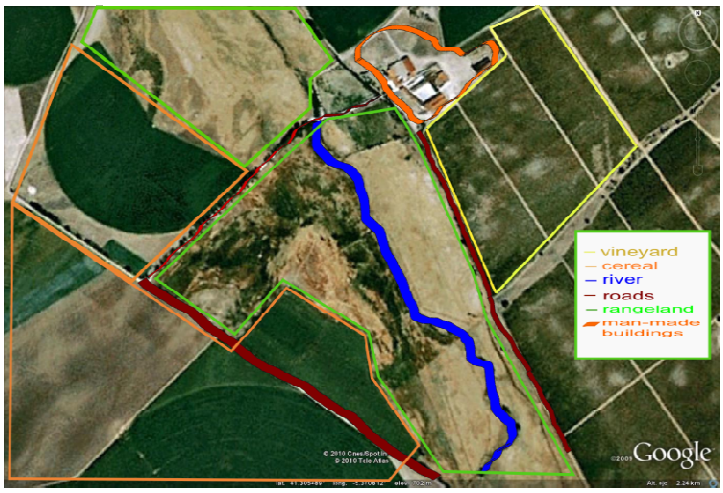

Flight measurements were carried out in the morning right after the sunrise and in the evening right before sunset in order to reduce the effect of Sun interferences due to reflections over the terrain. The retrieved soil moisture maps from two flights are plotted in Figure 11a. Figure 11b shows the soil moisture ground truth map obtained by the CIALE/USAL team, which has been generated using Kriging interpolation techniques. The ground truth maps show variations in SM from 2% to almost 50%.

Figure 11. Experimental measurements in Vadillo de la Guareña (Zamora, Spain), March 25th (DoY=84), 2009. **(a)** Soil moisture map mixing two different flights (square area of 2.28 km^2). Flight 1 covers the right image part and flight 2 the left one. **(b)** Ground-truth soil moisture map provided by CIALE/USAL.

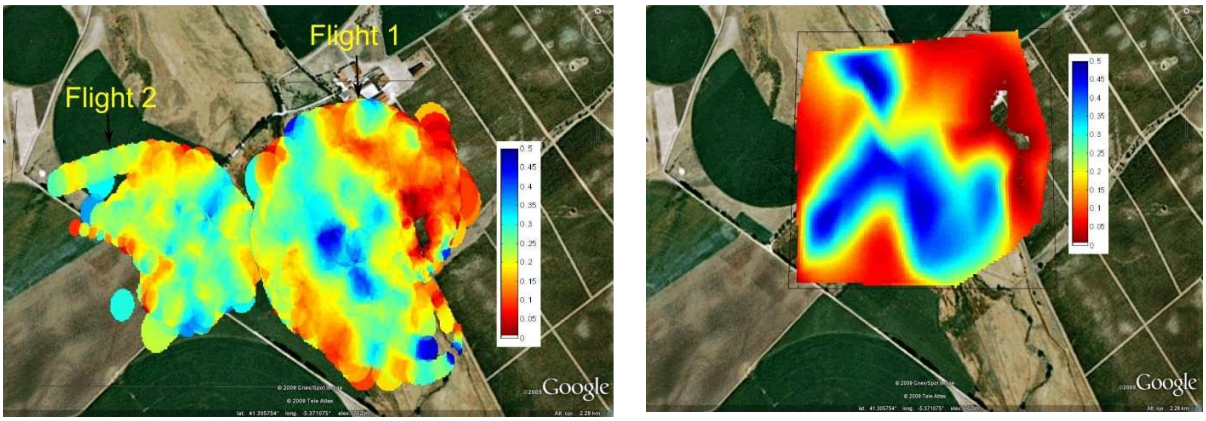

(a) (b)

Since the experiment was carried out in a very heterogeneous area, the most homogeneous zones with lower variations in the SM (up to 15%) are analyzed first. Figure 12a shows the error map between the retrieved SM map from flight 1 (figure 11.a) and the ground truth measurements (figure 11.b) of part of the scenario (center of figure 11.a). The ground truth showed a variation of SM from 25% to 40%, and the obtained error map (difference between retrieved SM and ground truth in %) goes from 1% to 6%. The same results are obtained in other parts of the scenario. Figure 12b shows the error map of the left part of the scenario with information retrieved from 2nd flight. As it could be noticed the same results are obtained in this flight.

Figure 12. Error maps for the homogeneous zone **(a)** from retrieved SM (flight 1) versus ground truth measurements, **(b)** from retrieved SM (flight 2) versus ground truth measurements.

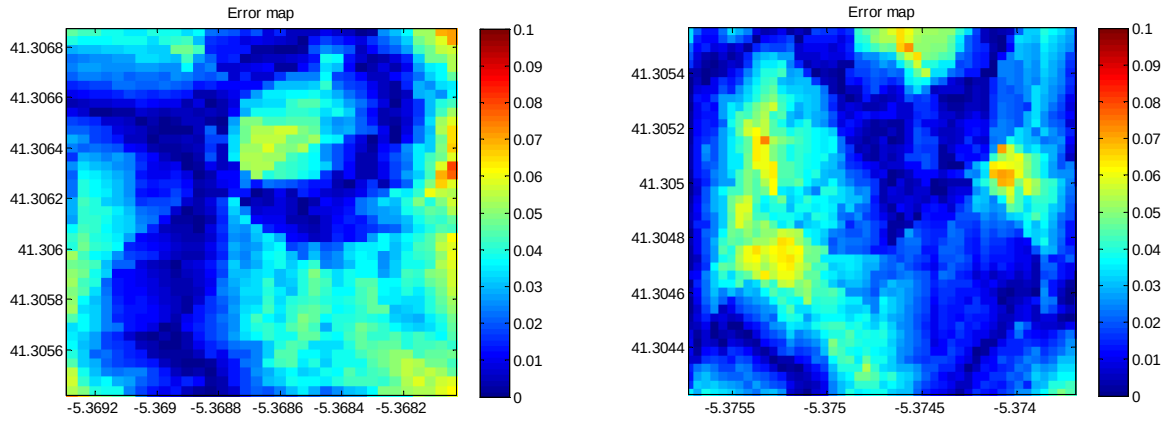

(a) (b)

Figure 13a shows the error map in the complete image, it is easy to see that this absolute error increases at the corners of the area from 12% up to 20 % due to the substantial reduction of the number of overpasses. It must be pointed out that some areas showed variations in SM from 4 to 46 % at distances closer than 70 m. These areas have been interpolated by the radiometer if a footprint of 100 m is observed that implies a large error in the retrieved SM value.

Figure 13b represents the error map in the complete image from the second flight. There are two zones in the center of the image where the error reaches 20%, for which some considerations must be taken into account. The flight was performed in the afternoon, and the ground truth map was taken in the morning simultaneously to the first flight so that in this zone the variability in SM is higher due to the drying. One limitation to generate ground truth maps with interpolation methods is the variability of SM values in short distances. A source of error in the ground truth information is the accuracy of the sensor that in this case is 1.5 % [21].

Figure 13. Error maps for the full areas **(a)** from retrieved SM versus ground truth measurements of flight 1, **(b)** from retrieved SM versus ground truth measurements of flight 2. The dark blue points show the locations of the ground truth measurements.

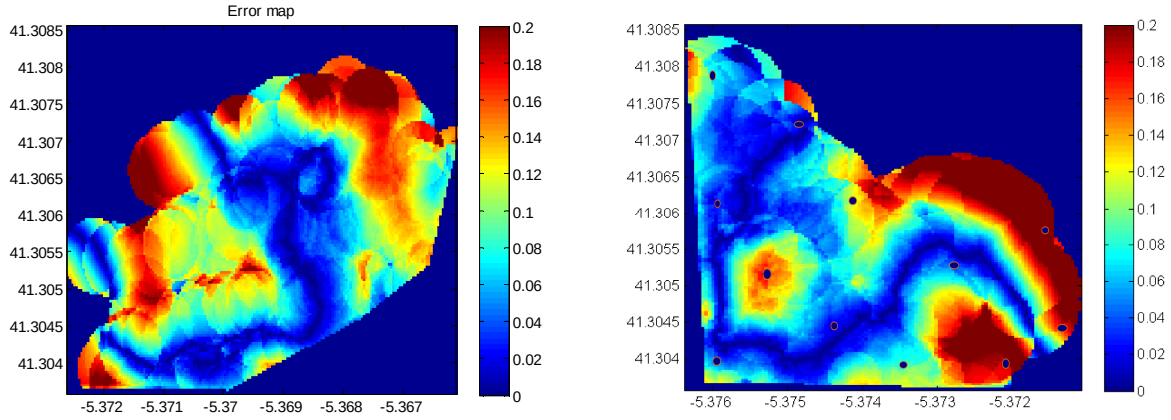

(a) (b)

To better understand these large differences, biophysical parameters of the vegetation present in the site are provided in table 1. The VWC was determined during the measurement and the normalized difference vegetation index (NDVI) was measured with a USB4000 miniature fiber optic spectrometer from ocean optics.

Table 1. Biophysical parameters of the vegetation present in Vadillo de la Guareña (Zamora, Spain), March 25th (DoY=84), 2009.

	NDVI	Growing Cycle	VWC (%)	FVC (%)
Grass/Pasture	0.60 to 0.85	Development	66 to 78	55 to 75
Barley/Cereal	0.63 to 0.72	Development	70 to 75	49 to 61
Vineyard	-0.01 to 0	Dormancy	--	--
Unproductive	-0.05 to 0	--	--	--

Based on table 1 information and on the land use map of figure 10, the best results in the first flight were obtained over unproductive areas (bare soil or poor vegetation). The average errors were obtained over grass/pasture zones where higher vegetation index were present.

The largest errors are obtained in the vineyard area. Although its low vegetation index with poor water content this area has a particular orography, with a 10% slope and a road (without ground truth information) that separates a very dense grass zone from the vineyard. Furthermore, this part of the scenario was not well covered during the flight and then few footprints contribute to the pixels.

In the second flight the biggest errors are present over cereal zones where a high vegetation index is present. The same performance occurs over the roads where is not possible to have ground truth information.

Other noticeable artifact in the image of figure 11.a is an apparent circular feature of the SM retrieved maps. It occurs in the zones where few over flights were performed, which means that few samples contribute to the pixel generation and the antenna footprint is depicted.

6. Conclusions

This work has presented the design and development of an airborne light weight radiometer at L-band (ARIEL). It also presents the software processor that includes different calibration techniques and interpolation and merging techniques. These techniques allow immediate processing of the data just at the end of the flight.

The flexibility of the UAV system has been applied for soil moisture mapping in cereal and vineyard fields located in the REMEDHUS SMOS CAL/VAL site. Results show that geo-referenced Google Earth maps of soil moisture and brightness temperature maps were obtained with estimated absolute errors between 1% to 6%, these results where obtained at homogeneous zones of agricultural fields.

The experimental tests planned in heterogeneous and vegetation covered soils show large errors where abrupt changes in SM are present and Krigging interpolation is prone to larger

errors. The best results are obtained over more homogeneous zones, and the best image quality is achieved over the zones in which more overflights where performed.

Some improvements on the system are planned in order to increase the resolution. Also a unique GPS-IMU unit will be included to avoid data re-sampling.

Acknowledgements

This project has been supported by the projects: MIDAS-5 ESP2007-65667-C04-02 and AYA 2008-05906-C02-01/ESP, TEC 2005.

This project has been supported by a grant of Universitat Politècnica de Catalunya, UPC Pre-PhD Scholarships.

This work, conducted as part of the award "Passive Advanced Unit (PAU): A Hybrid L-band Radiometer, GNSS-Reflectometer and IR-Radiometer for Passive Remote Sensing of the Ocean" made under the European Heads of Research Councils and European Science Foundation EURYI (European Young Investigator) Awards scheme in 2004, was supported by funds from the Participating Organizations of EURYI and the EC Sixth Framework Program.

References and Notes

1. Kerr, Y. H.; Waldteufel, P.; Wigneron, J. -.; Martinuzzi, J.; Font, J.; Berger, M. Soil moisture retrieval from space: the Soil Moisture and Ocean Salinity (SMOS) mission. *IEEE Trans. Geosci. Remote Sens.* **2001**, *39*, 1729-1735.
2. Lagerloef, G.; LeVine, D.; Chao, Y.; Colomb, R. Aquarius/SAC-D Mission; a key to Understanding the Links Between Salinity and Climate Variability. *AGU-ASLO* **2005**.
3. Le Vine, D. M.; Lagerloef, G. S. E.; Colomb, F. R.; Yueh, S. H.; Pellerano, F. A. Aquarius: An Instrument to Monitor Sea Surface Salinity From Space. *IEEE Trans. Geosci. Remote Sens.* **2007**, *45*, 2040-2050.
4. Committee on Earth Science and Applications from Space: A Community Assessment and Strategy for the Future, National Research Council. Earth Science and Applications from Space: National Imperatives for the Next Decade and Beyond. *http://www.nap.edu*, **2007**.
5. Miller, J. L.; Goodberlet, M. A.; Zaitzeff, J. B. Airborne Salinity Mapper Makes Debut in Coastal Zone. *Transactions American Geophysical Union EOS* **1998**, *79*, 173-177.
6. Haarbrink, R.; Shutko, A. New Airborne Sensor for Soil Moisture Mapping. In *Proceedings of the Second International Workshop on The Future of Remote Sensing, ISPRS Inter-Commission WG I/V, Autonomous Navigation, VITO/ISPRS,* Antwerp, Belgium, October **2006**.
7. McIntyre, E. M.; Gasiewski, A. J.; Leuski, V. Development of a Lobe-Differencing Correlation Radiometer (LDCR) for Airborne UAV SSS Mapping. In *Proceedings of the*

IEEE International Geoscience and Remote Sensing Symposium 2007, Barcelona, Spain, **2007**, pp 1095-1097.

8. Valencia, E.; Acevo, R.; Bosch-Lluis, X.; Aguasca, A.; Rodriguez-Alvarez, N.; Ramos-Perez, I.; Marchan-Hernandez, J. F.; Glenat, M.; Bou, F.; Camps, A. Initial Results of an Airborne Light-Weight L-Band Radiometer. In *Proceedings of the IEEE International Geoscience and Remote Sensing Symposium 2008,* Boston, MA, USA, **2008**, *2*, II-1176-II-1179.
9. Remote Sensing Laboratory http://www.tsc.upc.edu/rslab/index.php.
10. Skou, N.; Le Vine, D. In *Microwave Radiometer Systems Design and Analysis,*2nd Ed. Artech House, Inc.: Norwood, MA, USA, 2006; 222 p.
11. KML standard http://www.opengeospatial.org/standards/kml/.
12. Ulaby, F. T.; Moore, R. K.; Fung, A. K. In *Microwave Remote Sensing. Active and Passive Vol I. Fundamentals and Radiometry,* 1st Ed. Addison-Wesley, Advanced Book Program: Reading, Massachusetts, USA, 1981; 456 p.
13. In *Spatial Statistics for Remote Sensing: Remote Sensing and Digital Image Processing,* Stein, A.; Van der Meer, F.; Gorte, B. Eds.; Kluwer Academic Publishers: Dordrecht, The Netherlands 1999; 300 p.
14. Van de Griend, A. A.; Wigneron, J. -. The b-factor as a Function of Frequency and Canopy Type at H-polarization. *IEEE Trans. Geosci. Remote Sens.* **2004**, 42, 786-794.
15. Kirdiashev, K. P.; Chukhlantsev, A. A.; Shutko, A. M. Microwave Radiation of the Earth's Surface in the Presence of Vegetation Cover . *Radio Eng. Electron. Phys.* **1979**, *2*, 37-56.
16. Wang, J. R.; Schmugge, T. J. An Empirical Model for the Complex Dielectric Permittivity of Soils as a Function of Water Content. *IEEE Trans. Geosci. Remote Sens.* **1980**, *18*, 288-296.
17. Escorihuela, M. J.; Kerr, Y. H.; de Rosnay, P.; Wigneron, J. -.; Calvet, J. -.; Lemaitre, F. A Simple Model of the Bare Soil Microwave Emission at L-Band. *IEEE Trans. Geosci. Remote Sens.* **2007**, 45, 1978-1987.
18. Acevo-Herrera, R.; Aguasca, A.; Bosch-Lluis, X.; Camps, A. On the Use of Compact L-band Dicke Radiometer (ARIEL) and UAV for Soil Moisture and Salinity Map Retrieval: 2008/2009 Field Experiments. In *Proceedings of the IEEE International Geoscience and Remote Sensing Symposium 2009,* Cape Town, South Africa **2009**, *4*, IV-729-IV-732.
19. Monerris, A.; Rodriguez-Alvarez, N.; Vall-llossera, M.; Camps, A.; Piles, M.; Martinez-Fernandez, J.; Sanchez-Martin, N.; Perez-Gutierrez, C.; Baroncini-Turricchia, G.; Acevo, R.; Aguasca, A. The GPS and RAdiometric Joint Observations Experiment at the REMEDHUS Site (Zamora-Salamanca Region, Spain). In *Proceedings of the IEEE International Geoscience and Remote Sensing Symposium 2009,* Cape Town, South Africa **2009**, *3*, III-286-III-289.

20. ECH2O Soil Moisture Sensor. Available: http://www.decagon.com/ag_research/soil/ec5.php.
21. Stevens' Hydra Probe II Soil Moisture Sensor (SDI-12 / RS485). Available at: http://www.stevenswater.com/catalog/products/soil_sensors/datasheet/hydraprobeiidatasheetnewweb.pdf